

1

<sup>2</sup>A SEARCH FOR LONG-LIVED, CHARGED, SUPERSYMMETRIC PARTICLES  
<sup>3</sup>USING IONIZATION WITH THE ATLAS DETECTOR

4

BRADLEY AXEN

5

September 2016 – Version 0.42

6



<sup>8</sup> Bradley Axen: *A Search for Long-Lived, Charged, Supersymmetric Particles using*  
<sup>9</sup> *Ionization with the ATLAS Detector*, Subtitle, © September 2016

10

Usually a quotation.

11

Dedicated to.



<sub>12</sub> ABSTRACT

---

<sub>13</sub> How to write a good abstract:

<sub>14</sub> <https://plg.uwaterloo.ca/~migod/research/beck00PSLA.html>



<sub>15</sub> PUBLICATIONS

---

<sub>16</sub> Some ideas and figures have appeared previously in the following publications:

<sub>17</sub>

<sub>18</sub> Put your publications from the thesis here. The packages `multibib` or `bibtopic`  
<sub>19</sub> etc. can be used to handle multiple different bibliographies in your document.



---

<sup>21</sup> ACKNOWLEDGEMENTS

<sup>22</sup> Put your acknowledgements here.

<sup>23</sup>

<sup>24</sup> And potentially a second round.

<sup>25</sup>



26 CONTENTS

---

27	I	INTRODUCTION	1
28	1	INTRODUCTION	3
29	II	THEORETICAL CONTEXT	5
30	2	STANDARD MODEL	7
31	2.1	Particles . . . . .	7
32	2.2	Interactions . . . . .	8
33	2.3	Limitations . . . . .	8
34	3	SUPERSYMMETRY	9
35	3.1	Motivation . . . . .	9
36	3.2	Structure . . . . .	9
37	3.3	Phenomenology . . . . .	9
38	4	LONG-LIVED PARTICLES	11
39	4.1	Mechanisms . . . . .	11
40	4.1.1	Examples in Supersymmetry . . . . .	11
41	4.2	Phenomenology . . . . .	11
42	4.2.1	Disimilarities to Prompt Decays . . . . .	11
43	4.2.2	Characteristic Signatures . . . . .	11
44	III	EXPERIMENTAL STRUCTURE AND RECONSTRUCTION	13
45	5	THE LARGE HADRON COLLIDER	15
46	5.1	Injection Chain . . . . .	16
47	5.2	Design . . . . .	17
48	5.2.1	Layout . . . . .	17
49	5.2.2	Magnets . . . . .	18
50	5.2.3	RF Cavities . . . . .	19
51	5.2.4	Beam . . . . .	21
52	5.3	Luminosity Parameters . . . . .	21
53	5.4	Delivered Luminosity . . . . .	23
54	6	THE ATLAS DETECTOR	25
55	6.1	Coordinate System . . . . .	27
56	6.2	Magnetic Field . . . . .	28
57	6.3	Inner Detector . . . . .	32
58	6.3.1	Pixel Detector . . . . .	32
59	6.3.2	Semiconductor Tracker . . . . .	32
60	6.3.3	Transition Radiation Tracker . . . . .	32
61	6.4	Calorimetry . . . . .	32
62	6.4.1	Electromagnetic Calorimeters . . . . .	35
63	6.4.2	Hadronic Calorimeters . . . . .	35
64	6.4.3	Forward Calorimeters . . . . .	35
65	6.5	Muon Spectrometer . . . . .	35

66	6.6	Trigger . . . . .	35
67	6.6.1	Trigger Scheme . . . . .	35
68	6.6.2	Missing Transverse Energy Triggers . . . . .	35
69	7	EVENT RECONSTRUCTION . . . . .	39
70	7.1	Tracks and Vertices . . . . .	39
71	7.1.1	Track Reconstruction . . . . .	39
72	7.1.2	Vertex Reconstruction . . . . .	39
73	7.2	Jets . . . . .	39
74	7.2.1	Topological Clustering . . . . .	39
75	7.2.2	Jet Energy Scale . . . . .	39
76	7.2.3	Jet Energy Scale Uncertainties . . . . .	39
77	7.2.4	Jet Energy Resolution . . . . .	39
78	7.3	Electrons . . . . .	39
79	7.3.1	Electron Identification . . . . .	39
80	7.4	Muons . . . . .	39
81	7.4.1	Muon Identification . . . . .	39
82	7.5	Missing Transverse Energy . . . . .	39
83	IV	CALORIMETER RESPONSE . . . . .	41
84	8	RESPONSE MEASUREMENT WITH SINGLE HADRONS . . . . .	43
85	8.1	Dataset and Simulation . . . . .	44
86	8.1.1	Data Samples . . . . .	44
87	8.1.2	Simulated Samples . . . . .	44
88	8.1.3	Event Selection . . . . .	44
89	8.2	Inclusive Hadron Response . . . . .	45
90	8.2.1	E/p Distribution . . . . .	45
91	8.2.2	Zero Fraction . . . . .	46
92	8.2.3	Neutral Background Subtraction . . . . .	47
93	8.2.4	Corrected Response . . . . .	49
94	8.2.5	Additional Studies . . . . .	51
95	8.3	Identified Particle Response . . . . .	54
96	8.3.1	Decay Reconstruction . . . . .	54
97	8.3.2	Identified Response . . . . .	55
98	8.3.3	Additional Species in Simulation . . . . .	57
99	8.4	Summary . . . . .	58
100	9	JET ENERGY RESPONSE AND UNCERTAINTY . . . . .	61
101	9.1	Motivation . . . . .	61
102	9.2	Uncertainty Estimate . . . . .	61
103	9.3	Summary . . . . .	64
104	V	SEARCH FOR LONG-LIVED PARTICLES . . . . .	67
105	10	LONG-LIVED PARTICLES IN ATLAS . . . . .	69
106	10.1	Event Topology . . . . .	69
107	10.1.1	Detector Interactions . . . . .	70
108	10.1.2	Lifetime Dependence . . . . .	71
109	10.2	Simulation . . . . .	74

110	11	EVENT SELECTION	77
111	11.1	Trigger	78
112	11.2	Kinematics and Isolation	79
113	11.3	Particle Species Rejection	83
114	11.4	Ionization	86
115	11.4.1	Mass Estimation	87
116	11.5	Efficiency	88
117	12	BACKGROUND ESTIMATION	91
118	12.1	Background Sources	91
119	12.2	Prediction Method	92
120	12.3	Validation	93
121	12.3.1	Closure in Simulation	93
122	12.3.2	Validation Region in Data	94
123	13	SYSTEMATIC UNCERTAINTIES AND RESULTS	97
124	13.1	Systematic Uncertainties	97
125	13.1.1	Background Estimate	97
126	13.1.2	Signal Yield	98
127	13.2	Final Yields	104
128	13.3	Cross Sectional Limits	105
129	13.4	Mass Limits	107
130	13.5	Context for Long-Lived Searches	109
131	VI	CONCLUSIONS	113
132	14	SUMMARY AND OUTLOOK	115
133	14.1	Summary	115
134	14.2	Outlook	115
135	VII	APPENDIX	117
136	A	INELASTIC CROSS SECTION	119
137	B	EXPANDED R-HADRON YIELDS AND LIMITS	121
138		BIBLIOGRAPHY	127

139 LIST OF FIGURES

---

140	Figure 1	The particle content of the Standard Model ( <a href="#">SM</a> ). . . . .	8
141	Figure 2	The four collision points and corresponding experiments of the Large Hadron Collider ( <a href="#">LHC</a> ). The image includes the location of the nearby city of Geneva as well as the border of France and Switzerland. . . . .	16
142			
143			
144			
145	Figure 3	The cumulative luminosity over time delivered to the A Toroidal LHC ApparatuS ( <a href="#">ATLAS</a> ) experiment from high energy proton-proton collisions since 2011. The energies of the collisions are listed for each of the data-taking periods. . . . .	17
146			
147			
148			
149			
150	Figure 4	The accelerator complex that builds up to the full design energies at the <a href="#">LHC</a> . The protons are passed in order to Linac 2, the <a href="#">PSB</a> , the <a href="#">PS</a> , the <a href="#">SPS</a> and then the <a href="#">LHC</a> . . . . .	18
151			
152			
153			
154	Figure 5	A schematic of the layout of the <a href="#">LHC</a> , not to scale. The arched and straight sections are illustrated at the bottom of the schematic, and all four crossing sites are indicated with their respective experiments. . . . .	19
155			
156			
157			
158	Figure 6	A cross section of the the cryodipole magnets which bend the flight path of protons around the circumference of the <a href="#">LHC</a> . The diagram includes both the superconducting coils which produce the magnetic field and the structural elements which keep the magnets precisely aligned. . . . .	20
159			
160			
161			
162			
163			
164	Figure 7	The arrangement of four radiofrequency ( <a href="#">RF</a> ) cavities within a cryomodule. . . . .	20
165			
166	Figure 8	The cumulative luminosity versus time delivered to ATLAS (green), recorded by ATLAS (yellow), and certified to be good quality data (blue) during stable beams for pp collisions at 13 TeV in 2015. . . . .	23
167			
168			
169			
170	Figure 9	The luminosity-weighted distribution of the mean number of interactions per crossing for the 2015 pp collision data at 13 TeV. . . . .	24
171			
172			
173	Figure 10	A cut-away schematic of the layout of the <a href="#">ATLAS</a> detector. Each of the major subsystems is indicated. . . . .	26
174			
175	Figure 11	A cross-sectional slice of the <a href="#">ATLAS</a> experiment which illustrates how the various <a href="#">SM</a> particles interact with the detector systems. . . . .	26
176			
177			
178	Figure 12	The layout of the four superconducting magnets in the <a href="#">ATLAS</a> detector. . . . .	29
179			
180	Figure 13	. . . . .	30

181	Figure 14	30
182	Figure 15	31
183	Figure 16	31
184	Figure 17	31
185	Figure 18	32
186	Figure 19	32
187	Figure 20	33
188	Figure 21	33
189	Figure 22	34
190	Figure 23	34
191	Figure 24	35
192	Figure 25	36
193	Figure 26	36
194	Figure 27	37
195	Figure 28	
196		An illustration (a) of the $E/p$ variable used throughout this paper. The red energy deposits come from the charged particle targeted for measurement, while the blue energy deposits are from nearby neutral particles and must be subtracted. The same diagram (b) for the neutral-background selection, described in Section 8.2.3.
197		46
198		
199		
200		
201	Figure 29	
202		The $E/p$ distribution and ratio of simulation to data for isolated tracks with (a) $ \eta  < 0.6$ and $1.2 < p/\text{GeV} < 1.8$ and (b) $ \eta  < 0.6$ and $2.2 < p/\text{GeV} < 2.8$ .
203		46
204	Figure 30	
205		The fraction of tracks as a function (a, b) of momentum, (c, d) of interaction lengths with $E \leq 0$ for tracks with positive (on the left) and negative (on the right) charge.
206		48
207		
208	Figure 31	
209		$\langle E/p \rangle_{\text{BG}}$ as a function of the track momentum for tracks with (a) $ \eta  < 0.6$ , (b) $0.6 <  \eta  < 1.1$ , and as a function of the track pseudorapidity for tracks with (c) $1.2 < p/\text{GeV} < 1.8$ , (d) $1.8 < p/\text{GeV} < 2.2$ .
210		49
211		
212	Figure 32	
213		$\langle E/p \rangle_{\text{COR}}$ as a function of track momentum, for tracks with (a) $ \eta  < 0.6$ , (b) $0.6 <  \eta  < 1.1$ , (c) $1.8 <  \eta  < 1.9$ , and (d) $1.9 <  \eta  < 2.3$ .
214		50
215	Figure 33	
216		$\langle E/p \rangle_{\text{COR}}$ calculated using LCW-calibrated topological clusters as a function of track momentum for tracks with (a) zero or more associated topological clusters or (b) one or more associated topological clusters.
217		51
218		
219	Figure 34	
220		Comparison of the $\langle E/p \rangle_{\text{COR}}$ for tracks with (a) less than and (b) greater than 20 hits in the TRT.
221	Figure 35	52
222		Comparison of the $\langle E/p \rangle_{\text{COR}}$ for (a) positive and (b) negative tracks as a function of track momentum for tracks with $ \eta  < 0.6$ .
223		52

224	Figure 36	Comparison of the $E/p$ distributions for (a) positive and (b) negative tracks with $0.8 < p/\text{GeV} < 1.2$ and $ \eta  < 0.6$ , in simulation with the FTFP_BERT and QGSP_BERT physics lists. . . . .	53
225			
226			
227			
228	Figure 37	Comparison of the response of the hadronic calorimeter as a function of track momentum (a) at the EM-scale and (b) after the LCW calibration. . . . .	53
229			
230			
231	Figure 38	Comparison of the response of the EM calorimeter as a function of track momentum (a) at the EM-scale and (b) with the LCW calibration. . . . .	54
232			
233			
234	Figure 39	The reconstructed mass peaks of (a) $K_S^0$ , (b) $\Lambda$ , and (c) $\bar{\Lambda}$ candidates. . . . .	55
235			
236	Figure 40	The $E/p$ distribution for isolated (a) $\pi^+$ , (b) $\pi^-$ , (c) proton, and (d) anti-proton tracks. . . . .	56
237			
238	Figure 41	The fraction of tracks with $E \leq 0$ for identified (a) $\pi^+$ and $\pi^-$ , and (b) proton and anti-proton tracks . . . . .	56
239			
240	Figure 42	The difference in $\langle E/p \rangle$ between (a) $\pi^+$ and $\pi^-$ (b) $p$ and $\pi^+$ , and (c) $\bar{p}$ and $\pi^-$ . . . . .	57
241			
242	Figure 43	$\langle E/p \rangle_{\text{COR}}$ as a function of track momentum for (a) $\pi^+$ tracks and (b) $\pi^-$ tracks. . . . .	58
243			
244	Figure 44	The ratio of the calorimeter response to single particles of various species to the calorimeter response to $\pi^+$ with the physics list FTFP_BERT. . . . .	58
245			
246			
247	Figure 45	The spectra of true particles inside anti- $k_t$ , $R = 0.4$ jets with (a) $90 < p_T/\text{GeV} < 100$ , (b) $400 < p_T/\text{GeV} < 500$ , and (c) $1800 < p_T/\text{GeV} < 2300$ . . . . .	62
248			
249			
250	Figure 46	The jet energy scale ( <b>JES</b> ) uncertainty contributions, as well as the total <b>JES</b> uncertainty, as a function of jet $p_T$ for (a) $ \eta  < 0.6$ and (b) $0.6 <  \eta  < 1.1$ . . . . .	64
251			
252			
253	Figure 47	The <b>JES</b> correlations as a function of jet $p_T$ and $ \eta $ for jets in the central region of the detector. . . . .	65
254			
255	Figure 48	A schematic diagram of an R-Hadron event with a lifetime around 0.01 ns. The diagram includes one charged R-Hadron (solid blue), one neutral R-Hadron (dashed blue), Lightest Supersymmetric Particles ( <b>LSPs</b> ) (dashed green) and charged hadrons (solid orange). The pixel detector, calorimeters, and muon system are illustrated but not to scale. . . . .	71
256			
257			
258			
259			
260			
261			
262	Figure 49	A schematic diagram of an R-Hadron event with a lifetime around 4 ns. The diagram includes one charged R-Hadron (solid blue), one neutral R-Hadron (dashed blue), <b>LSPs</b> (dashed green) and a charged hadron (solid orange). The pixel detector, calorimeters, and muon system are illustrated but not to scale. . . . .	72
263			
264			
265			
266			
267			

268	Figure 50	A schematic diagram of an R-Hadron event with a life-time around 5 ns. The diagram includes one charged R-Hadron (solid blue), one neutral R-Hadron (dashed blue), LSPs (dashed green) and charged hadrons (solid orange). The pixel detector, calorimeters, and muon system are illustrated but not to scale. . . . .	73
274	Figure 51	A schematic diagram of an R-Hadron event with a life-time around 20 ns. The diagram includes one charged R-Hadron (solid blue), one neutral R-Hadron (dashed blue), LSPs (dashed green) and charged hadrons (solid orange). The pixel detector, calorimeters, and muon system are illustrated but not to scale. . . . .	73
280	Figure 52	A schematic diagram of an R-Hadron event with a life-time around 20 ns. The diagram includes one charged R-Hadron (solid blue) and one neutral R-Hadron (dashed blue). The pixel detector, calorimeters, and muon system are illustrated but not to scale. . . . .	74
285	Figure 53	The distribution of (a) $E_T^{\text{miss}}$ and (b) Calorimeter $E_T^{\text{miss}}$ for simulated signal events before the trigger requirement. . . . .	78
288	Figure 54	The distribution of $E_T^{\text{miss}}$ for data and simulated signal events, after the trigger requirement. . . . .	80
290	Figure 55	The trigger efficiency for the HLT_xe70 trigger requirement as a function of (a) $E_T^{\text{miss}}$ and (b) Calorimeter $E_T^{\text{miss}}$ for simulated signal events. . . . .	81
293	Figure 56	The dependence of $dE/dx$ on $N_{\text{split}}$ in data after basic track hit requirements have been applied. . . . .	82
295	Figure 57	The distribution of $dE/dx$ with various selections applied in data and simulated signal events. . . . .	82
297	Figure 58	The distribution of track momentum for data and simulated signal events, after previous selection requirements have been applied. . . . .	83
300	Figure 59	The distribution of $M_T$ for data and simulated signal events, after previous selection requirements have been applied. . . . .	84
303	Figure 60	The distribution of summed tracked momentum within a cone of $\Delta R < 0.25$ around the candidate track for data and simulated signal events, after previous selection requirements have been applied. . . . .	85
307	Figure 61	The normalized, two-dimensional distribution of $E/p$ and $f_{\text{EM}}$ for simulated (a) $Z \rightarrow ee$ , (b) $Z \rightarrow \tau\tau$ , (c) 1200 GeV Stable R-Hadron events, and (d) 1200 GeV, 10 ns R-Hadron events. . . . .	86

311	Figure 62	Two-dimensional distribution of $dE/dx$ versus charge signed momentum ( $qp$ ) for minimum-bias tracks. The fitted distributions of the most probable values for pions, kaons and protons are superimposed. . . . .	87
312			
313			
314			
315	Figure 63	The distribution of mass estimated using $dE/dx$ for simulated stable R-Hadrons with masses between 1000 and 1600 GeV. . . . .	88
316			
317			
318	Figure 64	The acceptance $\times$ efficiency as a function of R-Hadron (a) mass and (b) lifetime. (a) shows all of the combinations of mass and lifetime considered in this search, and (b) highlights the lifetime dependence for 1000 GeV and 1600 GeV R-Hadrons. . . . .	90
319			
320			
321			
322			
323	Figure 65	The distribution of (a) $dE/dx$ and (b) momentum for tracks in data and simulated signal after requiring the event level selection and the track selection on $p_T$ , hits, and $N_{\text{split}}$ . Each sub-figure shows the normalized distributions for tracks classified as hadrons, electrons, and muons in data and R-Hadrons in the simulated signal. . . . .	92
324			
325			
326			
327			
328			
329			
330	Figure 66	The distribution of $M_{dE/dx}$ (a) before and (b) after the ionization requirement for tracks in simulated W boson decays and for the randomly generated background estimate. . . . .	94
331			
332			
333			
334	Figure 67	The distribution of $M_{dE/dx}$ (a) before and (b) after the ionization requirement for tracks in the validation region and for the randomly generated background estimate. . . . .	95
335			
336			
337			
338	Figure 68	The trigger efficiency for the HLT_xe70 trigger requirement as a function of Calorimeter $E_T^{\text{miss}}$ for simulated data events with a W boson selection. Simulated signal events and simulated W boson events are also included. . . . .	100
339			
340			
341			
342			
343	Figure 69	The efficiency of the muon veto for R-hadrons of two different masses, as a function of $\frac{1}{\beta}$ for simulated R-Hadron tracks. . . . .	102
344			
345			
346	Figure 70	The average reconstructed MDT $\beta$ distribution for $Z \rightarrow \mu\mu$ events in which one of the muons is reconstructed as a slow muon, for both data and simulation. A gaussian fit is superimposed. . . . .	103
347			
348			
349			
350	Figure 71	The observed mass distribution of events in data and the generated background distribution in (a) the stable and (b) the metastable signal region. A few example simulated signal distributions are superimposed. . . . .	104
351			
352			
353			

354	Figure 72	The observed and expected cross section limits as a function of mass for the stable simulated signal. The predicted cross section values for the corresponding signals are included. . . . .	107
355			
356			
357			
358	Figure 73	The observed and expected cross section limits as a function of mass for each generated lifetime. The predicted cross section values for the corresponding signals are included. . . . .	108
359			
360			
361			
362	Figure 74	The excluded range of masses as a function of gluino lifetime. The expected lower limit (LL), with its experimental $\pm 1\sigma$ band, is given with respect to the nominal theoretical cross-section. The observed 95% LL obtained at $\sqrt{s} = 8$ TeV [61] is also shown for comparison. . . . .	110
363			
364			
365			
366			
367	Figure 75	The constraints on the gluino mass as a function of lifetime for a split-supersymmetry model with the gluino R-Hadrons decaying into a gluon or light quarks and a neutralino with mass of 100 GeV. The solid lines indicate the observed limits, while the dashed lines indicate the expected limits. The area below the curves is excluded. The dots represent results for which the particle is assumed to be prompt or stable. . . . .	111
368			
369			
370			
371			
372			
373			
374			

375 LIST OF TABLES

---

376	Table 1	The design parameters of the LHC beam that determines the energy of collisions and the luminosity, for both the injection of protons and at the nominal circulation. . . . .	22
377			
378			
379			
380	Table 2	The performance goals for each of the subsystems of the ATLAS detector. The $ \eta $ coverage specifies the range where the subsystem needs to be able to provide measurements with the specified resolution. The resolutions include a $p_T$ or E dependence that is added in quadrature with a $p_T/E$ independent piece. . . . .	27
381			
382			
383			
384			
385			
386	Table 3	The dominant sources of corrections and systematic uncertainties in the JES estimation technique, including typical values for the correcting shift ( $\Delta$ ) and the associated uncertainty ( $\sigma$ ). . . . .	63
387			
388			
389			
390	Table 4	The expected number of events at each level of the selection for metastable 1600 GeV, 10 ns R-Hadrons, along with the number of events observed in data, for $3.2 \text{ fb}^{-1}$ . The simulated yields are shown with statistical uncertainties only. The total efficiency $\times$ acceptance is also shown for the signal. . . . .	89
391			
392			
393			
394			
395			
396	Table 5	A summary of the sources of systematic uncertainty for the data-driven background in the signal region. If the uncertainty depends on the mass, the maximum values are reported. . . . .	97
397			
398			
399			
400	Table 6	A summary of the sources of systematic uncertainty for the simulated signal yield. The uncertainty depends on the mass and lifetime, and the maximum negative and positive values are reported in the table. . . . .	99
401			
402			
403			
404	Table 7	Example of the contributing systematic variations to the total systematic for the $E_T^{\text{miss}}$ Scale, as measured in a 1200 GeV, Stable R-Hadron signal sample. . . . .	101
405			
406			
407	Table 8	The estimated number of background events and the number of observed events in data for the specified selection regions prior to the requirement on mass. The background estimates show statistical and systematic uncertainties. . . . .	104
408			
409			
410			
411			
412	Table 9	The left and right extremum of the mass window for each generated mass point with a 10 ns lifetime. . . . .	105
413			
414	Table 10	The left and right extremum of the mass window used for each generated stable mass point. . . . .	105
415			

416	Table 11	The expected number of signal events, the expected number of background events, and the observed number of events in data with their respective statistical errors within the respective mass window for each generated stable mass point . . . . .	106
417			
418			
419			
420			
421	Table 12	The expected number of signal events, the expected number of background events, and the observed number of events in data with their respective statistical errors within the respective mass window for each generated mass point with a lifetime of 10 ns. . . . .	106
422			
423			
424			
425			
426	Table 13	The observed and expected 95% CL lower limit on mass for gluino R-Hadrons for each considered lifetime. . . . .	109
427			
428	Table 14	The left and right extremum of the mass window for each generated mass point with a 50 ns lifetime. . . . .	121
429			
430	Table 15	The left and right extremum of the mass window for each generated mass point with a 30 ns lifetime. . . . .	121
431			
432	Table 16	The left and right extremum of the mass window for each generated mass point with a 10 ns lifetime. . . . .	122
433			
434	Table 17	The left and right extremum of the mass window used for each generated mass point with a lifetime of 3 ns. . . . .	122
435			
436	Table 18	The left and right extremum of the mass window used for each mass point with a lifetime of 1 ns. . . . .	122
437			
438	Table 19	The left and right extremum of the mass window for each generated mass point with a lifetime of 0.4 ns. . . . .	123
439			
440	Table 20	The left and right extremum of the mass window used for each generated stable mass point. . . . .	123
441			
442	Table 21	The expected number of signal events, the expected number of background events, and the observed number of events in data with their respective statistical errors within the respective mass window for each generated mass point with a lifetime of 50 ns. . . . .	123
443			
444			
445			
446			
447	Table 22	The expected number of signal events, the expected number of background events, and the observed number of events in data with their respective statistical errors within the respective mass window for each generated mass point with a lifetime of 30 ns. . . . .	124
448			
449			
450			
451			
452	Table 23	The expected number of signal events, the expected number of background events, and the observed number of events in data with their respective statistical errors within the respective mass window for each generated mass point with a lifetime of 10 ns. . . . .	124
453			
454			
455			
456			
457	Table 24	The expected number of signal events, the expected number of background events, and the observed number of events in data with their respective statistical errors within the respective mass window for each generated mass point with a lifetime of 3 ns. . . . .	125
458			
459			
460			
461			

462	Table 25	The expected number of signal events, the expected number of background events, and the observed number of events in data with their respective statistical errors within the respective mass window for each generated mass point with a lifetime of 1 ns. . . . .	125
463			
464			
465			
466			
467	Table 26	The expected number of signal events, the expected number of background events, and the observed number of events in data with their respective statistical errors within the respective mass window for each generated mass point with a lifetime of p4 ns. . . . .	126
468			
469			
470			
471			
472	Table 27	The expected number of signal events, the expected number of background events, and the observed number of events in data with their respective statistical errors within the respective mass window for each generated stable mass point . . . . .	126
473			
474			
475			
476			



478 ACRONYMS

---

- 479 SM Standard Model  
480 CERN European Organization for Nuclear Research  
481 SUSY Supersymmetry  
482 LSP Lightest Supersymmetric Particle  
483 LHC Large Hadron Collider  
484 ATLAS A Toroidal LHC ApparatuS  
485 CMS Compact Muon Solenoid  
486 ALICE A Large Ion Collider Experiment  
487 LHCb Large Hadron Collider beauty experiment  
488 LEP the Large Electron Positron collider  
489 PS Proton Synchrotron  
490 PSB Proton Synchrotron Booster  
491 SPS Super Proton Synchrotron  
492 ToT time over threshold  
493 LCW local cluster weighted  
494 MIP minimally ionizing particle  
495 EPJC European Physical Journal C  
496 JES jet energy scale  
497 LLP Long-Lived Particle  
498 CR Control Region  
499 NLO next-to-leading order  
500 NLL next-to-leading logarithmic  
501 PDF parton distribution function  
502 ISR initial state radiation  
503 RMS root mean square  
504 IBL Insertible B-Layer

<sup>505</sup> CP Combined Performance

<sup>506</sup> MDT Monitored Drift Tube

<sup>507</sup> RF radiofrequency



508

## PART I

509

### INTRODUCTION

510

You can put some informational part preamble text here.



# 1

s11

## s12 INTRODUCTION

---



S13

## PART II

S14

### THEORETICAL CONTEXT

S15

You can put some informational part preamble text here.



# 2

516

## 517 STANDARD MODEL

---

518 The SM of particle physics seeks to explain the symmetries and interactions of  
519 all currently discovered fundamental particles. It has been tested by several genera-  
520 tions of experiments and has been remarkably successful, no significant de-  
521 viations have been found. The SM provides predictions in particle physics for  
522 interactions up to the Planck scale ( $10^{15}$ - $10^{19}$  GeV).

523 The theory itself is a quantum field theory grown from an underlying  $SU(3) \times$   
524  $SU(2) \times U(1)$  that requires the particle content and quantum numbers consist-  
525 ent with experimental observations (see Section 2.1). Each postulated symme-  
526 try is accompanied by an interaction between particles through gauge invari-  
527 ance. These interactions are referred to as the Strong, Weak, and Electromag-  
528 netic forces, which are discussed in Section 2.2.

529 Although this model has been very predictive, the theory is incomplete; for  
530 example, it is not able to describe gravity or astronomically observed dark matter.  
531 These limitations are discussed in more detail in Section 2.3.

## 532 21 PARTICLES

533 The most familiar matter in the universe is made up of protons, neutrons, and  
534 electrons. Protons and neutrons are composite particles, however, and are made  
535 up in turn by particles called quarks. Quarks carry both electric charge and color  
536 charge, and are bound in color-neutral combinations called baryons. The elec-  
537 tron is an example of a lepton, and carries only electric charge. Another type  
538 of particle, the neutrino, does not form atomic structures in the same way that  
539 quarks and leptons do because it carries no color or electric charge. Collectively,  
540 these types of particles are known as fermions, the group of particles with half-  
541 integer spin.

542 There are three generations of fermions, although familiar matter is formed  
543 predominantly by the first generation. The generations are identical except for  
544 their masses, which increase in each generation by convention. In addition, each  
545 of these particles is accompanied by an antiparticle, with opposite-sign quantum  
546 numbers but the same mass.

547 The fermions comprise what is typically considered matter, but there are  
548 additional particles that are mediators of interactions between those fermions.  
549 These mediators are known as the gauge bosons, gauge in that their existence  
550 is required by gauge invariance (discussed further in Section 2.2) and bosons in  
551 that they have integer spin. The boson which mediates the electromagnetic force  
552 is the photon, the first boson to be discovered; it has no electric charge, no mass,  
553 and a spin of 1. There are three spin-1 mediators of the weak force, the two  
554 W bosons and the Z boson. The W bosons have electric charge of  $\pm 1$  and a  
555 mass of  $80.385 \pm 0.015$  GeV, while the Z boson is neutral and has a mass of

556 91.1876  $\pm$  0.0021 GeV. The strong force is mediated by eight particles called  
 557 gluons, which are massless and electrically neutral but do carry color charge.

558 The final particle present in the SM is the Higgs boson, which was recently  
 559 observed for the first time by experiments at CERN in 2012. It is electrically  
 560 neutral, has a mass of 125.7  $\pm$  0.4 GeV, and is the only spin-0 particle yet to be  
 561 observed. The Higgs boson is the gauge boson associated with the mechanism  
 562 that gives a mass to the W and Z bosons.

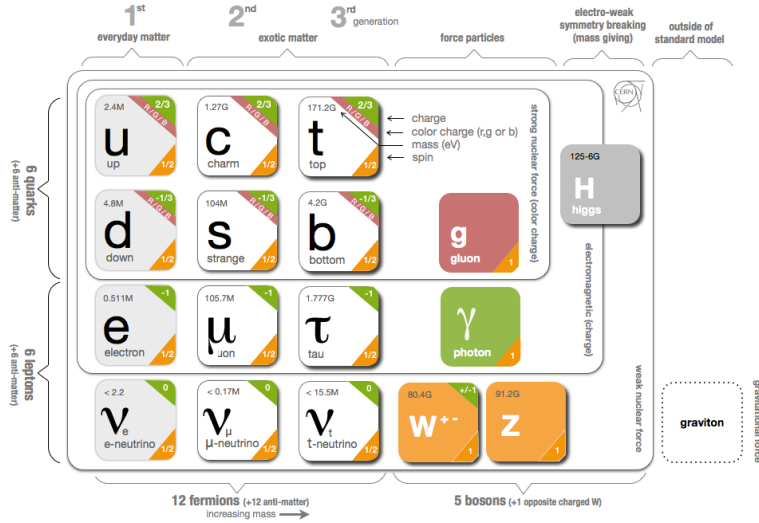


Figure 1: The particle content of the SM.

563 Together these particles form the entire content of the SM, and are summa-  
 564 rized in Figure 1. These are the particles that constitute the observable universe  
 565 and all the so-far-observed interactions within it.

## 566 2.2 INTERACTIONS

567 The interactions predicted and described by the SM are fundamentally tied to the  
 568 particles within it, both in that they describe the way those particles can influence  
 569 each other and also in that the existence of the interactions requires the existence  
 570 of some particles (the gauge bosons).

## 571 2.3 LIMITATIONS

# 3

572

573 SUPERSYMMETRY

---

574 3.1 MOTIVATION

575 3.2 STRUCTURE

576 3.3 PHENOMENOLOGY



# 4

577

## 578 LONG-LIVED PARTICLES

---

### 579 4.1 MECHANISMS

#### 580 4.1.1 EXAMPLES IN SUPERSYMMETRY

### 581 4.2 PHENOMENOLOGY

#### 582 4.2.1 DISIMILARITIES TO PROMPT DECAYS

#### 583 4.2.2 CHARACTERISTIC SIGNATURES



584

### PART III

585

## EXPERIMENTAL STRUCTURE AND RECONSTRUCTION

586

You can put some informational part preamble text here.



587

588 THE LARGE HADRON COLLIDER

---

589 The LHC, a two-ring superconducting hadron accelerator, provides high energy  
590 proton-proton collisions for several large experiments at European Organization  
591 for Nuclear Research (CERN) in Geneva, Switzerland [1, 2]. It is the largest,  
592 highest-luminosity, and highest-energy proton collider ever built, and was con-  
593 structed by a collaboration of more than 10,000 scientists from the more than  
594 100 countries that contribute to CERN. The original design of the LHC focused on  
595 providing collision energies of up to 14 TeV and generating enough collisions to  
596 reveal physics beyond the SM which is predicted to exist at higher energy scales.

597 The LHC was installed in an existing 27 km tunnel at CERN which was origi-  
598 nally designed to house the Large Electron Positron collider (LEP). This allows  
599 the collider to use existing accelerators at the same complex to provide the initial  
600 acceleration of protons up to 450 GeV before injecting into LHC. The injected  
601 hadrons are accelerated up to as much as 14 TeV while being focused into two  
602 beams traveling in opposite directions. During this process the protons circulate  
603 around the tunnel millions of times, while the beams are intermittently crossed  
604 at the four locations of the experiments to provide collisions. These collision  
605 points correspond to the four major LHC experiments: ATLAS, Compact Muon  
606 Solenoid (CMS), Large Hadron Collider beauty experiment (LHCb), and A Large  
607 Ion Collider Experiment (ALICE), and Figure 2 shows the layout of the exper-  
608 iments both on the surface and below. ATLAS and CMS are both general pur-  
609 pose, high-luminosity detectors which search for a wide range of new types of  
610 physics [3, 4]. LHCb studies the interactions of b-hadrons to explore the asymme-  
611 try between matter and antimatter [5]. ALICE focuses on the collisions of lead  
612 ions, which the LHC also provides, in order to study the properties of quark-  
613 gluon plasma [6].

614 During the first five years of operation, after the LHC turned on in 2010, the  
615 LHC has provided four major data collecting periods. In 2010 the LHC generated  
616 collisions at several energies, starting at 900 GeV. It increased the energy from  
617 900 GeV to 2.76 TeV and then subsequently to 7 TeV, with a peak luminos-  
618 ity of  $2 \times 10^{32} \text{ cm}^{-2}\text{s}^{-1}$ , and a total delivered luminosity of  $50 \text{ pb}^{-1}$ . The next  
619 run, during 2011, continued the operation at 7 TeV and provided an additional  $5$   
620  $\text{fb}^{-1}$  with a peak luminosity of  $4 \times 10^{33} \text{ cm}^{-2}\text{s}^{-1}$ . The energy was then increased  
621 to 8 TeV for the data collection during 2012, which provided  $23 \text{ fb}^{-1}$  with a peak  
622 luminosity of  $7.7 \times 10^{33} \text{ cm}^{-2}\text{s}^{-1}$ . After the first long shutdown for 2013 and  
623 2014, the LHC resumed operation and increased the energy to 13 TeV in 2015,  
624 where it delivered  $4.2 \text{ fb}^{-1}$  with a peak luminosity of  $5.5 \times 10^{33} \text{ cm}^{-2}\text{s}^{-1}$ . The  
625 LHC is currently providing additional 13 TeV collisions in 2016 with higher lu-  
626 minosities than during any previous data collection periods. These running peri-  
627 ods are summarized in Figure 3, which shows the total delivered luminosity over

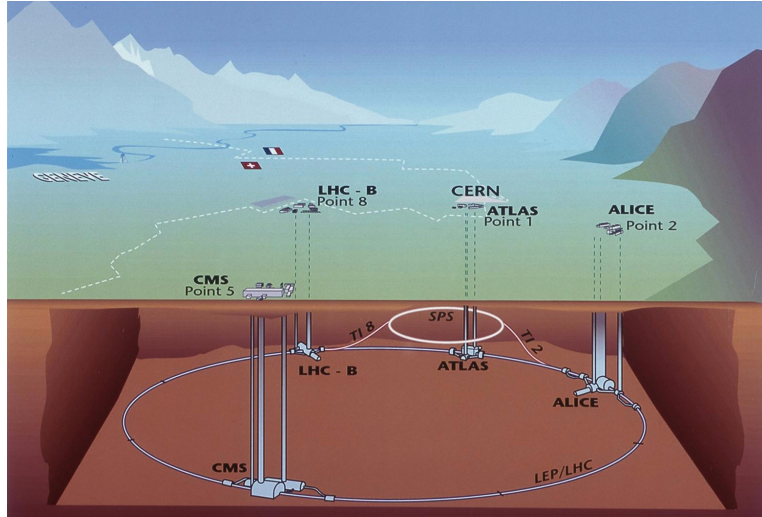


Figure 2: The four collision points and corresponding experiments of the [LHC](#). The image includes the location of the nearby city of Geneva as well as the border of France and Switzerland.

628 time for the [ATLAS](#) experiment during each of the four years of data collection  
629 since 2011.

### 630 5.1 INJECTION CHAIN

631 The [LHC](#) takes advantage of the presence of previously built accelerators at [CERN](#)  
632 to work up to the target energy in consecutive stages. The series of accelerators  
633 that feed into the [LHC](#) are known collectively as the injection chain, and together  
634 with the [LHC](#) form the accelerator complex. The full complex is illustrated in  
635 Figure 4, which details the complex series required to reach collisions of 13 or  
636 14 TeV.

637 Protons at the [LHC](#) begin as hydrogen atoms in the Linac 2, a linear accelerator  
638 which replaced Linac 1 as the primary proton accelerator at CERN in 1978. In  
639 Linac 2, the hydrogen atoms are stripped of their electrons by a strong magnetic  
640 field, and the resulting protons are accelerated up to 50 MeV by cylindrical con-  
641 ductors charged by radio frequency cavities. The protons are then transferred  
642 to the Proton Synchrotron Booster ([PSB](#)), which uses a stack of four synchrotron  
643 rings to accelerate the protons up to 1.4 GeV. Then the protons are injected  
644 into the Proton Synchrotron ([PS](#)) which again uses synchrotron rings to bring  
645 the energy up to 25 GeV. The intermediate step between Linac 2 and the [PS](#) is  
646 not directly necessary, as the [PS](#) can accelerate protons starting from as low as  
647 50 MeV. The inclusion of the [PSB](#) allows the [PS](#) to accept a higher intensity of  
648 injection and so increases the deliverable luminosity in the [LHC](#). The penulti-  
649 mate stage of acceleration is provided by the Super Proton Synchrotron ([SPS](#)), a  
650 large synchrotron with a 7 km circumference that was commissioned at CERN  
651 in 1976. During this step the protons increase in energy to 450 GeV, after which  
652 they can be directly injected into the [LHC](#).

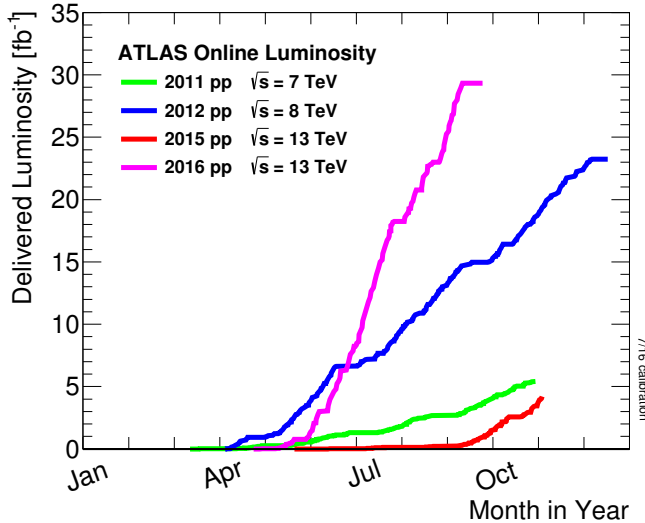


Figure 3: The cumulative luminosity over time delivered to the [ATLAS](#) experiment from high energy proton-proton collisions since 2011. The energies of the collisions are listed for each of the data-taking periods.

653        The final step is the [LHC](#) itself, which receives protons from the [SPS](#) into two  
 654        separate beam pipes which circulate in opposite directions. The filling process  
 655        at this steps takes approximately 4 minutes, and the subsequent acceleration to  
 656        the final energy (6.5 TeV during 2015 and up to 7 TeV by design) takes approxi-  
 657        mately half an hour. At this point the protons circulate around the circumference  
 658        tens of thousands of times a second and continue for up to two hours.

## 659        5.2 DESIGN

### 660        5.2.1 LAYOUT

661        Many of the aspects of the [LHC](#) design are driven by the use of the existing [LEP](#)  
 662        tunnel. This tunnel slopes gradually, with a 1.4% decline, with 90% of its length  
 663        built into molasse rock which is particularly well suited to the application. The  
 664        circumference is composed of eight 2987 meter arcs and eight 528 meter straight  
 665        sections which connect them; this configuration is illustrated in Figure 5. The  
 666        tunnel diameter is 3.7 m throughout its length.

667        The design energy is directly limited by the size of this tunnel, with its radius  
 668        of curvature of 2804 m. A significant magnetic field is required to curve the  
 669        protons around that radius of curvature; the relationship is given by

$$p \simeq 0.3BR \quad (1)$$

670        where  $p$  is the momentum of the particle in GeV,  $B$  is the magnetic field in Tesla,  
 671        and  $R$  is the radius of curvature in meters. From the target design energy of  
 672        14 TeV, or 7 TeV of momentum for protons in each beam, the required mag-  
 673        netic field is 8.33 Tesla. This is too large a field strength to be practical with

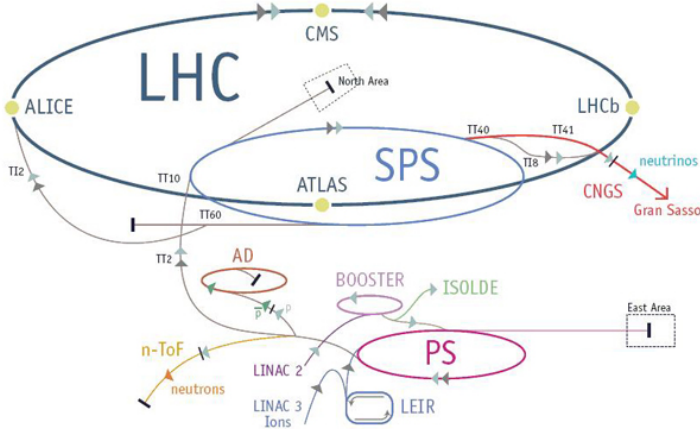


Figure 4: The accelerator complex that builds up to the full design energies at the [LHC](#). The protons are passed in order to Linac 2, the [PSB](#), the [PS](#), the [SPS](#) and then the [LHC](#).

674 iron electromagnets, because of the enormous power required and the resulting  
 675 requirements for cooling. Because of these constraints, the [LHC](#) uses supercon-  
 676 ducting magnets which can maintain that field strength with significantly less  
 677 power consumption.

#### 678 5.2.2 MAGNETS

679 Specifically the magnets chosen were Niobium and Titanium (NbTi) which al-  
 680 low for field strengths as high as 10 Tesla when cooled down to 1.9 K. Reaching  
 681 the target temperature of 1.9 K for all of the magnets requires superfluid helium  
 682 and a large cryogenic system along the entire length of the tunnel. During nor-  
 683 mal operation, the [LHC](#) uses 120 tonnes of helium within the magnets, and the  
 684 entire system is cooled by eight cryogenic helium refrigerators. The tempera-  
 685 ture increase that occurs during transit from the refrigerator along the beam  
 686 necessitates that the refrigerators cool the helium down to 1.8 K. Any significant  
 687 increase above this temperature range can remove the superconductive proper-  
 688 ties of the magnets, which in turn generates drastically larger heat losses from  
 689 the current within the magnets and causes a rapid rise in temperature called a  
 690 quench.

691 In all there are approximately 8000 superconducting magnets distributed around  
 692 the [LHC](#). The 1232 bending magnets, which keep the protons curving along the  
 693 length of the beam, are twin bore cryodipoles, which allow both proton beams  
 694 to be accommodated by one magnet and all of the associated cooling structure.  
 695 Figure 6 shows the cross section of the design for these dipoles. The magnets are  
 696 very large, 16.5 m long with a diameter of 0.57 meters and a total weight of 28  
 697 tonnes. They are slightly curved, with an angle of 5.1 mrad, in order to carefully  
 698 match the beam path. The twin bore accommodates both magnets inside the  
 699 two 5 cm diameter holes which are surrounded by the superconducting coils.  
 700 The coils require 12 kA of current in order to produce the required magnetic

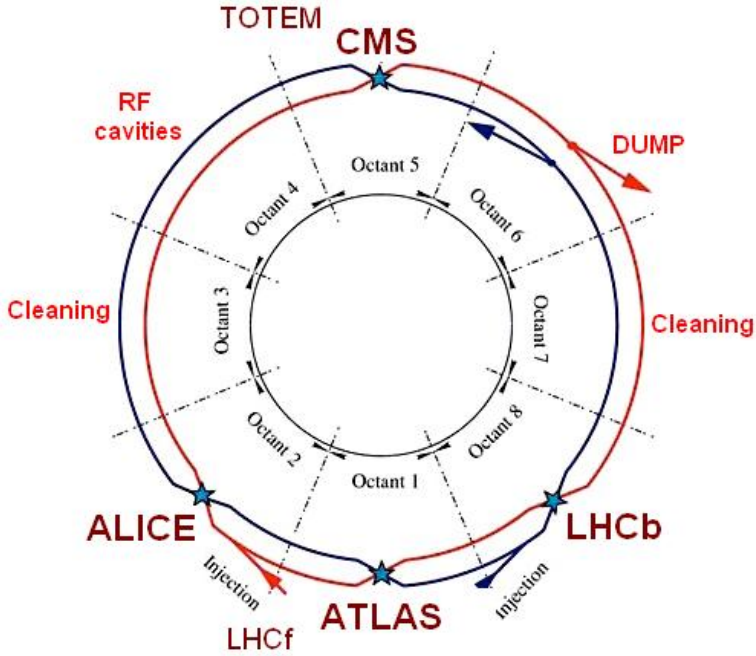


Figure 5: A schematic of the layout of the LHC, not to scale. The arched and straight sections are illustrated at the bottom of the schematic, and all four crossing sites are indicated with their respective experiments.

701 field. These coils are comprised of NbTi cable wound in two layers; the wire in  
 702 the inner layer has a diameter of 1.065 mm while the wire in the outer layer has  
 703 a diameter of 0.825 mm.

704 The large currents in the wires, along with the magnetic field produced, result  
 705 in forces on the magnets which would tend to push them apart with over 10,000  
 706 Newtons per meter. Constraining the magnets requires a significant amount of  
 707 structure including non-magnetic stainless steel collars. Both the presence of  
 708 these electromagnetic forces and the varying thermal contraction coefficient of  
 709 the pieces of the magnet produce significant forces on the cold mass structure.  
 710 The cold mass is carefully engineered to so that these stresses do not significantly  
 711 alter the magnetic field shape, which must be maintained between magnets to a  
 712 precision of approximately  $10^{-4}$  for successful operation.

713 The remaining 6800 magnets are a variety of quadrupole, sextapole, octopole,  
 714 and single bore dipole magnets. These are used to damp oscillations, correct  
 715 beam trajectories, focus the beams during circulation, and to squeeze the beams  
 716 before collisions.

### 717 5.2.3 RF CAVITIES

718 Sixteen RF cavities produce the actual acceleration of the proton beam up to the  
 719 design energy. These RF cavities are tuned to operate at 400 MHz, and are pow-  
 720 ered by high-powered electron beams modulated at the same frequency, called  
 721 klystrons. The resonance within the cavity with the oscillating electric field  
 722 establishes a voltage differential of 2 MV per cavity. The sixteen cavities are

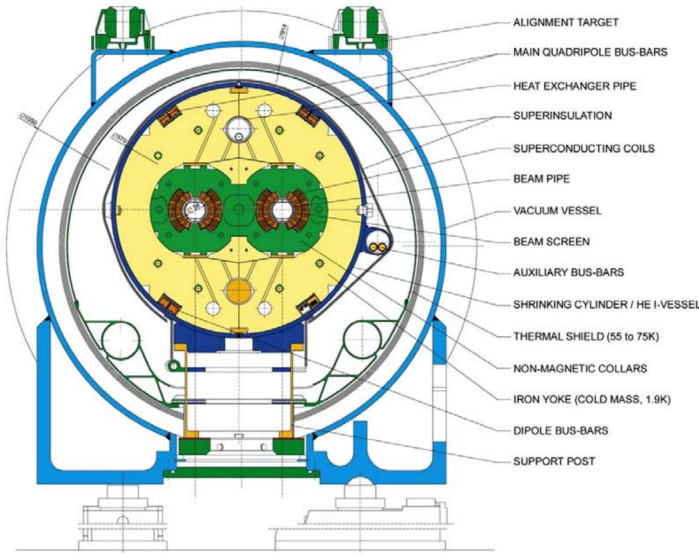


Figure 6: A cross section of the cryodipole magnets which bend the flight path of protons around the circumference of the LHC. The diagram includes both the superconducting coils which produce the magnetic field and the structural elements which keep the magnets precisely aligned.

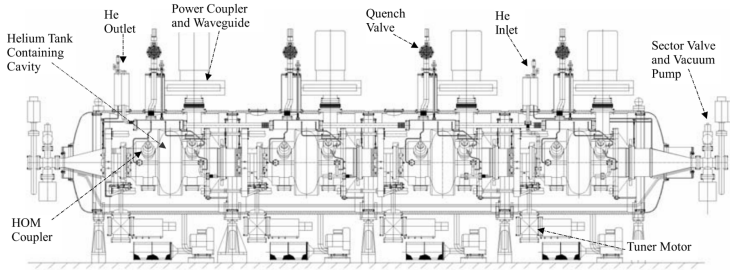


Figure 7: The arrangement of four RF cavities within a cryomodule.

723 split between the two beams, so combined the cavities provide 16 MV per beam,  
 724 which accelerate the protons on each consecutive pass through the cavity. This  
 725 acceleration is also necessary during circulation even after the target energy has  
 726 been reached in order to compensate for losses from synchrotron radiation.

727 The cavities are arranged in cryomodules which contain four cavities, with  
 728 two cryomodules per beam; this arrangement is illustrated in Figure 7. These  
 729 cryomodules are necessary to maintain the superconducting state of the cavities,  
 730 which are also constructed from niobium. The RF cavities use niobium along  
 731 with copper to allow for low power losses in the superconductors. The copper  
 732 provides a reduced susceptibility to quenching, as it rapidly conducts away heat  
 733 generated by imperfections in the niobium, as well as natural shielding from the  
 734 earth's magnetic field which can interfere with the RF system.

735 The nature of the radio frequency oscillations tends to group protons together  
 736 into buckets. A proton traveling exactly in phase with the RF oscillations will not  
 737 be displaced at all during a single circulation, and those slightly ahead or behind

738 of that phase will slightly decelerate or accelerate, respectively. This produces  
 739 separate clusters of protons which arrive in phase to the cavities every 2.5 ns,  
 740 corresponding to the 400 MHz frequency.

741 5.2.4 BEAM

742 The beams of protons circulate within 54 km of 5 cm diameter beam pipe. This  
 743 entire structure is kept under vacuum at 1.9 K to prevent interactions between  
 744 the beam pipe and the magnets as well as to prevent any interactions between the  
 745 circulating protons and gas in the pipe. The vacuum within the pipe establishes  
 746 a pressure as low as  $10^{-9}$  mbar before the protons are introduced.

747 Because of the very high energies of the circulating protons, synchrotron ra-  
 748 diation is not negligible in the bending regions. The protons are expected to  
 749 radiate 3.9 kW per beam at 14 TeV, with 0.22 W/m, which is enough power to  
 750 heat the liquid helium and cause a quench were it absorbed by the magnets. To  
 751 prevent this, a copper screen is placed within the vacuum tube that absorb the  
 752 emitted photons. This screen is kept between 5 and 20 K by the liquid helium  
 753 cooling system.

754 5.3 LUMINOSITY PARAMETERS

755 In addition to the high energy of the collisions, the rate of collisions is extremely  
 756 important to enabling the discovery of new physics. Many measurements and  
 757 searches require a large number of events in order to be able to make statistically  
 758 significant conclusions. The rate of collisions is measured using luminosity, the  
 759 number of collisions per unit time and unit cross section for the proton-proton  
 760 collisions. From the beam parameters, luminosity is given by

$$\mathcal{L} = \frac{N_b^2 n_b f_{rev} \gamma}{4\pi \epsilon_n \beta^*} F \quad (2)$$

761 where  $N_b$  is the number of protons per bunch,  $n_b$  is the number of bunches per  
 762 beam,  $f_{rev}$  is the frequency of revolution,  $\gamma$  is the Lorentz factor for the protons  
 763 at the circulating energy,  $\epsilon_n$  is the emittance,  $\beta^*$  is the amplitude function at the  
 764 collision point, and  $F$  is a geometric factor that accounts for the crossing angle of  
 765 the beams at the collision point. The emittance measures the average spread of  
 766 particles in both position and momentum space, while the amplitude function  
 767 is a beam parameter which measures how much the beam has been squeezed.  
 768 Together  $\epsilon_n$  and  $\beta^*$  give the size of the beam in the transverse direction,  $\sigma = \sqrt{\epsilon \beta^*}$ .  $\beta$   
 769 changes over the length of the beam as the accessory magnets shape the  
 770 distribution of protons, but only the value at the point of collisions,  $\beta^*$ , affects  
 771 the luminosity.

772 The luminosity is maximized to the extent possible by tuning the parameters  
 773 in Equation 2. A number of these are constrained by the design decisions. The  
 774 revolution frequency is determined entirely by the length of the tunnel, as the

Parameter	Unit	Injection	Nominal
Beam Energy	TeV	0.450	7
Peak Instantaneous Luminosity	$\text{cm}^{-2}\text{s}^{-1}$	-	$10^{34}$
Bunch Spacing	ns	25	25
Number of Filled Bunches	-	2808	2808
Normalized Transverse Emittance	$\mu\text{m}$	3.75	3.75
Frequency	MHz	400.789	400.790
RF Voltage/Beam	MV	8	16
Stored Energy	MJ	-	362
Magnetic Field	T	0.54	8.33
Operating Temperature	K	1.9	1.9

Table 1: The design parameters of the [LHC](#) beam that determines the energy of collisions and the luminosity, for both the injection of protons and at the nominal circulation.

775 protons travel at very close to the speed of light. The geometric factor  $F$  is de-  
 776 termined by the crossing angle of the beams at the collision points, again a com-  
 777 ponent of the tunnel design; this angle is already very small at  $285 \mu\text{rad}$ , which  
 778 helps to maximize the geometric factor.

779 The major pieces that can be adjusted are the number of protons per bunch,  
 780  $N_b$ , the number of bunches in the beam,  $n_b$ , and the amplitude function  $\beta$ . In-  
 781 creasing either  $N_b$  or  $n_b$  increases the amount of energy stored in the beam,  
 782 which presents a danger if control of the beam is lost. At design specifications,  
 783 the beam stores 362 MJ, which is enough energy to damage the detectors or ac-  
 784 celerator if the beam were to wander out of the beam pipe. So, the luminosity  
 785 is primarily controlled at the [LHC](#) by adjusting  $\beta^*$ , where lowering  $\beta^*$  increases  
 786 the luminosity.  $\beta^*$  is tuned to provide the various values of luminosity used at  
 787 the [LHC](#) which can be raised to as much as  $10^{34}$ .

788 The nominal bunch structure consists of 3654 bunches, each holding  $10^{11}$  pro-  
 789 tons, which cross a collision point in 25 ns. These are further subdivided into the  
 790 buckets mentioned in Section 5.2.3 by the clustering properties of the RF cavities.  
 791 The bunches are further grouped into trains of 72 bunches which are separated  
 792 by a gap which would otherwise hold 12 bunches. At nominal operation 2808  
 793 of the bunches will actually be filled with protons, while the remainder are left  
 794 empty to form an abort gap that can be used in case the beam needs to be dumped.

795 The various beam parameters are summarized in Table 1 for the designed op-  
 796 eration. In practice the beam has operated at lower energies and lower luminosi-  
 797 ties than the design values, but the [LHC](#) is expected to operate at the full design  
 798 values during Run 2.

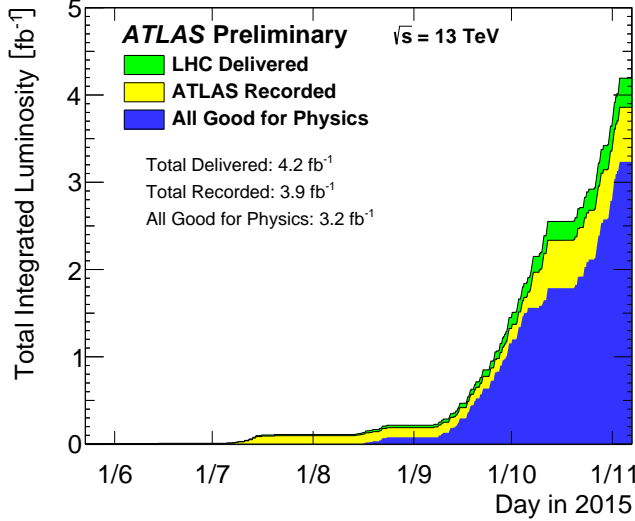


Figure 8: The cumulative luminosity versus time delivered to ATLAS (green), recorded by ATLAS (yellow), and certified to be good quality data (blue) during stable beams for pp collisions at 13 TeV in 2015.

## 5.4 DELIVERED LUMINOSITY

During the data collection of 2015, the [LHC](#) operated at luminosities as large as  $5 \times 10^{33}$ . It is convenient to refer to the integrated luminosity, the integral of the instantaneous luminosity, which corresponds directly to the number of delivered events for a given process.

$$N = \sigma \times \int \mathcal{L}(t) dt$$

where  $\sigma$  is the cross section for the process of interest. The integrated luminosity over time is shown in Figure 8. This includes the luminosity delivered by the [LHC](#) as well as the luminosity that was recorded by [ATLAS](#). Some of the delivered luminosity is not recorded because [ATLAS](#) is placed in standby until the [LHC](#) reports that the beam conditions are stable, and only then does [ATLAS](#) begin recording. The figure also includes the amount of luminosity marked as good for physics, which includes additional requirements on the operation of the detector during data collection that are necessary for precise measurements.

In addition to the instantaneous luminosity, the beam conditions also influence the number of collisions that occur within a single bunch crossing. The multiple interactions at each crossing are referred to as pileup, often denoted  $\mu$ , and each of these interactions are present in a single measured event. Figure 9 shows the luminosity-weighted distribution of the mean number of interactions for events collected in 2015. The presence of as many as 20 events in a single collision provides a significant challenge in reconstructing events and isolating the targeted physical processes.

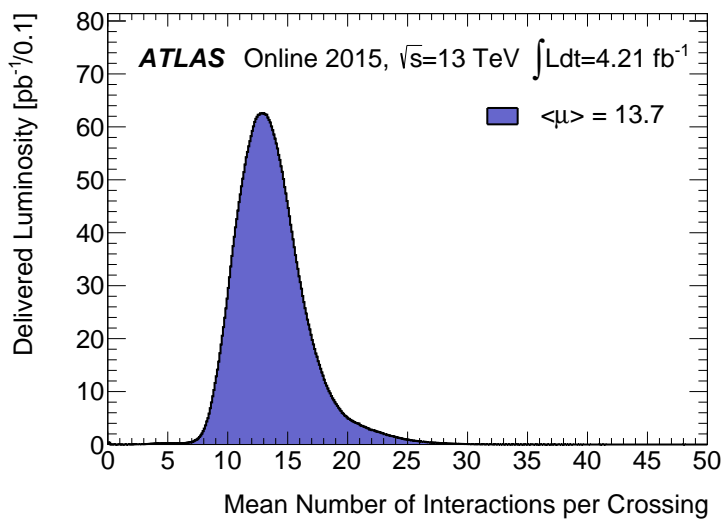


Figure 9: The luminosity-weighted distribution of the mean number of interactions per crossing for the 2015 pp collision data at 13 TeV.

817 THE ATLAS DETECTOR

---

818 The four major LHC experiments at CERN seek to use the never before matched  
819 energies and luminosities of the new collider to explore the boundaries of par-  
820 ticle physics and to gain insight into the fundamental forces of nature. Two of  
821 these experiments, ATLAS and CMS, are general purpose detectors that seek to  
822 measure a variety of processes in the up to 14 TeV proton-proton collisions that  
823 occur as much as 40 million times per second at the LHC at the design luminosity  
824 of  $10^{34} \text{ cm}^{-2}\text{s}^{-1}$ . ATLAS employs a hermetic detector design, one which encloses  
825 the particle collisions as completely as possible with detecting elements, that al-  
826 lows it to study a wide range of physics from SM and Higgs measurements to  
827 searches for new physics in models like Supersymmetry [3].

828 Accomodating this wide variety of goals is a challenge for the design of the  
829 detector. The wide range of energies involved requires high measurement preci-  
830 sion over several orders of magnitude and the ability to measure a variety of par-  
831 ticle types. At the time of the construction of ATLAS, the Higgs boson had yet to be  
832 discovered, but the diphoton decay mode was (correctly) expected to be impor-  
833 tant and necessitated a high resolution photon measurement. The potential for  
834 decays of new heavy gauge bosons, W' and Z', required a similarly high momen-  
835 tum resolution for leptons with momentum up to several TeV. Hadronic decay  
836 modes of several possible new high energy particles could result in very energetic  
837 jets, again up to several TeV, and reconstructing the decay resonances would  
838 again require good energy resolution. Several models, such as Supersymmetry  
839 (SUSY) or Extra Dimensions, predict the existence of particles which would not  
840 interact with traditional detecting elements. However these particles can still be  
841 observed in a hermetic detector by accurately measuring the remaining event  
842 constituents to observe an imbalance in energy called missing energy or  $E_T^{\text{miss}}$ .  
843 Measuring  $E_T^{\text{miss}}$  implicitly requires a good resolution on all SM particles that can  
844 be produced. And at the lower end of the energy spectrum, precision SM mea-  
845 surements would require good resolution of a variety of particle types at energies  
846 as low as a few GeV, so the design needs to accomodate roughly three orders of  
847 magnitude.

848 This broad spectrum of measurements requires a variety of detector systems  
849 working together to form a cohesive picture of each collision. Two large magnet  
850 systems provide magnetic fields that provide a curvature to the propagation of  
851 charged particles and allows for precision momentum measurements by other  
852 systems. The inner detector uses a combination of tracking technologies to re-  
853 construct particle trajectories and vertexes for charged particles. A variety of  
854 calorimeters measure the energies of hadrons, electrons, and photons over a  
855 large solid angle. A large muon spectrometer identifies muons and uses the sec-  
856 ond magnet system to provide an independent measurement of their momentum

857 from the inner detector and improve the resolution. The layout of all of these  
 858 systems is shown in Figure 10.

859 The performance goals needed to achieve the various targeted measurements  
 860 and searches discussed above can be summarized as resolution and coverage re-  
 861 quirements on each of these systems. Those requirements are listed in Table 2.

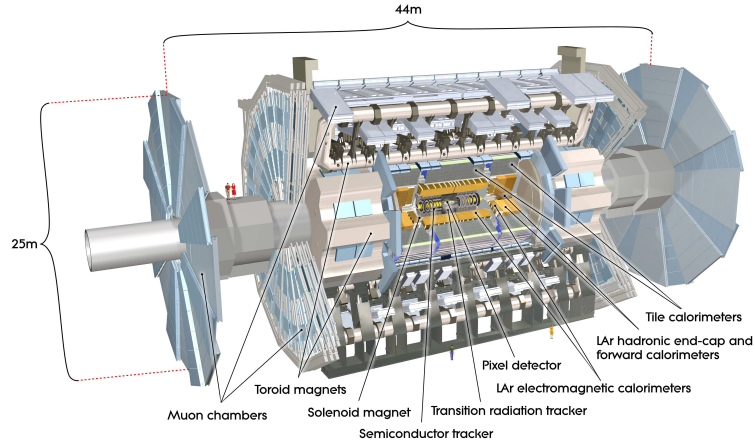


Figure 10: A cut-away schematic of the layout of the [ATLAS](#) detector. Each of the major subsystems is indicated.

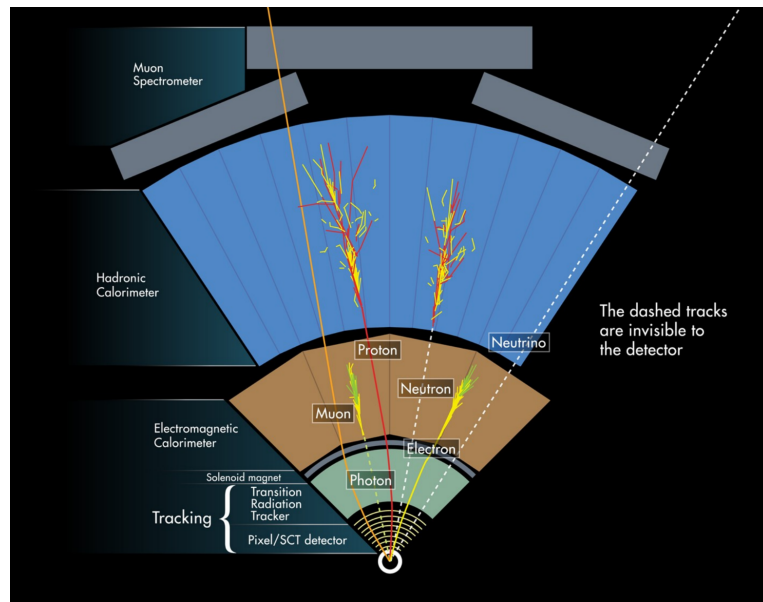


Figure 11: A cross-sectional slice of the [ATLAS](#) experiment which illustrates how the various SM particles interact with the detector systems.

862 Incorporating these various pieces into a single detector is a significant tech-  
 863 nical challenge. The resulting detector has a diameter of 22 m, is 46 m long,  
 864 and weighs 7,000 tons; it is the largest volume particle detector ever constructed.  
 865 The various detector elements need to be constructed and assembled with preci-  
 866 sions as low as micrometers. These systems all need to function well even after  
 867 exposure to the significant radiation dose from the collisions. Designing, con-

Detector Component	Required Resolution	$ \eta $ Coverage	
		Measurement	Trigger
Tracking	$\sigma_{p_T}/p_T = 0.05\% p_T + 1\%$	2.5	-
EM Calorimetry	$\sigma_E/E = 10\%/\sqrt{E} + 0.7\%$	3.2	2.5
Hadronic Calorimetry			
Barrel and End-Cap	$\sigma_E/E = 50\%/\sqrt{E} + 3\%$	3.2	3.2
Forward	$\sigma_E/E = 100\%/\sqrt{E} + 10\%$	3.1 – 4.9	3.1 – 4.9
Muon Spectrometer	$\sigma_{p_T}/p_T = 10\% \text{ at } p_T = 1 \text{ TeV}$	2.7	2.4

Table 2: The performance goals for each of the subsystems of the [ATLAS](#) detector. The  $|\eta|$  coverage specifies the range where the subsystem needs to be able to provide measurements with the specified resolution. The resolutions include a  $p_T$  or E dependence that is added in quadrature with a  $p_T/E$  independent piece.

868 structing, and installing the detector took the combined effort of more than 3000  
 869 scientists from 38 countries over almost two decades.

## 870 6.1 COORDINATE SYSTEM

871 The coordinate system defined for the [ATLAS](#) detector is used throughout all of  
 872 the sections of this thesis. The choice of coordinate system reflects the cylindri-  
 873 cal symmetry of the [ATLAS](#) detector, and is oriented by the direction of the  
 874 beamline which defines the  $z$ -direction. The positive  $z$  side of the detector is  
 875 commonly referred to as the  $A$ -side, and the negative  $z$  side is referred to as  
 876 the  $C$ -side. The  $x - y$  plane is then the plane transverse to the beam direction,  
 877 with the  $x$  direction defined as pointing from the interaction point to the center  
 878 of the [LHC](#) ring and the  $y$  direction defined as pointing upwards. The nominal  
 879 interaction point is the origin of this system.

880 It is more convenient in practice to use a cylindrical coordinate system. The  
 881 angle from the  $z$ -axis is  $\theta$ . The azimuthal angle uses the usual definition, with  $\phi$   
 882 running around the  $z$ -axis and  $\phi = 0$  corresponding to the  $x$ -axis. Many aspects  
 883 of the detector are independent of the this coordinate to first order. The re-  
 884 maining direction is typically specified using rapidity or pseudorapidity, where  
 885 rapidity is defined as

$$y = \frac{1}{2} \ln \frac{E + p_z}{E - p_z} \quad (3)$$

886 Rapidity is particularly useful to indicate the component along the  $z$  direction  
 887 because differences in rapidity are invariant to boosts along the  $z$ -direction. A  
 888 similar quantity which depends only the  $\theta$  is pseudorapidity,

$$\eta = -\ln \tan \frac{\theta}{2} \quad (4)$$

889 which is the same as rapidity when the particle is massless and in the limit where  
 890 the energy is much larger than the particle's mass. It is often useful to refer to  
 891 differences in solid angle using the pseudorapidity and the azimuthal angle:

$$\Delta R = \sqrt{\Delta\phi^2 + \Delta\eta^2} \quad (5)$$

892 The pseudorapidity is also invariant to boosts along the  $z$ -axis for high mo-  
 893 mentum particles, and is preferable to rapidity because it does not depend on  
 894 the specific choice of particle. Pseudorapidity is also preferable to  $\theta$  because  
 895 of the aforementioned boost-invariance and also because particle production is  
 896 roughly uniform in equal-width intervals of  $\eta$  up to about  $\eta = 5.0$ . A particle  
 897 travelling along the beampipe has  $\eta = \inf$  and a particle travelling perpendicular  
 898 to the beampipe has  $\eta = 0$ . The extent of the tracker,  $|\eta| < 2.5$ , corresponds  
 899 to approximately  $0.05\pi < \theta[\text{rad}] < 0.95\pi$  and the extent of the calorimeters,  
 900  $|\eta| < 4.9$  corresponds to approximately  $0.005\pi < \theta[\text{rad}] < 0.995\pi$ . Many de-  
 901 tector components are broken into multiple subsystems to provide coverage at  
 902 greater  $|\eta|$ . The lower  $|\eta|$  region is referred to as the barrel, typically with  $|\eta| \lesssim 2$ ,  
 903 and the greater  $|\eta|$  region is often referred to as the end-cap.

904 The initial energy and momentum of a proton-proton collision along the  $z$  di-  
 905 rection is unknown in hadron colliders because different energies and momen-  
 906 tums can be carried by the partons. Along the transverse plane, however, the  
 907 vector sum of momentum will be zero. For this reason, many physical quantities  
 908 are quantified in terms of their projection onto the transverse plan, such as  $p_T$   
 909 or  $E_T$ . In addition,  $p_T$  alone determines the amount of curvature in the mag-  
 910 netic field, and can be measured independently by measuring the curvature of a  
 911 particle's propagation.

## 912 6.2 MAGNETIC FIELD

913 The magnet system used in [ATLAS](#) is designed to provide a substantial magnetic  
 914 field in the two regions where the trajectory of particles is measured, the inner  
 915 detector and the muon spectrometer. The magnetic field provides a curvature  
 916 to the trajectory of charged particles and allows the precision tracking measure-  
 917 ments to make high resolutions measurements of  $p_T$ . To provide a magnetic field  
 918 in these regions, [ATLAS](#) uses a hybrid system with four separate, superconduct-  
 919 ing magnets. A single solenoid provides a 2 T axial magnetic field for the inner  
 920 detector, while a barrel toroid and two end-cap toroids produce a magnetic field  
 921 of 0.5 and 1 T, respectively, for the muon detectors. This geometry is illustrated  
 922 in Figure 12.

923 The central solenoid uses a single-layer coil with a current of 7.730 kA to gen-  
 924 erate the 2 T axial field at the center of the magnet. The single-layer coil design  
 925 enables a minimal amount of material to be used in the solenoid's construction,  
 926 which is important because the solenoid is placed between the inner detector  
 927 and the calorimeters. At normal incidence the magnet has only 0.66 radiation  
 928 lengths worth of material, where one radiation length is the mean distance over

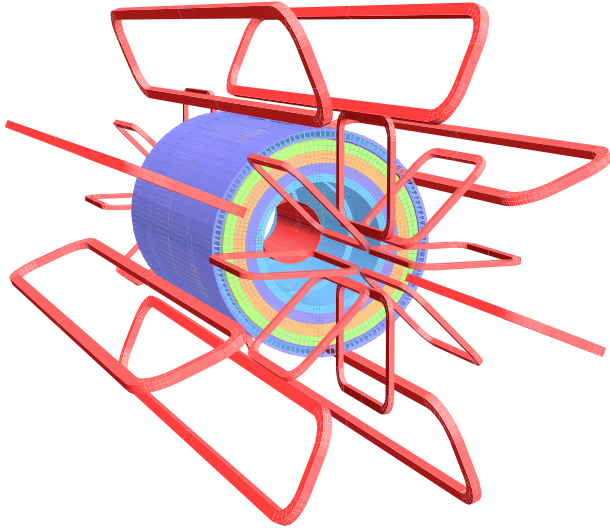


Figure 12: The layout of the four superconducting magnets in the [ATLAS](#) detector.

which a high-energy electron loses all but  $1/e$  of its energy through material interactions [7]. The coil is made of a high-strength aluminum stabilized NbTi superconductor which was optimized to achieve a high field with minimal thickness. The axial magnetic field produced by the solenoid bends charged particles in the  $\phi$  direction.

The barrel toroid consists of eight coils which generate a 0.5 T magnetic field in the cylindrical region around the calorimeters with an approximately 20 kA current. The coils are separated only by air to reduce the scattering of muons as they propagate through the region. The coils are made of an aluminum stabilized NbTiCu superconductor and each is separately housed in a vacuum and cold chamber. This magnetic configuration produces a field in the  $\phi$  and so curves muons traversing the volume primarily in the  $\eta$  direction.

The end-cap toroids follow a similar design to the barrel toroid, with eight separate NbTiCu coils, but in this case all eight are housed within a single cold mass. This extra structure is necessary to withstand the Lorentz forces exerted by the magnets. These magnets are rotated 22.5% relative to the barrel toroid to provide a uniform field in the transition between the two systems. The end-cap toroids also produce a field in the  $\phi$  direction and curve muons primarily in the  $\eta$  direction.

The major parameters of the three magnet systems are summarized in Table ??.

Parameter	Unit	Solenoid	Barrel Toroid	End-Cap Toroids
Inner Diameter	m	2.4	9.4	1.7
Outer Diameter	m	2.6	20.1	10.7
Axial Length	m	5.3	25.3	5.0
Weight	tons	5.7	830	239
Conductor Size	mm <sup>2</sup>	30×4.25	57×12	41×4.25
Peak Field	T	2.6	3.9	4.1
Heat Load	W	130	990	330
Current	kA	7.7	20.5	20.0
Stored Energy	MJ	38	1080	206

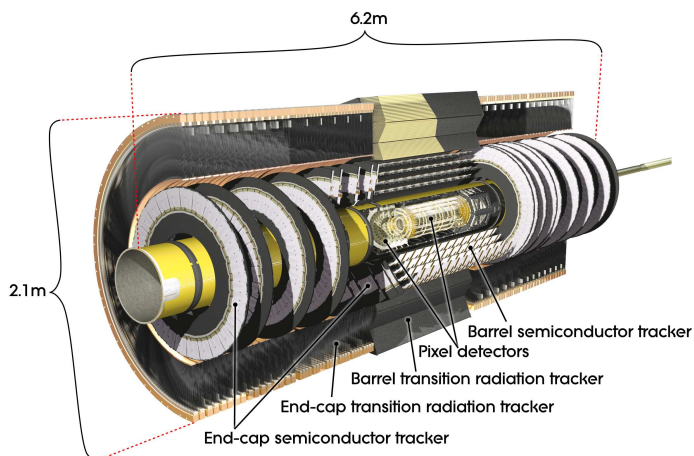


Figure 13

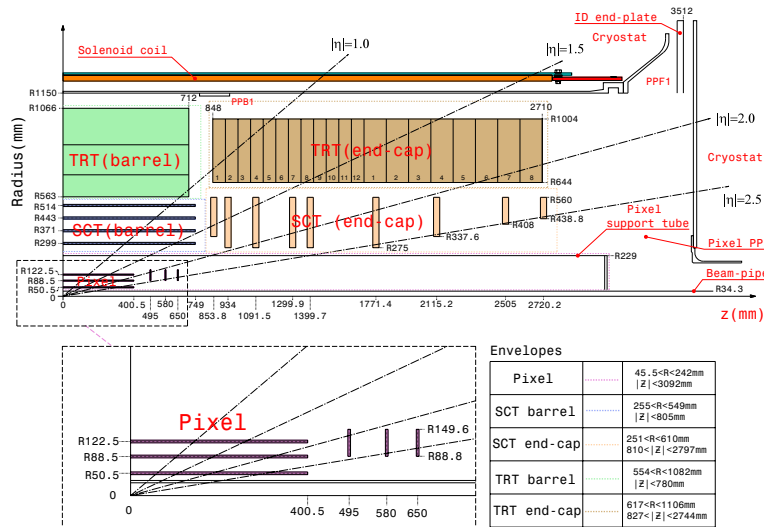


Figure 14

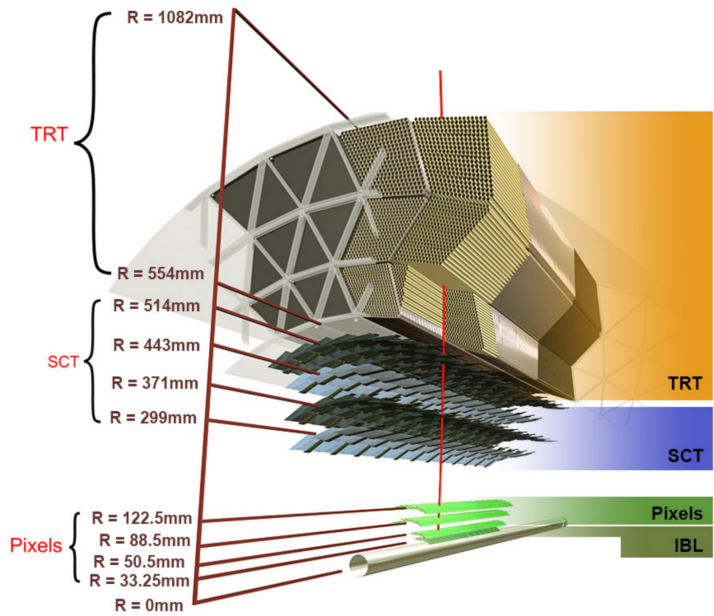


Figure 15

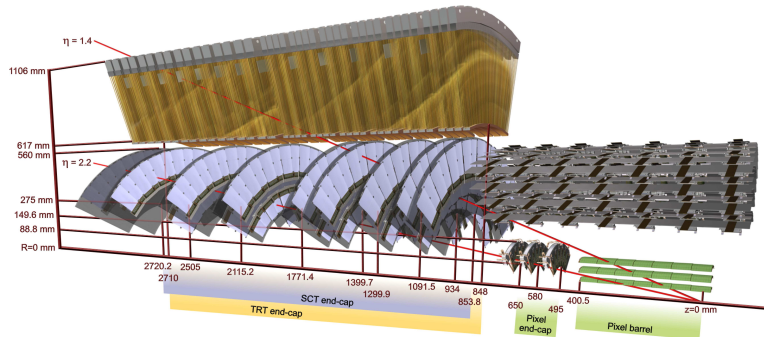


Figure 16

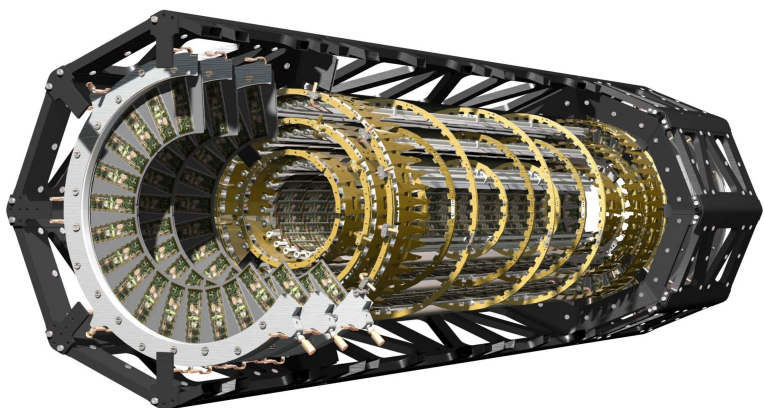


Figure 17

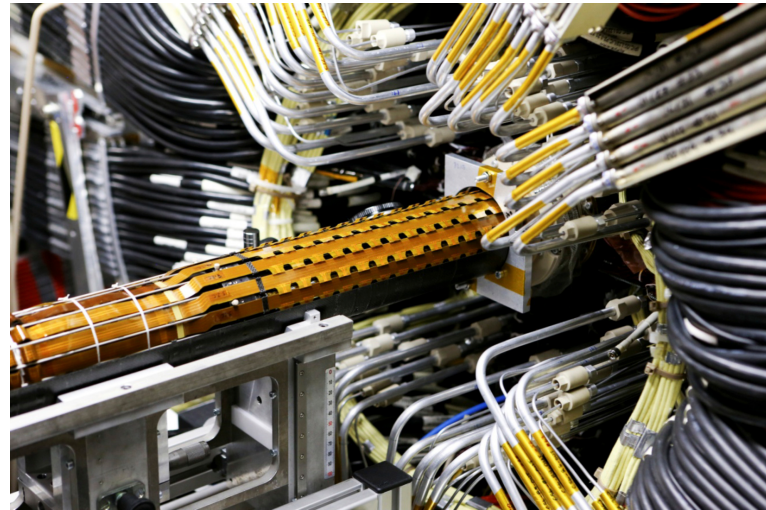


Figure 18

## 950 6.3 INNER DETECTOR

## 951 6.3.1 PIXEL DETECTOR

## 952 6.3.2 SEMICONDUCTOR TRACKER

## 953 6.3.3 TRANSITION RADIATION TRACKER

## 954 6.4 CALORIMETRY

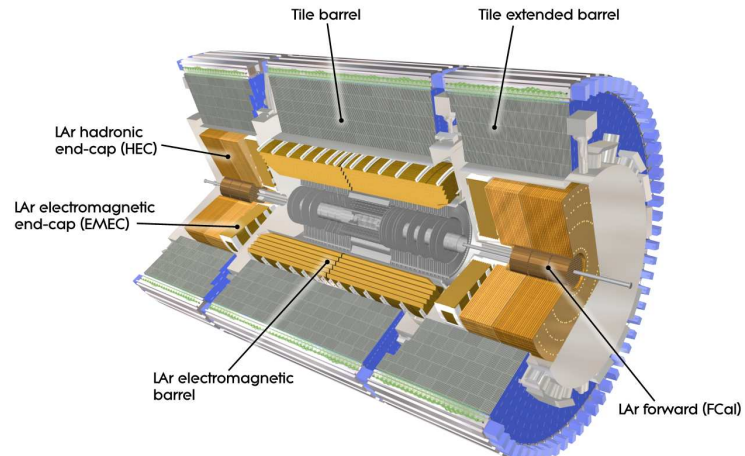


Figure 19

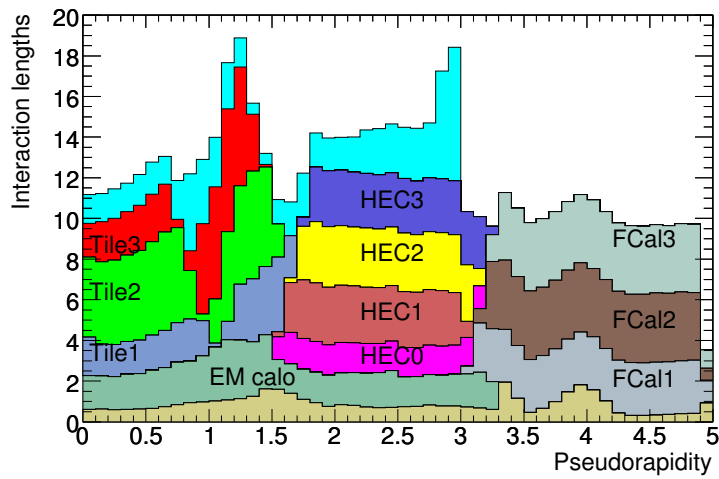


Figure 20

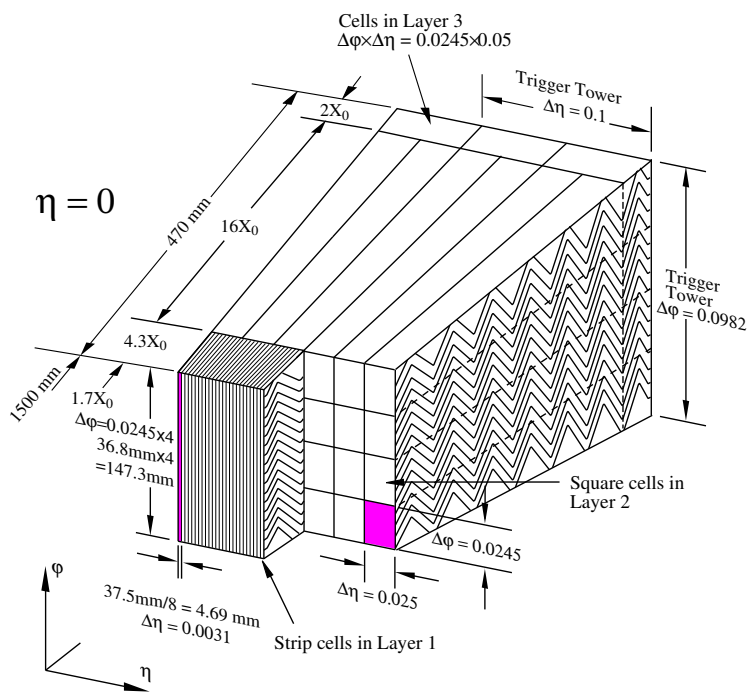


Figure 21

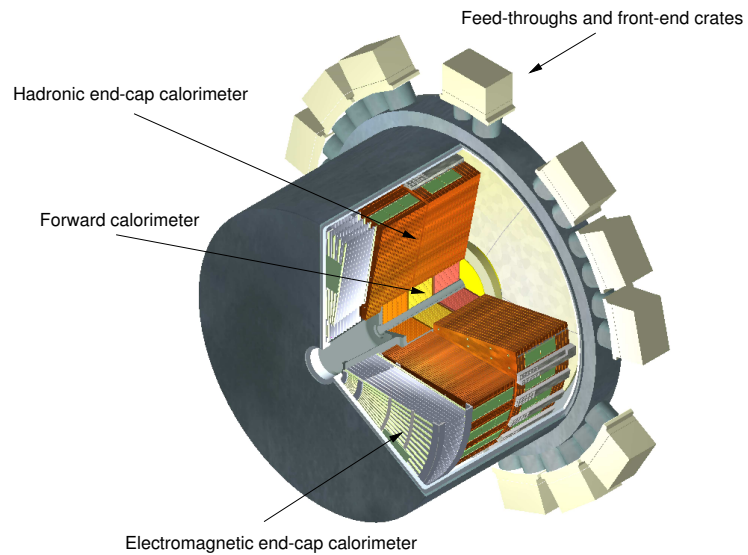


Figure 22

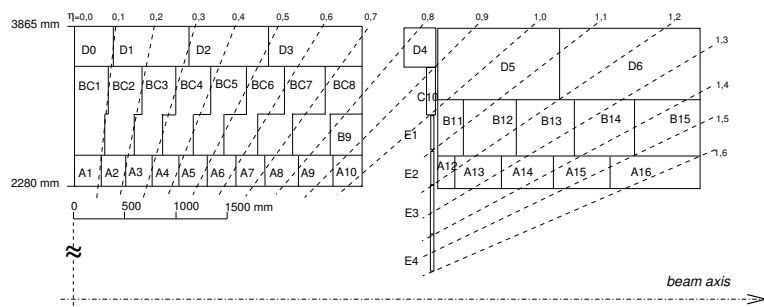


Figure 23

955 6.4.1 ELECTROMAGNETIC CALORIMETERS

956 6.4.2 HADRONIC CALORIMETERS

957 6.4.3 FORWARD CALORIMETERS

958 6.5 MUON SPECTROMETER

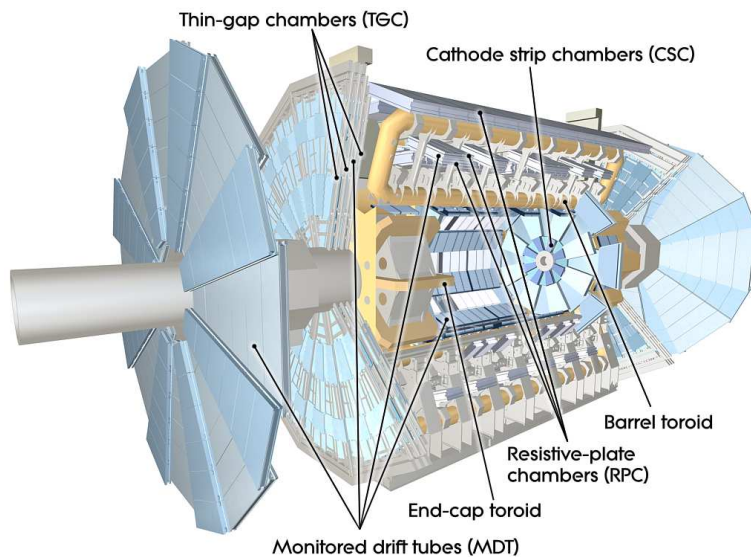


Figure 24

959 6.6 TRIGGER

960 6.6.1 TRIGGER SCHEME

961 6.6.2 MISSING TRANSVERSE ENERGY TRIGGERS

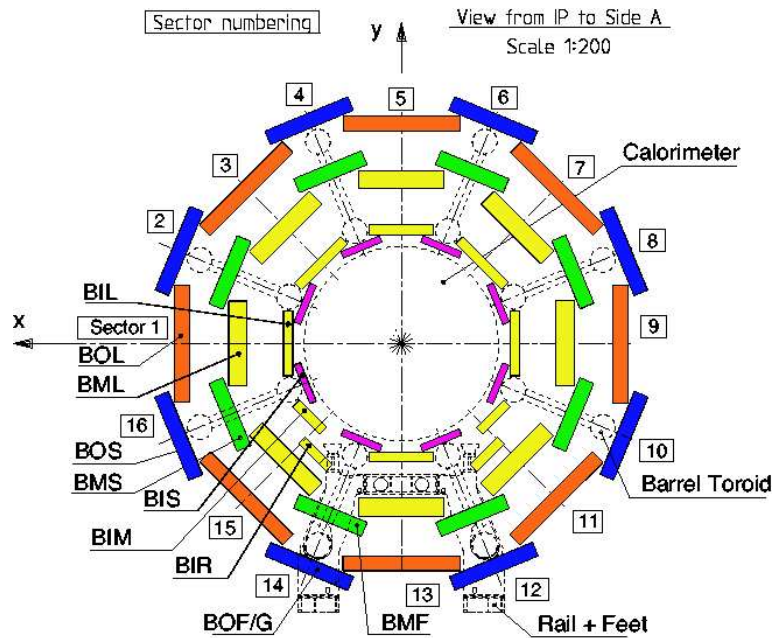


Figure 25

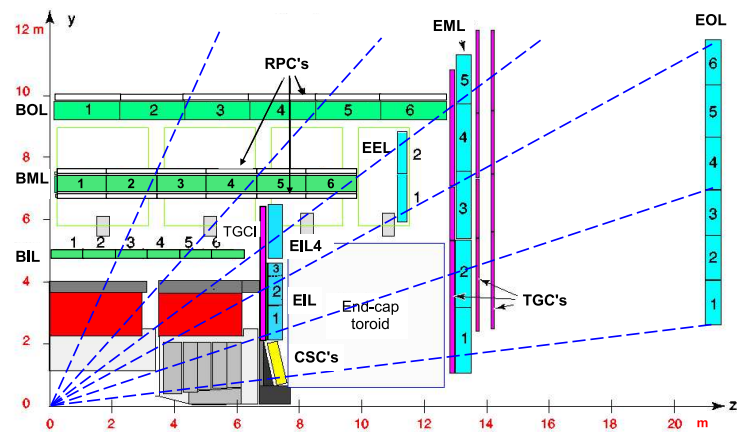


Figure 26

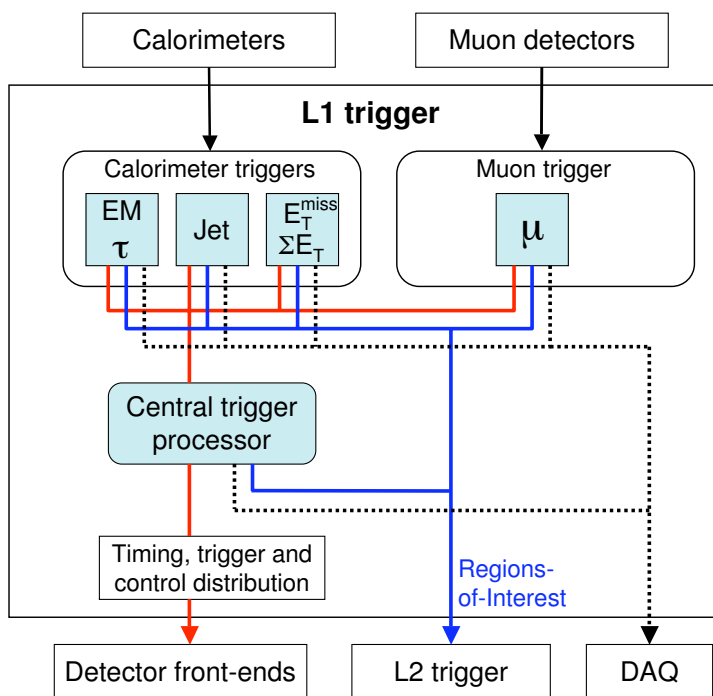


Figure 27



# 7

962

## 963 EVENT RECONSTRUCTION

---

964 The ATLAS experiment combines measurements in the subdetectors to form a  
965 cohesive picture of each physics event.

## 966 7.1 TRACKS AND VERTICES

### 967 7.1.1 TRACK RECONSTRUCTION

#### 968 7.1.1.1 NEURAL NETWORK

#### 969 7.1.1.2 PIXEL DE/DX

### 970 7.1.2 VERTEX RECONSTRUCTION

## 971 7.2 JETS

### 972 7.2.1 TOPOLOGICAL CLUSTERING

### 973 7.2.2 JET ENERGY SCALE

### 974 7.2.3 JET ENERGY SCALE UNCERTAINTIES

### 975 7.2.4 JET ENERGY RESOLUTION

## 976 7.3 ELECTRONS

### 977 7.3.1 ELECTRON IDENTIFICATION

## 978 7.4 MUONS

### 979 7.4.1 MUON IDENTIFICATION

## 980 7.5 MISSING TRANSVERSE ENERGY



981

## PART IV

982

### CALORIMETER RESPONSE

983

You can put some informational part preamble text here.



984

985 RESPONSE MEASUREMENT WITH SINGLE HADRONS

---

986 As discussed in Section 7.2, colored particles produced in collisions hadronize  
987 into jets of multiple hadrons. One approach to understanding jet energy mea-  
988 surements in the ATLAS calorimeters is to evaluate the calorimeter response to  
989 those individual hadrons; measurements of individual hadrons can be used to  
990 build up an understanding of the jets that they form. The redundancy of the  
991 momentum provided by the tracking system and the energy provided by the  
992 calorimeter provides an opportunity to study calorimeter response using real  
993 collisions, as described further in Section 8.2.

994 Calorimeter response includes a number of physical effects that can be ex-  
995 tracted to provide insight into many aspects of jet modeling. First, many charged  
996 hadrons interact with the material of the detector prior to reaching the calorime-  
997 ters and thus do not deposit any energy. Comparing this effect in data and simu-  
998 lation is a powerful tool in validating the interactions of particles with the mate-  
999 rial of the detector and the model of the detector geometry in simulation, see Sec-  
1000 tion 8.2.2. The particles which do reach the calorimeter deposit their energy into  
1001 several adjacent cells, which are then clustered together. The energy of the clus-  
1002 ter is then the total energy deposited by that particle. Comparing the response of  
1003 hadrons in data to that of simulated hadrons provides a direct evaluation of the  
1004 showering of hadronic particles and the energy deposited by particles in matter  
1005 (Section 8.2.4).

1006 The above studies all use an inclusive selection of charged particles, which are  
1007 comprised predominantly of pions, kaons, and (anti)protons. It is also possible to  
1008 measure the response to various identified particle types separately to evaluate  
1009 the simulated interactions of each particle, particularly at low energies where  
1010 differences between species are very relevant. Pions and (anti)protons can be  
1011 identified through decays of long-lived particles, in particular  $\Lambda$ ,  $\bar{\Lambda}$ , and  $K_S^0$ , and  
1012 then used to measure response as described above. This is discussed in detail in  
1013 Section 8.3.

1014 The results in this chapter use data collected at 7 and 8 TeV collected in 2010  
1015 and 2012, respectively. Both are included as the calorimeter was repaired and  
1016 recalibrated between those two data-taking periods. Both sets of data are com-  
1017 pared to an updated simulation that includes new physics models provided by  
1018 Geant4 [8] and improvements in the detector description [9, 10]. The present  
1019 results are published in European Physical Journal C (EPJC) [11] and can be com-  
1020 pared to a similar measurement performed in 2009 and 2010 [12], which used  
1021 the previous version of the simulation framework [13].

## 1022 8.1 DATASET AND SIMULATION

## 1023 8.1.1 DATA SAMPLES

1024 The two datasets used in this chapter are taken from dedicated low-pileup runs  
 1025 where the fraction of events with multiple interactions was negligible. These  
 1026 datasets are used rather than those containing full-pileup events to facilitate mea-  
 1027 surement of isolated hadrons. The 2012 dataset at  $\sqrt{s} = 8$  TeV contains 8 mil-  
 1028 lion events and corresponds to an integrated luminosity of  $0.1 \text{ nb}^{-1}$ . The 2010  
 1029 dataset at  $\sqrt{s} = 7$  TeV contains 3 million events and corresponds to an inte-  
 1030 grated luminosity of  $3.2 \text{ nb}^{-1}$ . The latter dataset was also used for the 2010 re-  
 1031 sults [12], but it has since been reanalyzed with an updated reconstruction in-  
 1032 cluding the final, best understanding of the detector description for the material  
 1033 and alignment from Run 1.

## 1034 8.1.2 SIMULATED SAMPLES

1035 The two datasets above are compared to simulated single-, double-, and non-  
 1036 diffractive events generated with Pythia8 [14] using the A2 configuration of  
 1037 hadronization [15] and the MSTW 2008 parton-distribution function set [16,  
 1038 17]. The admixture of the single-, double-, and non-diffractive events uses the  
 1039 default relative contributions from Pythia8. The conditions and energies for  
 1040 the two simulations are chosen so that they match those of the corresponding  
 1041 dataset.

1042 To evaluate the interaction of hadrons with detector material, the simulation  
 1043 uses two different collections of hadronic physics models, called physics lists, in  
 1044 Geant4 9.4 [18]. The first, QGSP\_BERT, combines the Bertini intra-nuclear  
 1045 cascade [19–21] below 9.9 GeV, a parametrized proton inelastic model from 9.5  
 1046 to 25 GeV [22], and a quark-gluon string model above 12 GeV [23–27]. The  
 1047 second, FTFP\_BERT, combines the Bertini intra-nuclear cascade [19–21] below  
 1048 5 GeV and the Fritiof model [28–31] above 4 GeV. In either list, Geant4 en-  
 1049 forces a smooth transition between models where multiple models overlap.

## 1050 8.1.3 EVENT SELECTION

1051 The event selection for this study is minimal, as the only requirement is selecting  
 1052 good-quality events with an isolated track. Such events are triggered by requir-  
 1053 ing at least two hits in the minimum-bias trigger scintillators. After trigger, each  
 1054 event is required to have exactly one reconstructed vertex, and that vertex is re-  
 1055 quired to have four or more associated tracks.

1056 The particles which are selected for the response measurements are first iden-  
 1057 tified as tracks in the inner detector. The tracks are required to have at least 500  
 1058 MeV of transverse momentum. To ensure a reliable momentum measurement,  
 1059 these tracks are required to have at least one hit in the pixel detector, six hits in  
 1060 the SCT, and small longitudinal and transverse impact parameters with respect  
 1061 to the primary vertex [12]. For the majority of the measurements in this chapter,

1062 the track is additionally required to have 20 hits in the TRT, which significantly  
 1063 reduces the contribution from tracks which undergo nuclear interactions. This  
 1064 requirement and its effect is discussed in more detail in Section 8.2.5. In addition,  
 1065 tracks are rejected if there is any other reconstructed track which extrapolates  
 1066 to the calorimeter within a cone of  $\Delta R = \sqrt{(\Delta\phi)^2 + (\Delta\eta)^2} < 0.4$ . This require-  
 1067 ment guarantees that the contamination of energy from nearby charged particles  
 1068 is negligible [12].

## 1069 8.2 INCLUSIVE HADRON RESPONSE

1070 The calorimeter response is more precisely defined as the ratio of the measured  
 1071 calorimeter energy to the true energy carried by the particle, although this true  
 1072 energy is unknown. For charged particles, however, the inner detector provides  
 1073 a very precise measurement of momentum (with uncertainty less than 1%) that  
 1074 can be used as a proxy for true energy. The ratio of the energy deposited by  
 1075 the charged particle in the calorimeter,  $E$ , to its momentum measured in the  
 1076 inner detector  $p$ , forms the calorimeter response measure called  $E/p$ . Though  
 1077 the distribution of  $E/p$  contains a number of physical features, this study focuses  
 1078 on the trends in two aggregated quantities:  $\langle E/p \rangle$ , the average of  $E/p$  for the  
 1079 selected tracks, and the zero fraction, the fraction of tracks with no associated  
 1080 energy in the calorimeter for those tracks.

1081 The calorimeter energy assigned to a track is defined using clusters. The clus-  
 1082 ters are formed using a 4–2–0 algorithm [32] that begins with seeds requiring  
 1083 at least 4 times the average calorimeter cell noise. The neighboring cells with  
 1084 at least twice that noise threshold are then added to the cluster, and all bound-  
 1085 ing cells are then added with no requirement. This algorithm minimizes noise  
 1086 contributions through its seeding process, and including the bounding cells im-  
 1087 proves the energy resolution [33]. The clusters are associated to a given track  
 1088 if they fall within a cone of  $\Delta R = 0.2$  of the extrapolated position of the track,  
 1089 which includes about 90% of the energy on average [12]. This construction is  
 1090 illustrated in Figure 28.

### 1091 8.2.1 E/P DISTRIBUTION

1092 The  $E/p$  distributions measured in both data and simulation are shown in Fig-  
 1093 ure 29 for two example bins of track momentum and for tracks in the central  
 1094 region of the detector. These distributions show several important features of  
 1095 the  $E/p$  observable. The large content in the bin at  $E = 0$  comes from tracks that  
 1096 have no associated cluster, which occurs due to interactions with detector mate-  
 1097 rial prior to reaching the calorimeter or the energy deposit being insufficiently  
 1098 large to generate a seed, and are discussed in Section 8.2.2. The small negative  
 1099 tail also comes from tracks that do not deposit any energy in the calorimeter but  
 1100 are randomly associated to a cluster with an energy below the noise threshold.  
 1101 The long positive tail above 1.0 comes from the contribution of neutral parti-  
 1102 cles. Nearby neutral particles deposit (sometimes large) additional energy in the  
 1103 calorimeter but do not produce tracks in the inner detector, so they cannot be

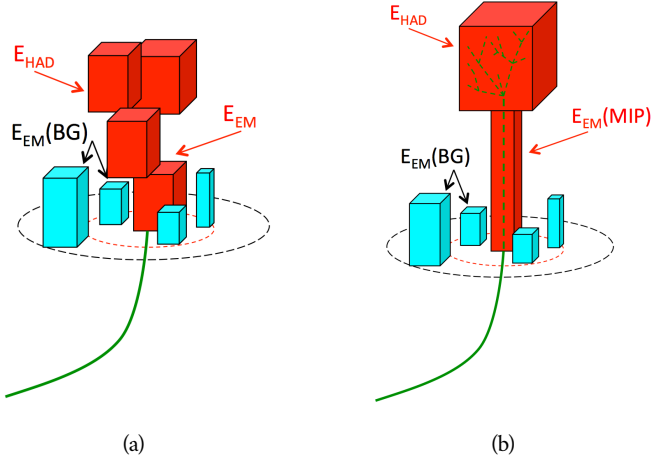


Figure 28: An illustration (a) of the  $E/p$  variable used throughout this paper. The red energy deposits come from the charged particle targeted for measurement, while the blue energy deposits are from nearby neutral particles and must be subtracted. The same diagram (b) for the neutral-background selection, described in Section 8.2.3.

1104 rejected by the track isolation requirement. Additionally the peak and mean of  
1105 the distribution falls below 1.0 because of the loss of energy not found within  
1106 the cone as well as the non-compensation of the calorimeter.

The data and simulation share the same features, but the high and low tails are significantly different. The simulated events tend to overestimate the contribution of neutral particles to the long tail, an effect which can be isolated and removed as discussed in Section 8.2.3. Additionally, the simulated clusters have less noise on average, although this is a small effect on the overall response.

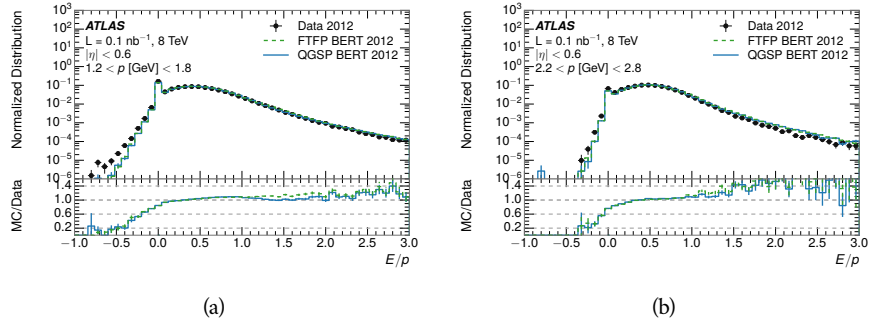


Figure 29: The  $E/p$  distribution and ratio of simulation to data for isolated tracks with (a)  $|\eta| < 0.6$  and  $1.2 < p/\text{GeV} < 1.8$  and (b)  $|\eta| < 0.6$  and  $2.2 < p/\text{GeV} < 2.8$ .

1112 8.2.2 ZERO FRACTION

1113 The fraction of particles with no associated clusters, or similarly those with  $E \leq$   
 1114 0, reflects the modeling of both the detector geometry and hadronic interactions.

1115 The zero fraction is expected to rise as the amount of material a particle traverses  
 1116 increases, while it is expected to decrease as the particle energy increases. This  
 1117 dependence can be seen in Figure 30, where the zero fraction in data and simulation  
 1118 is shown as a function of momentum and the amount of material measured  
 1119 in interaction lengths. The trends are similar between 2010 and 2012 and for  
 1120 positively and negatively charged particles. The zero fraction decreases with  
 1121 energy as expected. The absolute discrepancy in zero fraction decreases with  
 1122 momentum from 5% to less than 1%, but this becomes more pronounced in the  
 1123 ratio as the zero fraction shrinks quickly with increasing momentum. There is  
 1124 a small constant difference between the data and simulation in both interaction  
 1125 models that becomes more pronounced. The amount of material in the detector  
 1126 increases with  $\eta$ , which is used to obtain results for interaction lengths ranging  
 1127 between 0.1 and 0.65  $\lambda$ . As the data and simulation have significant disagree-  
 1128 ment in the zero fraction over a number of interaction lengths, the difference  
 1129 must be primarily from the modeling of hadronic interactions with detector ma-  
 1130 terial and not just the detector geometry. Although two different hadronic in-  
 1131 teraction models are shown in the figure, they have very similar discrepancies to  
 1132 data because both use the same description (the BERT model) at low momentum.

### 1133 8.2.3 NEUTRAL BACKGROUND SUBTRACTION

1134 The isolation requirement on hadrons is only effective in removing an energy  
 1135 contribution from nearby charged particles. Nearby neutral particles, predomi-  
 1136 nantly photons from  $\pi^0$  decays, also add their energy to the calorimeter clusters,  
 1137 but mostly in the electromagnetic calorimeter. It is possible to measure this con-  
 1138 tribution, on average, using late-showering hadrons that minimally ionize in the  
 1139 electromagnetic calorimeter. Such particles are selected by requiring that they  
 1140 deposit less than 1.1 GeV in the EM calorimeter within a cone of  $\Delta R < 0.1$   
 1141 around the track. To ensure that these particles are well measured, they are addi-  
 1142 tionally required to deposit between 40% and 90% of their energy in the hadronic  
 1143 calorimeter within the same cone.

1144 These particles provide a clean sample to measure the nearby neutral back-  
 1145 ground because they do not deposit energy in the area immediately surrounding  
 1146 them in the EM calorimeter, as shown in Figure 28. So, the energy deposits in the  
 1147 region  $0.1 < \Delta R < 0.2$  can be attributed to neutral particles alone. To estimate  
 1148 the contribution to the whole cone considered for the response measurement,  
 1149 that energy is scaled by a geometric factor of  $4/3$ . This quantity,  $\langle E/p \rangle_{\text{BG}}$ , mea-  
 1150 sured in aggregate over a number of particles, gives the contribution to  $\langle E/p \rangle$   
 1151 from neutral particles in the EM calorimeter. Similar techniques were used in  
 1152 the individual layers of the hadronic calorimeters to show that the background  
 1153 from neutrals is negligible in those layers [12].

1154 The distribution of this background estimate is shown in Figure 31 for data  
 1155 and simulation with the two different physics lists. The contribution from neu-  
 1156 tral particles falls from 0.1 at low momentum to around 0.03 for particles above  
 1157 7 GeV. Although the simulation captures the overall trend, it significantly over-  
 1158 estimates the neutral contribution for tracks with momentum between 2 and 8

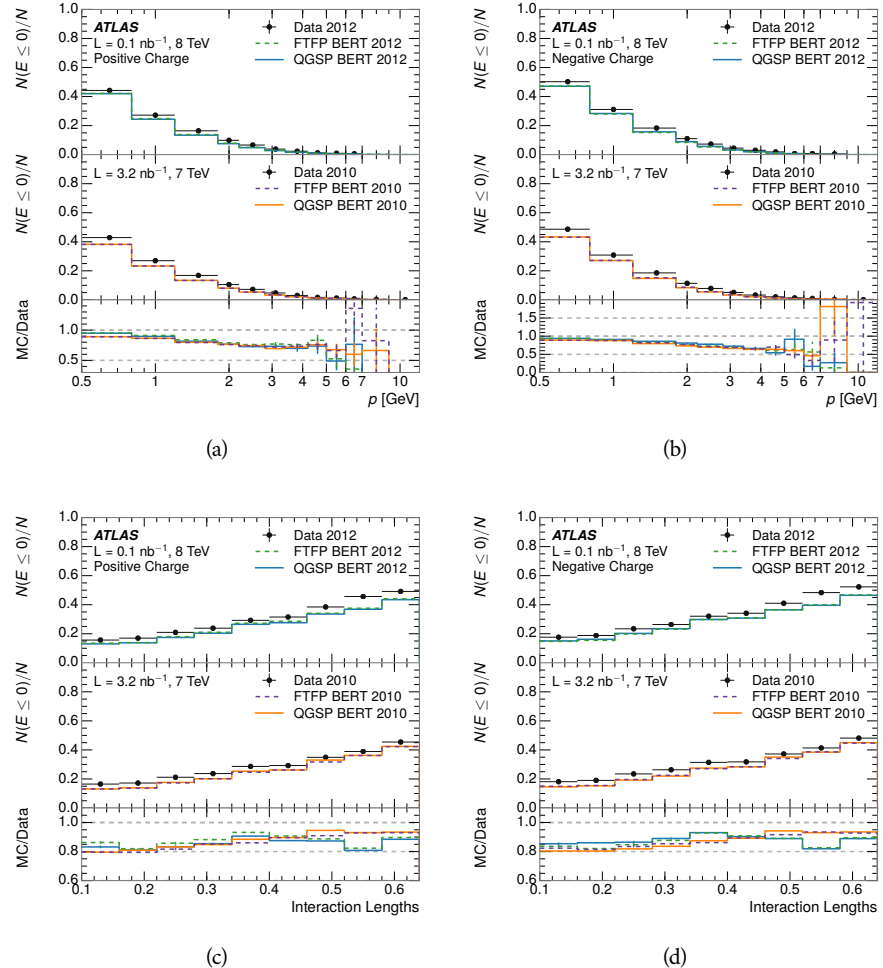


Figure 30: The fraction of tracks as a function (a, b) of momentum, (c, d) of interaction lengths with  $E \leq 0$  for tracks with positive (on the left) and negative (on the right) charge.

1159 GeV. This effect was also seen in the tails of the  $E/p$  distributions in Figure 29.  
 1160 This difference is likely due to modeling of coherent neutral particle radiation  
 1161 in **Pythia8** that overestimates the production of  $\pi^0$  near the production of the  
 1162 charged particles. The discrepancy does not depend on  $\eta$  and thus is unlikely to  
 1163 be a mismodeling of the detector. This difference can be subtracted to form a  
 1164 corrected average  $E/p$ , as in Section 8.2.4.

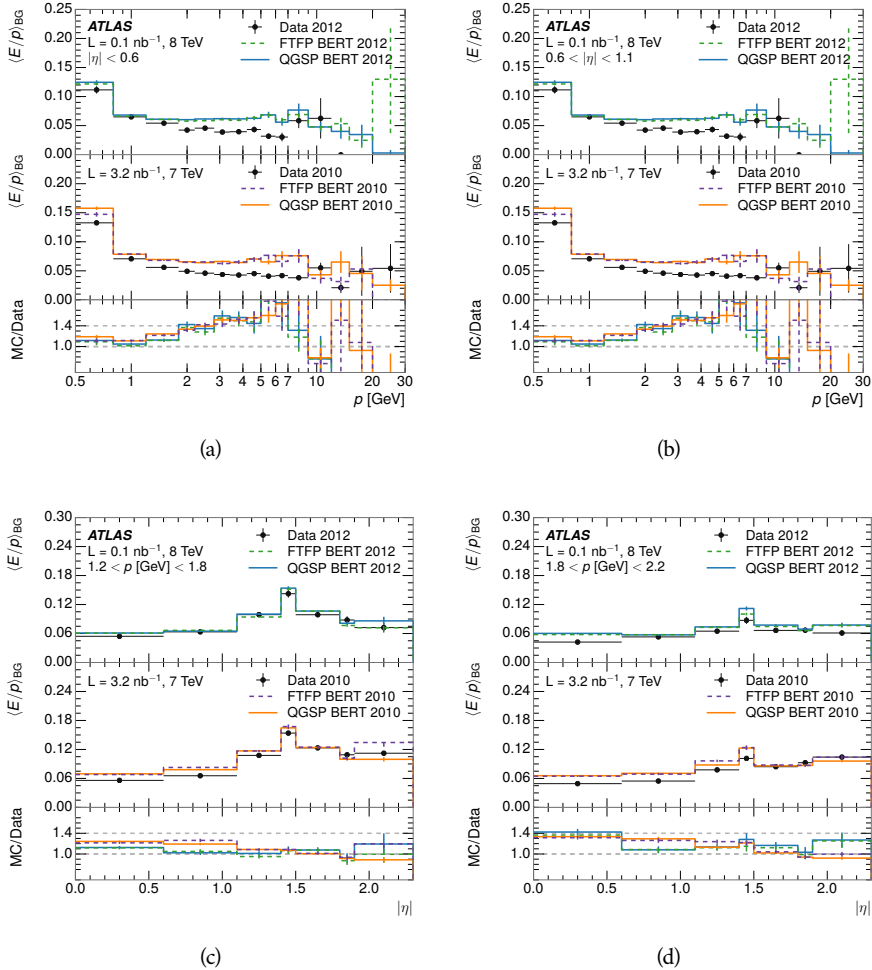


Figure 31:  $\langle E/p \rangle_{BG}$  as a function of the track momentum for tracks with (a)  $|\eta| < 0.6$ ,  
 (b)  $0.6 < |\eta| < 1.1$ , and as a function of the track pseudorapidity for tracks  
 with (c)  $1.2 < p/\text{GeV} < 1.8$ , (d)  $1.8 < p/\text{GeV} < 2.2$ .

#### 1165 8.2.4 CORRECTED RESPONSE

1166 Figure 32 shows  $\langle E/p \rangle_{COR}$  as a function of momentum for several bins of pseudo-  
 1167 rapidity. This corrected  $\langle E/p \rangle_{COR} \equiv \langle E/p \rangle - \langle E/p \rangle_{BG}$  measures the average  
 1168 calorimeter response without the contamination of neutral particles. It is the  
 1169 most direct measurement of calorimeter response in that it is the energy mea-  
 1170 sured for fully isolated hadrons. The correction is performed separately in data  
 1171 and simulation, so that the mismodeling of the neutral background in simulation

is removed from the comparison of response. The simulation overestimates the response at low momentum by about 5%, an effect that can be mostly attributed to the underestimation of the zero fraction mentioned previously. For  $|\eta| < 0.6$ , the data-simulation agreement has a larger discrepancy by about 5% for 2010 than 2012, although this is not reproduced in at higher pseudorapidity.

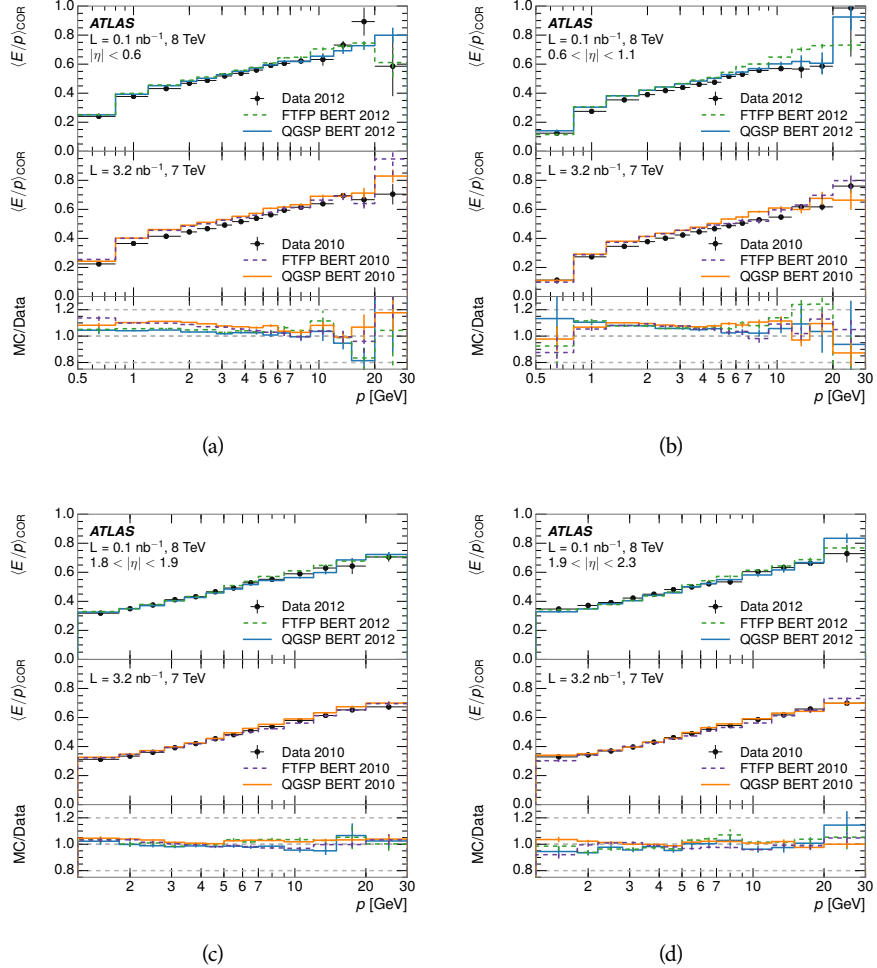


Figure 32:  $\langle E/p \rangle_{\text{COR}}$  as a function of track momentum, for tracks with (a)  $|\eta| < 0.6$ , (b)  $0.6 < |\eta| < 1.1$ , (c)  $1.8 < |\eta| < 1.9$ , and (d)  $1.9 < |\eta| < 2.3$ .

The response measurement above used topological clustering at the EM scale, that is clusters were formed to measure energy but no corrections were applied to correct for expected effects like energy lost outside of the cluster or in uninstrumented material. It is also interesting to measure  $\langle E/p \rangle_{\text{COR}}$  using local cluster weighted (LCW) energies, which accounts for those effects by calibrating the energy based on the properties of the cluster such as energy density and depth in the calorimeter. Figure 33 shows these distributions for tracks with zero or more clusters and separately for tracks with one or more clusters. The calibration moves the mean value of  $\langle E/p \rangle_{\text{COR}}$  significantly closer to 1.0 as desired. The agreement between data and simulation improves noticeably when at least one cluster is required, as this removes the contribution from the mismodeling of

1188 the zero fraction. The good agreement in that case again demonstrates that the  
 1189 difference in  $\langle E/p \rangle_{\text{COR}}$  between data and simulation is caused predominantly  
 1190 by the difference in zero fraction.

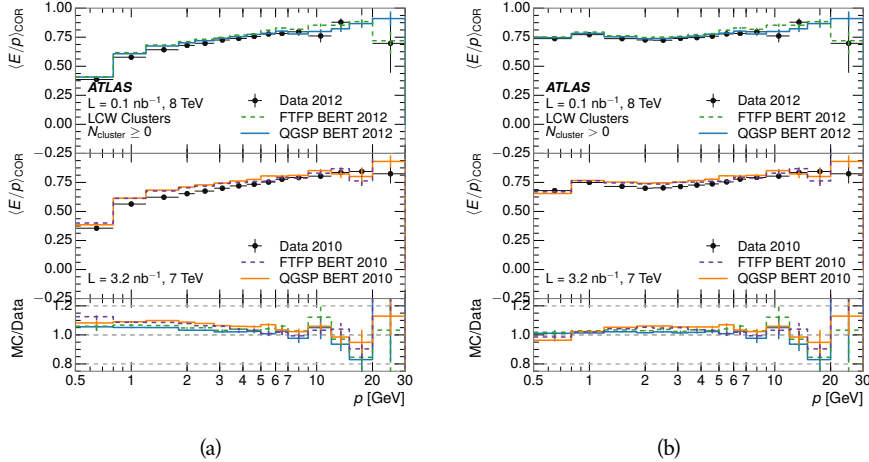


Figure 33:  $\langle E/p \rangle_{\text{COR}}$  calculated using LCW-calibrated topological clusters as a function of track momentum for tracks with (a) zero or more associated topological clusters or (b) one or more associated topological clusters.

### 1191 8.2.5 ADDITIONAL STUDIES

1192 As has been seen in several measurements in previous sections, the simulation  
 1193 does not correctly model the chance of a low momentum hadron to reach the  
 1194 calorimeter. Because of the consistent discrepancy across pseudorapidity and  
 1195 interaction lengths, this can be best explained by incomplete understanding of  
 1196 hadronic interactions with the detector [11]. For example, a hadron that scat-  
 1197 ters off of a nucleus in the inner detector can be deflected through a significant  
 1198 angle and not reach the expected location in the calorimeter. In addition, these  
 1199 interactions can produce secondary particles that are difficult to model.

1200 The requirement used throughout the previous sections on the number of  
 1201 hits in the TRT reduces these effects by preferentially selecting tracks that do  
 1202 not undergo nuclear interactions. It is interesting to check how well the sim-  
 1203 ulation models tracks with low numbers of TRT hits, which selects tracks that  
 1204 are more likely to have undergone a hadronic interaction. Figure 34 compares  
 1205 the distributions with  $N_{\text{TRT}} < 20$  to  $N_{\text{TRT}} > 20$  for real and simulated particles.  
 1206 As expected, the tracks with fewer hits are poorly modeled in the simulation as  
 1207  $\langle E/p \rangle_{\text{COR}}$  differs by as much as 25% at low momentum.

1208 Another interesting aspect of the simulation is the description of antiprotons  
 1209 at low momentum, where QGSP\_BERT and FTFP\_BERT have significant differ-  
 1210 ences. This can be seen to have an effect in the inclusive response measurement  
 1211 when separated into positive and negative charge. The  $\langle E/p \rangle_{\text{COR}}$  distributions  
 1212 for positive and negative particles are shown in Figure 35, where a small differ-  
 1213 ence between QGSP\_BERT and FTFP\_BERT can be seen in the distribution for

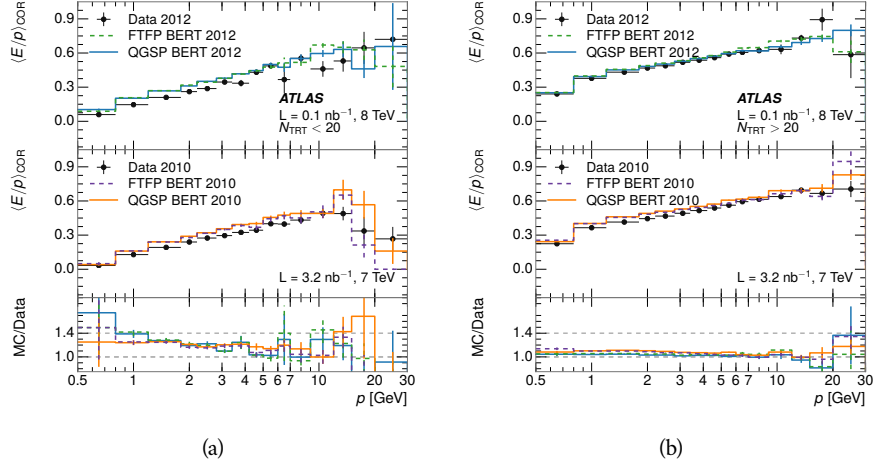


Figure 34: Comparison of the  $\langle E/p \rangle_{\text{COR}}$  for tracks with (a) less than and (b) greater than 20 hits in the TRT.

negative tracks. This is demonstrated more clearly in Figure 36, which shows the  $E/p$  distribution in the two simulations separated by charge. There is a clear difference around  $E/p > 1.0$ , which can be explained by the additional energy deposited by the annihilation of the antiproton in the calorimeter that is modeled well only in FTFP\_BERT. This is also explored with data using identified antiprotons in Section 8.3.

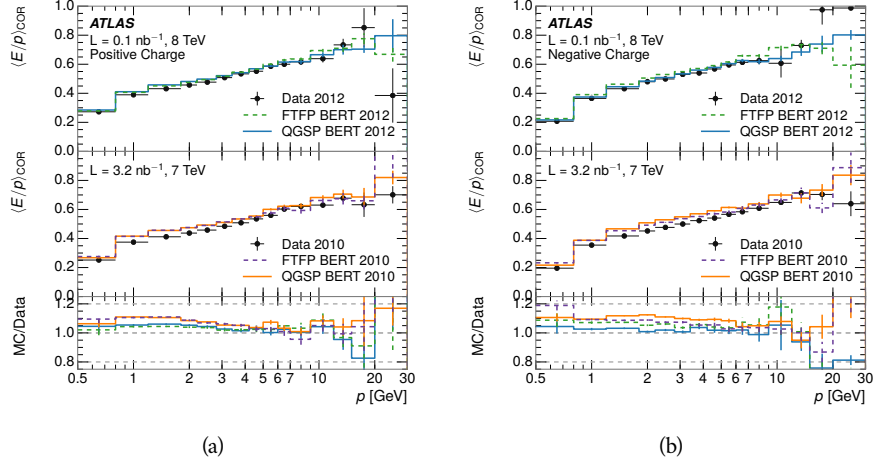


Figure 35: Comparison of the  $\langle E/p \rangle_{\text{COR}}$  for (a) positive and (b) negative tracks as a function of track momentum for tracks with  $|\eta| < 0.6$ .

The  $\langle E/p \rangle$  results in previous sections have considered the electromagnetic and hadronic calorimeters together as a single energy measurement, to emphasize the total energy deposited for a given particle. However, the deposits in each calorimeter are available separately and  $\langle E/p \rangle$  can be constructed for each layer. As the layers are composed of different materials and are modeled separately in the detector geometry, confirmation that the simulation matches the data well

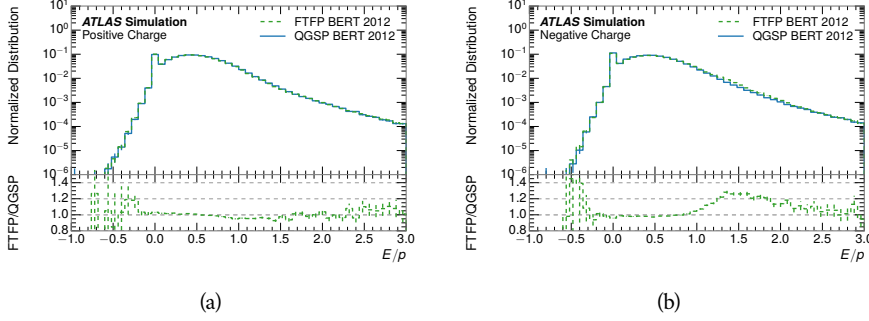


Figure 36: Comparison of the  $E/p$  distributions for (a) positive and (b) negative tracks with  $0.8 < p/\text{GeV} < 1.2$  and  $|\eta| < 0.6$ , in simulation with the FTFP\_BERT and QGSP\_BERT physics lists.

in each layer adds confidence in both the description of hadronic interactions with the two different materials and also the geometric description of each.

The technique discussed in Section 8.2.3 for selecting minimally ionizing particle (MIP)s in the electromagnetic calorimeter is also useful in studying deposits in the hadronic calorimeter. Those MIPs deposit almost all of their energy exclusively in the hadronic calorimeter. Figure 37 shows  $\langle E/p \rangle_{\text{RAW}}^{\text{Had}}$ , where RAW indicates that no correction has been applied for neutral backgrounds and Had indicates that only clusters for the hadronic calorimeter are included. The RAW and COR versions of  $\langle E/p \rangle$  in this case are the same, as the neutral background is negligible in that calorimeter layer. The distributions are shown both for the original EM scale calibration and after LCW calibration. The data and simulation agree very well in this comparison, except in the lowest momentum bin which has 5% discrepancy that has already been seen in similar measurements.

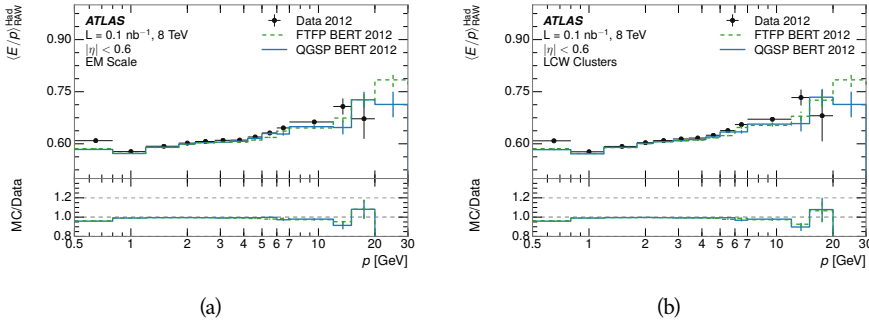


Figure 37: Comparison of the response of the hadronic calorimeter as a function of track momentum (a) at the EM-scale and (b) after the LCW calibration.

A similar comparison can be made in the electromagnetic calorimeter by selecting particles which have no associated energy in the hadronic calorimeter. These results are measured in terms of  $\langle E/p \rangle_{\text{COR}}^{\text{EM}}$ , where EM designates that only clusters in the electromagnetic calorimeter are included and COR designates that the neutral background is subtracted as the neutral background is present in this case. Figure 38 shows the analogous comparisons to Figure 37 in

1245 the electromagnetic calorimeter. In this case the disagreement between data and  
 1246 simulation is more pronounced, with discrepancies as high as 5% over a larger  
 1247 range of momenta. This level of discrepancy indicates that the description of  
 1248 the electromagnetic calorimeter is actually the dominant source of discrepancy  
 1249 in the combined distributions in Section 8.2.4.

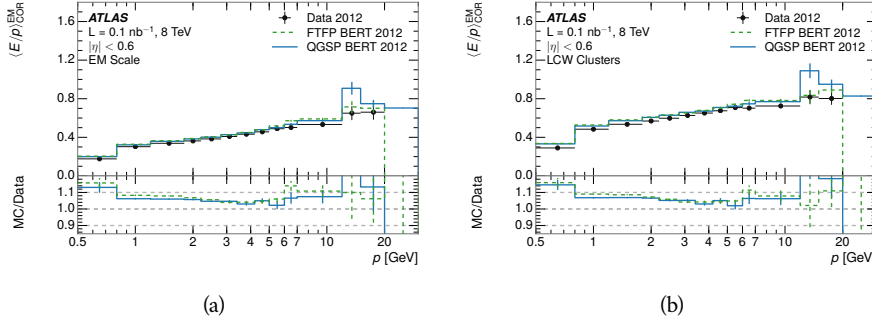


Figure 38: Comparison of the response of the EM calorimeter as a function of track momentum (a) at the EM-scale and (b) with the LCW calibration.

1250 **NOTE: There are more studies that I skipped for brevity that could be in-**  
 1251 **cluded if interesting.  $E/p$  at different cluster threshold settings,  $E/p$  with**  
 1252 **pileup,  $E/p$  with cells. I also left out a lot of eta bins that appear in the**  
 1253 **paper so that this section didn't turn into 20 pages of plots.**

### 1254 8.3 IDENTIFIED PARTICLE RESPONSE

1255 The inclusive response measurement for hadrons can be augmented by measur-  
 1256 ing the response for specific particle species. The simulation models each parti-  
 1257 cle type separately, and understanding the properties of each is important in con-  
 1258 straining the uncertainty on jets. In order to select and measure specific hadrons,  
 1259 this section relies on the displaced decays of long-lived particles. Such decays  
 1260 can be identified by reconstructing secondary vertices with a requirement on  
 1261 mass. In particular,  $\Lambda$ ,  $\bar{\Lambda}$ , and  $K_S^0$  can be used to select a pure sample of protons,  
 1262 antiprotons, and pions, respectively.

#### 1263 8.3.1 DECAY RECONSTRUCTION

1264 The measurement of response for identified particles uses the same selection as  
 1265 for inclusive particles (Section 8.1.3) with a few additions. Each event used is  
 1266 required to have at least one secondary vertex, and the tracks are required to  
 1267 match to that vertex rather than the primary vertex. Pions are selected from  
 1268 decays of  $K_S^0 \rightarrow \pi^+ \pi^-$ , which is the dominant decay for  $K_S^0$  to charged particles.  
 1269 Protons are selected from decays of  $\Lambda \rightarrow \pi^- p$  and antiprotons from  $\bar{\Lambda} \rightarrow \pi^+ \bar{p}$ ,  
 1270 which are similarly the dominant decays of  $\Lambda$  and  $\bar{\Lambda}$  to charged particles. The  
 1271 species of parent hadron in these decays is determined by reconstructing the  
 1272 mass of the tracks associated to the secondary vertex. The sign of the higher

momentum decay particle can distinguish between  $\Lambda$  and  $\bar{\Lambda}$ , which of course have the same mass, as the proton or antiproton is kinematically favored to have higher momentum. Examples of the reconstructed masses used to select these decays are shown in Figure 39.

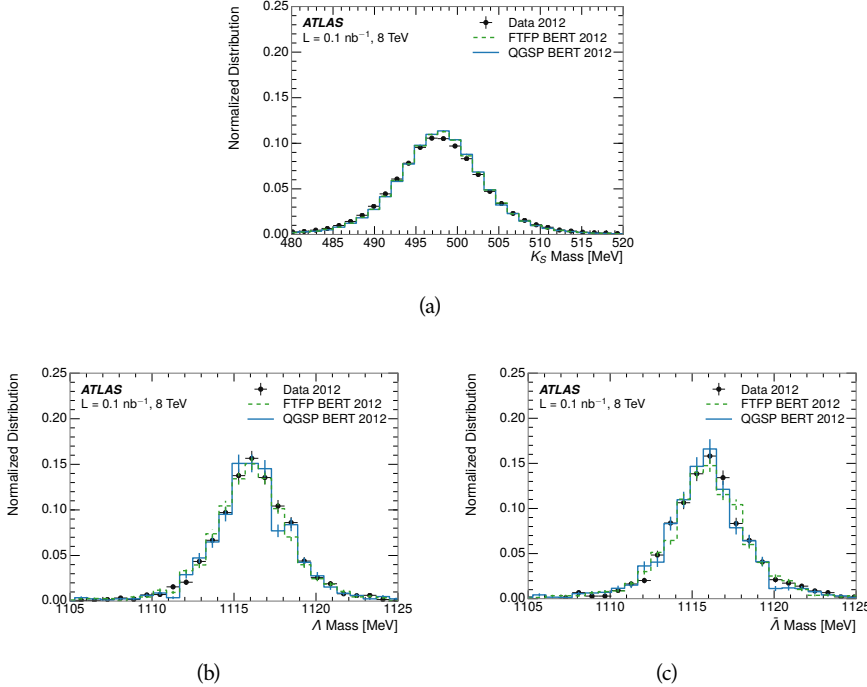


Figure 39: The reconstructed mass peaks of (a)  $K_S^0$ , (b)  $\Lambda$ , and (c)  $\bar{\Lambda}$  candidates.

The dominant backgrounds for the identified particle decays are nuclear interactions and combinatoric sources. These are suppressed by the kinematic requirements on the tracks as well as an additional veto which removes candidates that are consistent with both a  $\Lambda$  or  $\bar{\Lambda}$  and a  $K_S^0$  hypothesis, which is possible because of the different assumptions on particle mass in each case [12]. After these requirements, the backgrounds are found to be negligible compared to the statistical errors on these measurements.

### 8.3.2 IDENTIFIED RESPONSE

With these techniques the  $E/p$  distributions are extracted in data and simulation for each particle species and shown in Figure 40. These distributions are shown for a particular bin of  $E_a$  ( $2.2 < E_a/\text{GeV} < 2.8$ ), rather than  $p$ .  $E_a$  is the energy available to be deposited in the calorimeter: for pions  $E_a = \sqrt{p^2 + m^2}$ , for protons  $E_a = \sqrt{p^2 + m^2} - m$ , and for antiprotons  $E_a = \sqrt{p^2 + m^2} + m$ . The features of the  $E/p$  distributions are similar to the inclusive case. There is a small negative tail from noise and a large fraction of tracks with zero energy from particles which do not reach the calorimeter. The long positive tail is noticeably more pronounced for antiprotons because of the additional energy generated by the annihilation in addition to the neutral background.

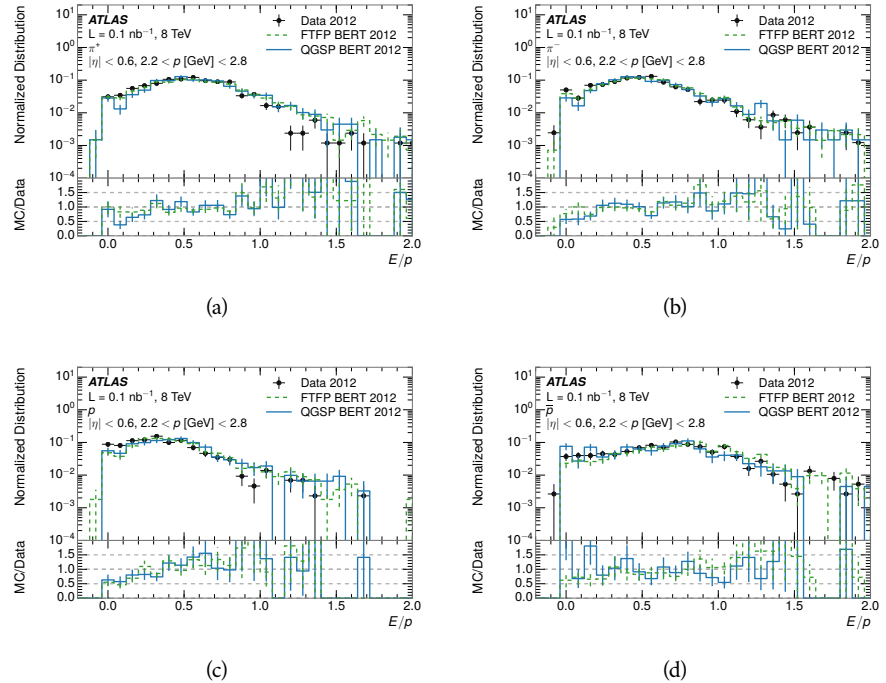


Figure 40: The  $E/p$  distribution for isolated (a)  $\pi^+$ , (b)  $\pi^-$ , (c) proton, and (d) anti-proton tracks.

1295      The zero fraction is further explored in Figure 41 for pions and protons in data  
 1296      and simulation. The simulation consistently underestimates the zero fraction  
 1297      independent of particle species, which implies that this discrepancy is not caused  
 1298      by the model of a particular species but rather a feature common to all.

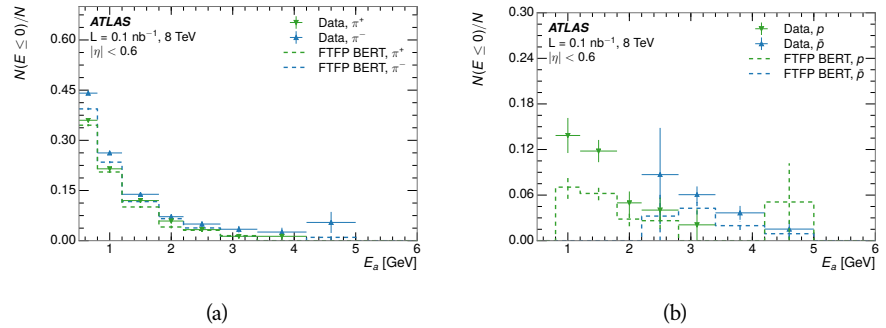


Figure 41: The fraction of tracks with  $E \leq 0$  for identified (a)  $\pi^+$  and  $\pi^-$ , and (b) proton and anti-proton tracks

1299      It is also interesting to compare the response between the different particle  
 1300      species. One approach to do this is to measure the difference in  $\langle E/p \rangle$  between  
 1301      two types, which has the advantage of removing the neutral background. These  
 1302      differences are shown in various combinations in Figure 42. The response for  
 1303       $\pi^+$  is greater on average than the response to  $\pi^-$  because of a charge-exchange  
 1304      effect which causes the production of additional neutral pions in the showers of

1305  $\pi^+$  [34]. The response for  $\pi^+$  is also greater on average than the response to  $p$ ,  
 1306 because a large fraction of the energy of  $\pi^+$  hadrons is converted to an electro-  
 1307 magnetic shower [35, 36]. However, the  $\bar{p}$  response is significantly higher than  
 1308 the response to  $\pi^-$  because of the annihilation of the antiproton. FTFP\_BERT  
 1309 does a better job of modeling this effect than QGSP\_BERT because of their differ-  
 1310 ent descriptions of  $\bar{p}$  interactions with material.

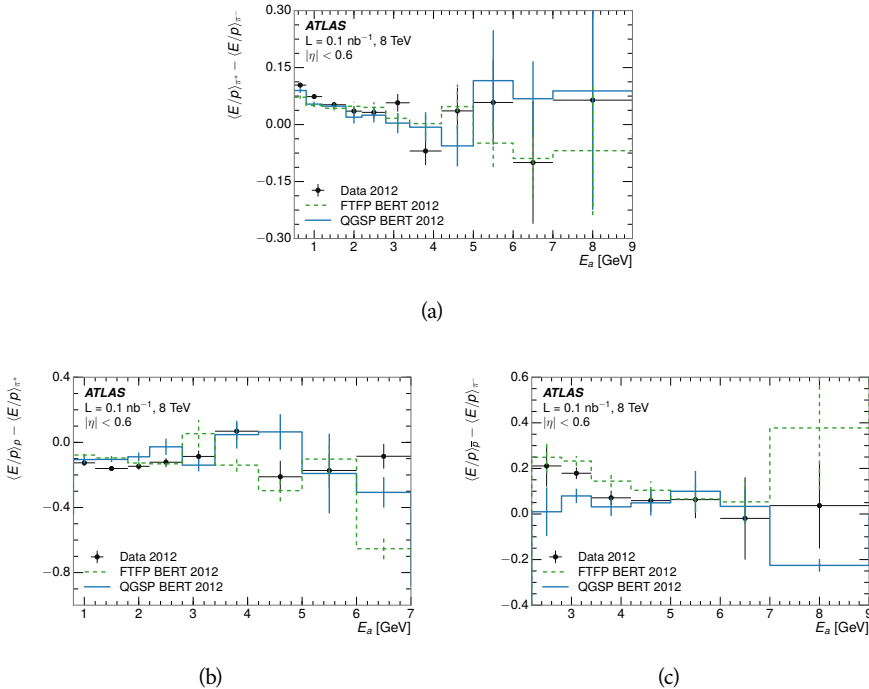


Figure 42: The difference in  $\langle E/p \rangle$  between (a)  $\pi^+$  and  $\pi^-$  (b)  $p$  and  $\pi^+$ , and (c)  $\bar{p}$  and  $\pi^-$ .

1311 It is also possible to remove the neutral background from these response dis-  
 1312 tributions using the same technique as in Section 8.2.3. The technique is largely  
 1313 independent of the particle species and so can be directly applied to  $\langle E/p \rangle$  for  
 1314 pions. The  $\langle E/p \rangle_{\text{COR}}$  distributions for pions are shown in Figure 43, which are  
 1315 very similar to the inclusive results. The inclusive hadrons are comprised mostly  
 1316 of pions, so this similarity is not surprising. It is also possible to see the small  
 1317 differences between  $\pi^+$  and  $\pi^-$  response here, where  $\langle E/p \rangle_{\text{COR}}$  is higher on av-  
 1318 erage for  $\pi^+$ . The agreement between data and simulation is significantly worse  
 1319 for the  $\pi^-$  distributions than for the  $\pi^+$ , with a discrepancy greater than 10%  
 1320 below 2-3 GeV.

### 1321 8.3.3 ADDITIONAL SPECIES IN SIMULATION

1322 The techniques above provide a method to measure the response separately for  
 1323 only pions and protons. However the hadrons which forms jets include a num-  
 1324 ber of additional species such as kaons and neutrons. The charged kaons are  
 1325 an important component of the inclusive charged hadron distribution, which is  
 1326 comprised of roughly 60-70% pions, 15-20% kaons, and 5-15% protons. These

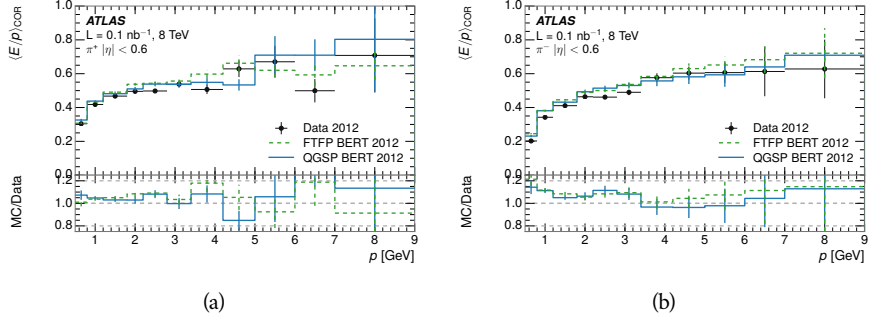


Figure 43:  $\langle E/p \rangle_{\text{COR}}$  as a function of track momentum for (a)  $\pi^+$  tracks and (b)  $\pi^-$  tracks.

are difficult to measure in data at the ATLAS detector, although a template subtraction technique has been proposed which may be effective with larger sample sizes [11]. The simulation of these particles includes noticeable differences in response at low energies, which are shown in Figure 44 for FTFP\_BERT. The significant differences in response between low energy protons and antiprotons are accounted for above in the definitions of  $E_a$ .

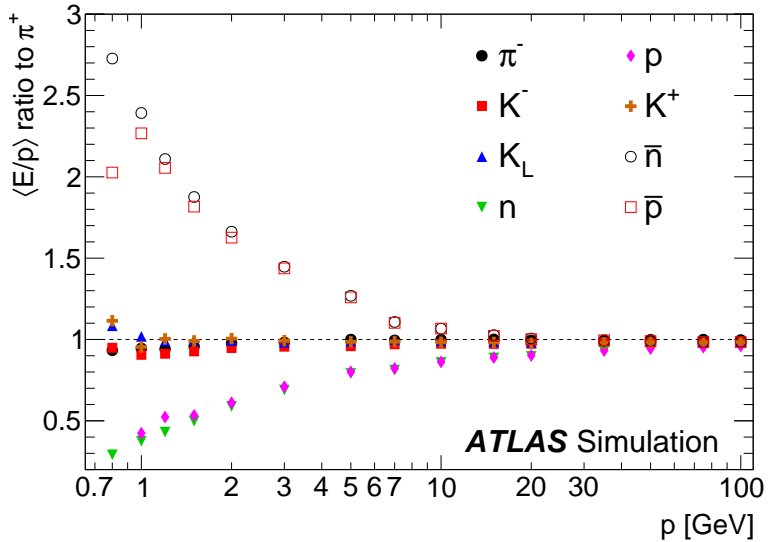


Figure 44: The ratio of the calorimeter response to single particles of various species to the calorimeter response to  $\pi^+$  with the physics list FTFP\_BERT.

1333 8.4 SUMMARY

1334 These various measurements of calorimeter response shown above for data and  
1335 simulation illuminate the accuracy of the simulation of hadronic interactions at  
1336 the ATLAS detector. The results were done using 2010 and 2012 data at 7 and 8  
1337 TeV, but reflect the most current understanding of the detector alignment and  
1338 geometry. A number of measurements focusing on a comparison between pro-

1339 tons and antiprotons suggest that FTFP\_BERT models those interaction more  
1340 accurately than QGSP\_BERT. These measurements, among others, were the moti-  
1341 vation to switch the default Geant4 simulation from FTFP\_BERT to QGSP\_BERT  
1342 for all ATLAS samples.

1343 Even with these updates, there are a number of small, approximately 5%, dis-  
1344 crepancies in response between the data and simulation at low energies. At  
1345 higher energies the simulation of hadronic interactions is very consistent with  
1346 data. Chapter 9 discusses how to use these observed differences to constrain the  
1347 jet energy scale and its associated uncertainties.



1348

## 1349 JET ENERGY RESPONSE AND UNCERTAINTY

## 1350 9.1 MOTIVATION

1351 As jets form a major component of many physics analyses at ATLAS, it is crucial  
 1352 to carefully calibrate the measurement of jet energies and to derive an uncer-  
 1353 tainty on that measurement. These uncertainties have often been the dominant  
 1354 systematic uncertainty in high-energy analyses at the LHC. Dijet and multijet  
 1355 balance techniques provide a method to constrain the JES and its uncertainty in  
 1356 data, and provide the default values used for ATLAS jet measurements at most  
 1357 energies [37]. These techniques are limited by their reliance on measuring jets  
 1358 in data, so they are statistically limited in estimating the jet energy scale at the  
 1359 highest jet energies. This chapter presents another method for estimating the jet  
 1360 energy scale and its uncertainty which builds up a jet from its components and  
 1361 thus can be naturally extended to high jet momentum. Throughout this chapter  
 1362 the jets studied are simulated using Pythia8 with the CT10 parton distribution  
 1363 set [38] and the AU2 tune [15], and corrections are taken from the studies includ-  
 1364 ing data and simulation in Chapter 8.

1365 As described in Section 7.2, jets are formed from topological clusters of energy  
 1366 in the calorimeters using the anti- $k_t$  algorithm. These clusters originate from a  
 1367 diverse spectrum of particles, in terms of both species and momentum, leading to  
 1368 significantly varied jet properties and response between jets of similar produced  
 1369 momentum. Figure 45 shows the simulated distribution of particles within jets  
 1370 at a few examples energies. The  $E/p$  measurements provide a thorough under-  
 1371 standing of the dominant particle content of jets, the charged hadrons.

## 1372 9.2 UNCERTAINTY ESTIMATE

1373 Simulated jets are not necessarily expected to correctly model the energy de-  
 1374 posits in the calorimeters, because of the various discrepancies discussed in Chap-  
 1375 ter 8. To evaluate a jet energy response, the simulated jet energies are compared  
 1376 to a corrected jet built up at the particle level. Each cluster in a jet is associated  
 1377 to the truth particle which deposited it, and the energy in that cluster is then  
 1378 corrected for a number of effects based on measurements in data. The primary  
 1379 corrections come from the single hadron response measurements in addition to  
 1380 response measured using the combined test beam which covers higher momen-  
 1381 tum particles [39]. These corrections include both a shift ( $\Delta$ ), in order to make  
 1382 the simulation match the average response in data, and an uncertainty ( $\sigma$ ) asso-  
 1383 ciated with the ability to constrain the difference between data and simulation.  
 1384 Some of the dominant sources of uncertainty are itemized in Table 3 with typi-  
 1385 cal values, and the full list considered is described in detail in the associated pa-

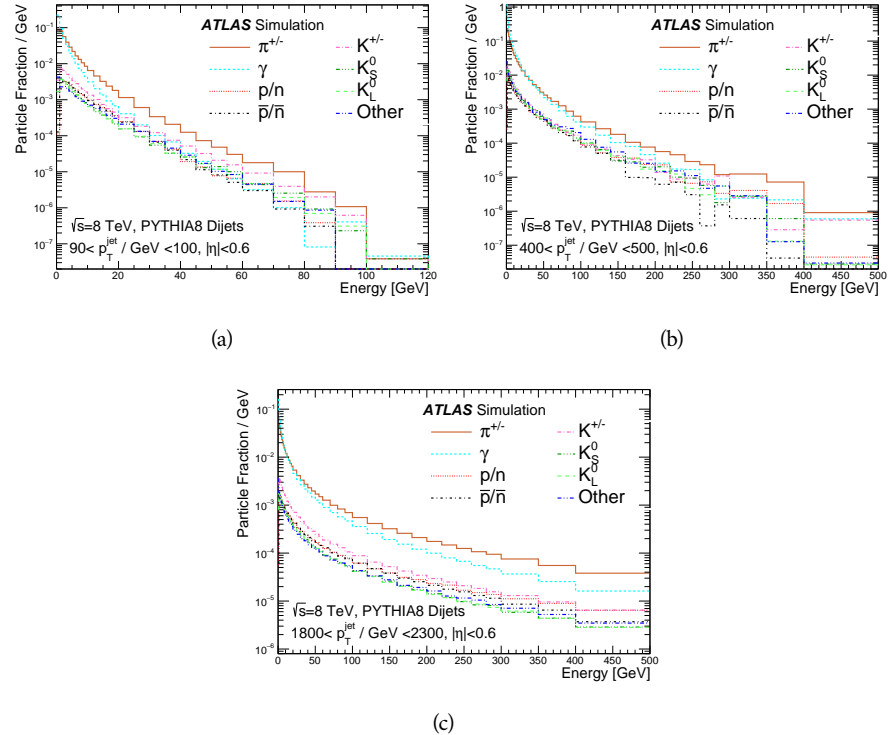


Figure 45: The spectra of true particles inside anti- $k_t$ ,  $R = 0.4$  jets with (a)  $90 < p_T/\text{GeV} < 100$ , (b)  $400 < p_T/\text{GeV} < 500$ , and (c)  $1800 < p_T/\text{GeV} < 2300$ .

1386 per [11]. These uncertainties cover differences between the data and simulation  
 1387 in the modeling of calorimeter response to a given particle. No uncertainties are  
 1388 added for the difference between particle composition of jets in data and simu-  
 1389 lation.

1390 From these terms, the jet energy scale and uncertainty is built up from indi-  
 1391 vidual energy deposits in simulation. Each uncertainty term is treated indepen-  
 1392 dently, and are taken to be gaussian distributed. The resulting scale and uncer-  
 1393 tainty is shown in Figure 46, where the mean response is measured relative to  
 1394 the calibrated energy reported by simulation. The dominant uncertainties come  
 1395 from the statistical uncertainties on the  $E/p$  measurements at lower energies and  
 1396 the additional uncertainty for out of range measurements at higher energies. The  
 1397 total uncertainty from this method at intermediate jet energies is comparable to  
 1398 other simulation-based methods [40] and is about twice as large as in-situ meth-  
 1399 ods using data [37]. This method is the only one which provides an estimation  
 1400 above 1.8 TeV, however, and so is still a crucial technique in analyses that search  
 1401 for very energetic jets.

1402 These techniques can also be used to measure the correlation between bins of  
 1403 average reconstructed jet momentum across a range of  $p_T$  and  $|\eta|$ , where cor-  
 1404 relations are expected because of a similarity in particle composition at similar  
 1405 energies. Figure 47 shows these correlations, where the uncertainties on jets in  
 1406 neighboring bins are typically between 30% and 60% correlated. The uncertainty  
 1407 on all jets becomes significantly correlated at high energies and larger pseudora-

Abbrev.	Description	$\Delta$ (%)	$\sigma$ (%)
In situ $E/p$	The comparison of $\langle E/p \rangle_{\text{COR}}$ as described in Chapter 8 with statistical uncertainties from 500 MeV to 20 GeV.	0-3	1-5
CTB	The main $\langle E/p \rangle$ comparison uncertainties, binned in $p$ and $ \eta $ , as derived from the combined test beam results, from 20 to 350 GeV [39].	0-3	1-5
$E/p$ Zero Fraction	The difference in the zero-fraction between data and MC simulation from 500 MeV to 20 GeV.	5-25	1-5
$E/p$ Threshold	The uncertainty in the EM calorimeter response from the potential mismodeling of threshold effects in topological clustering.	0	0-10
Neutral	The uncertainty in the calorimeter response to neutral hadrons based on studies of physics model variations.	0	5-10
$K_L$	An additional uncertainty in the response to neutral $K_L$ in the calorimeter based on studies of physics model variations.	0	20
$E/p$ Misalignment	The uncertainty in the $p$ measurement from misalignment of the ID.	0	1
Hadrons, $p > 350$ GeV	A flat uncertainty for all particles above the energy range or outside the longitudinal range probed with the combined test beam.	0	10

Table 3: The dominant sources of corrections and systematic uncertainties in the [JES](#) estimation technique, including typical values for the correcting shift ( $\Delta$ ) and the associated uncertainty ( $\sigma$ ).

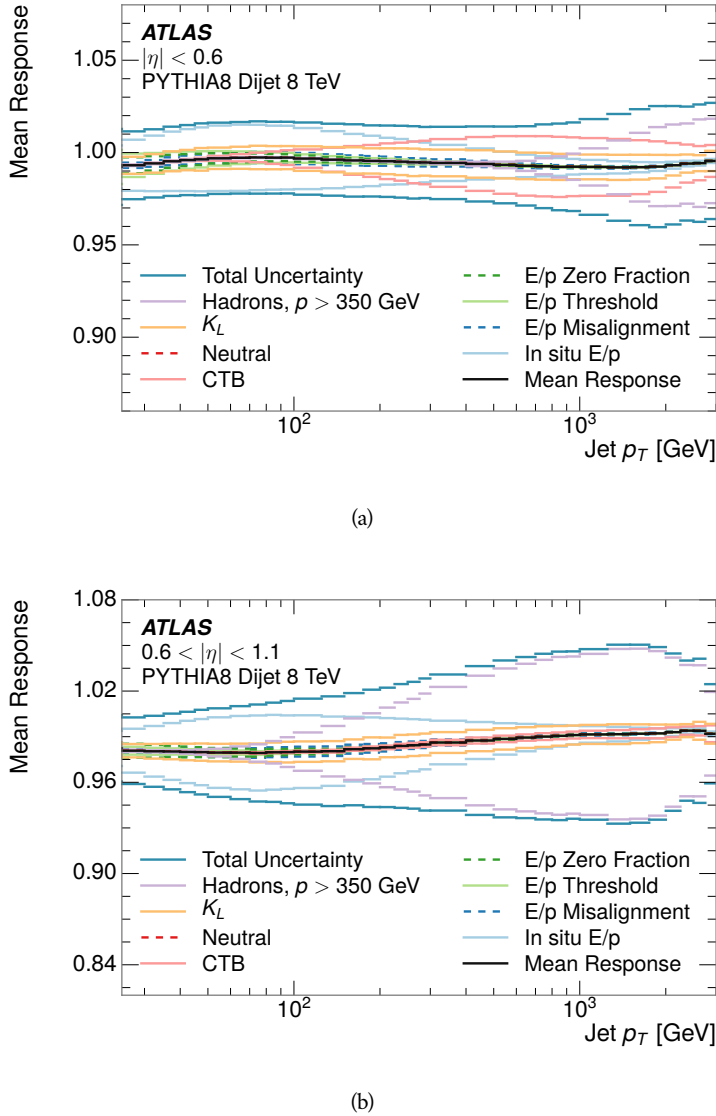


Figure 46: The [JES](#) uncertainty contributions, as well as the total [JES](#) uncertainty, as a function of jet  $p_T$  for (a)  $|\eta| < 0.6$  and (b)  $0.6 < |\eta| < 1.1$ .

1408      pidities, when the uncertainty becomes dominated by the single term reflecting  
 1409      out of range particles.

### 1410      9.3 SUMMARY

1411      The technique described above provides a jet energy scale and uncertainty by  
 1412      building up jet corrections from the energy deposits of constituent particles. The  
 1413       $E/p$  measurements are crucial in providing corrections for the majority of parti-  
 1414      cles in the jets. The uncertainty derived this way is between 2 and 5% and is about  
 1415      twice as large at corresponding momentum than jet balance methods. However  
 1416      this is the only uncertainty available for very energetic jets using 2012 data and  
 1417      simulation, and repeating this method with Run 2 data and simulation will be

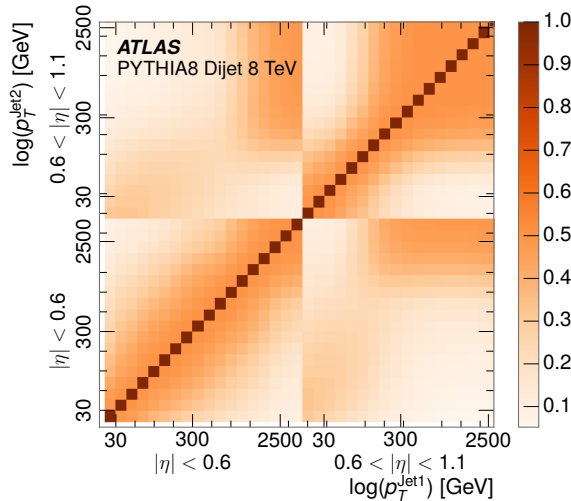


Figure 47: The **JES** correlations as a function of jet  $p_T$  and  $|\eta|$  for jets in the central region of the detector.

<sup>1418</sup> important in providing an uncertainty for the most energetic jets in 13 TeV col-  
<sup>1419</sup> lisions.



1420

## PART V

1421

### SEARCH FOR LONG-LIVED PARTICLES

1422

You can put some informational part preamble text here.



1423

1424 LONG-LIVED PARTICLES IN ATLAS

---

1425 As discussed in Section 2.3, various limitations in the SM suggest a need for new  
 1426 particles at the TeV scale. A wide range of extensions to the Standard Model  
 1427 predict that these new particles can have lifetimes greater than approximately  
 1428 one-hundredth of a nanosecond. These include theories with universal extra-  
 1429 dimensions [41, 42], with new fermions [43], and with leptoquarks [44]. Many  
 1430 SUSY theories also produce these Long-Lived Particles (LLPs), in both R-Parity  
 1431 violating [45–47] and R-Parity conserving [48–51] formulations. Split super-  
 1432 symmetry [52, 53], for example, predicts long-lived gluinos with O(TeV) masses.  
 1433 This search focuses specifically on the SUSY case, but many of the results are  
 1434 generic to any model with LLPs.

1435 Long-lived gluinos or squarks carry color-charge and will thus hadronize into  
 1436 color neutral bound states called R-Hadrons. These are composit particles like  
 1437 the usual hadrons but with one supersymmetric constituent, for example  $\tilde{g}q\bar{q}$   
 1438 and  $\tilde{q}\bar{q}$ . Through this hadronization process, the neutral gluino can acquire a  
 1439 charge. Gluino pair production,  $pp \rightarrow \tilde{g}\tilde{g}$  has the largest cross sectional increase  
 1440 with the increase in energy to 13 TeV, and so this search focuses on gluino R-  
 1441 Hadrons. Planned future updates will extend the case to explicitly include squark  
 1442 and chargino models, but the method covers any long-lived, charged, massive  
 1443 particle.

## 1444 10.1 EVENT TOPOLOGY

1445 The majority of SUSY models predict that gluinos will be produced in pairs at  
 1446 the LHC, through processes like  $pp \rightarrow q\bar{q} \rightarrow \tilde{g}\tilde{g}$  and  $pp \rightarrow gg \rightarrow \tilde{g}\tilde{g}$ , where the  
 1447 gluon mode dominates for the collision energy and gluino masses considered  
 1448 for this search. During their production, the long-lived gluinos hadronize into  
 1449 color singlet bound states including  $\tilde{g}q\bar{q}$ ,  $\tilde{g}qqq$ , and even  $\tilde{g}g$  [54]. The probability  
 1450 to form the gluon-only bound states is a free parameter usually taken to be 0.1,  
 1451 while the meson states are favored among the R-Hadrons [55]. The charged and  
 1452 neutral states are approximately equally likely for mesons, so the R-Hadrons will  
 1453 be charged roughly 50% of the time.

1454 These channels produce R-Hadrons with large  $p_T$ , comparable to their mass,  
 1455 so that they typically propagate with  $0.2 < \beta < 0.9$  [55]. The fragmentation that  
 1456 produces these hadrons is very hard, so the jet structure around the R-Hadron  
 1457 is minimal, with less than 5 GeV of summed particle momentum expected in a  
 1458 cone of  $\Delta R < 0.25$  around the R-Hadron [55]. After hadronization, depending  
 1459 on the gluino lifetime, the R-Hadrons then decay into hadrons and a LSP [54].

1460 In summary, the expected event for pair-produced long-lived gluinos is very  
 1461 simple: two isolated, high-momentum R-Hadrons that propagate through the  
 1462 detector before decaying into jets. The observable features of such events depend

1463 strongly on the interaction of the R-Hadron with the material of the detector and  
 1464 also its lifetime. Section 10.1.1 describes the interactions of R-Hadrons which  
 1465 reach the various detector elements in ATLAS and Section 10.1.2 provides a sum-  
 1466 mary of the observable event descriptions for R-Hadrons of various lifetimes.

1467 10.11 DETECTOR INTERACTIONS

1468 After approximately 0.2 ns, the R-Hadron reaches the pixel detector. If charged,  
 1469 it deposits energy into the material through repeated single collisions that result  
 1470 in ionization of the silicon substrate [7]. Because of its comparatively low  $\beta$ , the  
 1471 ionization energy can be significantly greater than expected for SM particles be-  
 1472 cause the most-probable energy loss grows significantly as  $\beta$  decreases [7]. This  
 1473 large ionization can be measured through the time over threshold (ToT) read out  
 1474 from the pixel detector as described in Section 7.1.1.2. Large ionization in the  
 1475 inner detector is one of the major characteristic features of LLPs.

1476 Throughout the next few nanoseconds, the R-Hadron propagates through the  
 1477 remainder of the inner detector. A charged R-Hadron will provide hits in each  
 1478 of these systems as would any other charged particle, and can be reconstructed  
 1479 as a track. The track reconstruction provides a measurement of its trajectory  
 1480 and thus its momentum as described in Section 7.1. The large momentum is  
 1481 another characteristic feature of massive particles produced at the LHC. **Note: At**  
**1482 this point I am failing to mention that the TRT provides a possible dE/dx**  
**1483 measurement, because no one uses it as far as I know.**

1484 As of roughly 20 ns, the R-Hadron enters the calorimeter where it interacts  
 1485 hadronically with the material. Because of its large mass and momentum, the  
 1486 R-Hadron does not typically stop in the calorimeter, but rather deposits a small  
 1487 fraction of its energy through repeated interactions with nucleons. The proba-  
 1488 bility of interaction between the gluino itself and a nucleon is low because the  
 1489 cross section drops off with the inverse square of its mass, so the interactions are  
 1490 primarily governed by the light constituents [56]. Each of these interactions can  
 1491 potentially change that quark content and thus change the sign of the R-Hadron,  
 1492 so that the charge at exit is typically uncorrelated with the charge at entry [55].  
 1493 The total energy deposited in the calorimeters during the propagation is small  
 1494 compared to the kinetic energy of the R-Hadron, around 20-40 GeV, so that  
 1495  $E/p$  is typically less than 0.1 [55].

1496 Then, 30 ns after the collision, it reaches the muon system, where it again  
 1497 ionizes in the material if charged and can be reconstructed as a muon track. Be-  
 1498 cause of the charge-flipping interactions in the calorimeter, this track may have  
 1499 the opposite sign of the track reconstructed in the inner detector, or there may  
 1500 be a track present when there was none in the inner detector and vice-versa. The  
 1501 propagation time at the typically lower  $\beta$  results in a significant delay compared  
 1502 to muons, and that delay can be assessed in terms of a time-of-flight measure-  
 1503 ment. Because of the probability of charge-flip and late arrival, there is a signif-  
 1504 icant chance that an R-Hadron which was produced with a charge will not be  
 1505 identified as a muon. The long time-of-flight is another characteristic feature of  
 1506 R-Hadrons which are reconstructed as muons.

## 1507 10.1.2 LIFETIME DEPENDENCE

1508 The above description assumed a lifetime long enough for the R-Hadron to exit  
 1509 the detector, which through this search is referred to as “stable”, even though  
 1510 the particle may decay after exiting the detector. There are several unique sig-  
 1511 natures at shorter lifetimes where the R-Hadron decays in various parts of the  
 1512 inner detector; these lifetimes are referred to as “metastable”.

1513 The shortest case where the R-Hadron is considered metastable is for life-  
 1514 times around 0.01 ns, where the particle decays before reaching any of the de-  
 1515 tector elements. Although the R-Hadrons are produced opposite each other in  
 1516 the transverse plane, each R-Hadron decays to a jet and an [LSP](#). The [LSPs](#) are not  
 1517 measured, so the produced jets can be significantly imbalanced in the transverse  
 1518 plane which results in large missing energy. That missing energy can be used  
 1519 to trigger candidate events, and provides the most efficient trigger option for  
 1520 shorter lifetimes. Additionally, the precision of the tracking system allows the  
 1521 displaced vertex of the R-Hadron decay to be reconstructed from the charged  
 1522 particles in the jet. The distance of that vertex from the interaction point can  
 1523 be used to distinguish R-Hadron decays from other processes. Figure 48 shows  
 1524 a schematic diagram of an example R-Hadron event with such a lifetime. The  
 1525 diagram is not to scale, but instead illustrates the detector interactions in the  
 1526 pixel detector, calorimeters, and muon system. It includes a representation of  
 1527 the charged R-Hadron and the neutral R-Hadron, as well as the [LSPs](#) and jets  
 1528 (shown as charged hadrons) produced in the decay. Neutral hadrons may also  
 1529 be produced in the decay but are not depicted. Previous searches on [ATLAS](#) have  
 1530 used the displaced vertex to target [LLP](#) decays [57].

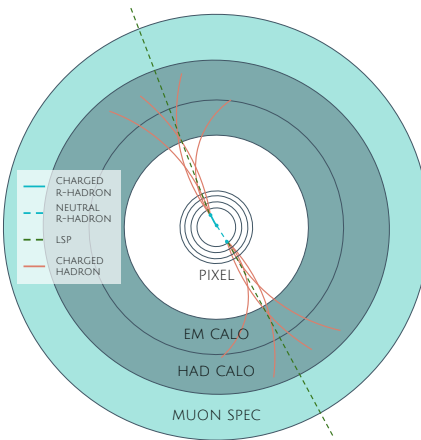


Figure 48: A schematic diagram of an R-Hadron event with a lifetime around 0.01 ns.  
 The diagram includes one charged R-Hadron (solid blue), one neutral R-Hadron (dashed blue), [LSPs](#) (dashed green) and charged hadrons (solid orange).  
 The pixel detector, calorimeters, and muon system are illustrated but not to scale.

1531 The next distinguishable case occurs at lifetimes greater than 0.1 ns, where  
 1532 the R-Hadron forms a partial track in the inner detector. If the decay products  
 1533 are sufficiently soft, they may not be reconstructed, and this forms a unique sig-

1534 nature of a disappearing track. An example of such an event is illustrated in  
 1535 Figure 49, which shows the short track in the inner detector and the undetected  
 1536 soft charged hadron and LSP that are produced. A dedicated search on ATLAS used  
 1537 the disappearing track signature to search for LLP in Run 1 [58]. **zNote: might**  
 1538 **not be worth mentioning the disappearing track here since it is actually a**  
 1539 **chargino search, the soft pion is pretty unique to charginos.**

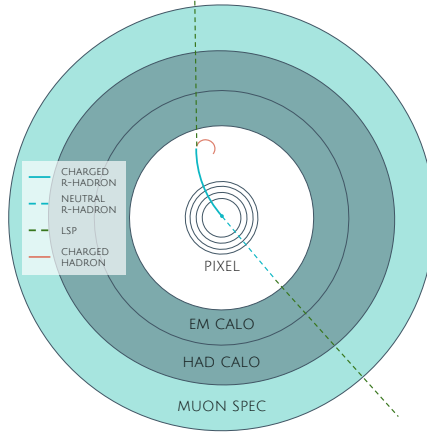


Figure 49: A schematic diagram of an R-Hadron event with a lifetime around 4 ns. The diagram includes one charged R-Hadron (solid blue), one neutral R-Hadron (dashed blue), LSPs (dashed green) and a charged hadron (solid orange). The pixel detector, calorimeters, and muon system are illustrated but not to scale.

1540 If the decay products are not soft, the R-Hadron daughters form jets, resulting  
 1541 in an event-level signature of up to two high-momentum tracks, jets, and signif-  
 1542 icant missing energy. The missing energy has the same origin as in the case of  
 1543 0.01 ns lifetimes, from the decay to unmeasured particles, and again can be large.  
 1544 The high-momentum tracks will also have the characteristically high-ionization  
 1545 of massive, long-lived particles in the inner detector. Figure 50 illustrates an ex-  
 1546 ample event with one charged R-Hadron which decays after approximately 10 ns,  
 1547 and shows how the jets from the decay can still be reconstructed in the calorime-  
 1548 ter. Several previous searches on ATLAS from Run 1 have used this signature to  
 1549 search for R-Hadrons [59, 60], including a dedicated search for metastable parti-  
 1550 cles [61].

1551 If the lifetime is longer than several nanoseconds, in the range of 15-30 ns,  
 1552 the R-Hadron decay can occur in or after the calorimeters, but prior to reaching  
 1553 the muon system. This case is similar to the above, although the jets may not be  
 1554 reconstructed, and is covered by many of the same search strategies. The events  
 1555 still often have large missing energy, although it is generated through different  
 1556 mechanisms. The R-Hadrons do not deposit much energy in the calorimeters, so  
 1557 a neutral R-Hadron will not enter into the missing energy calculation. A charged  
 1558 R-Hadron opposite a neutral R-Hadron will thus generate significant missing en-  
 1559 ergy, and close to 50% of pair-produced R-Hadron events fall into this category.  
 1560 If both R-Hadrons are neutral then the missing energy will be low because nei-  
 1561 ther is detected. Two charged R-Hadrons will also result in low missing energy  
 1562 because both are reconstructed as tracks and will balance each other in the trans-

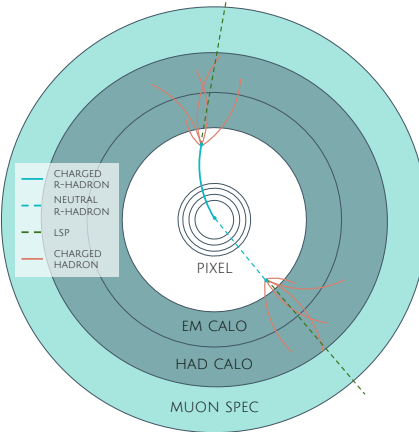


Figure 50: A schematic diagram of an R-Hadron event with a lifetime around 5 ns. The diagram includes one charged R-Hadron (solid blue), one neutral R-Hadron (dashed blue), LSPs (dashed green) and charged hadrons (solid orange). The pixel detector, calorimeters, and muon system are illustrated but not to scale.

1563 verse plane. A small fraction of the time, one of the charged R-Hadron tracks may  
 1564 fail quality requirements and thus be excluded from the missing energy calcula-  
 1565 tion and again result in significant missing energy. Figure 51 illustrates another  
 1566 example event with one charged R-Hadron which decays after approximately 20  
 1567 ns, and shows how the jets from the decay might not be reconstructed.

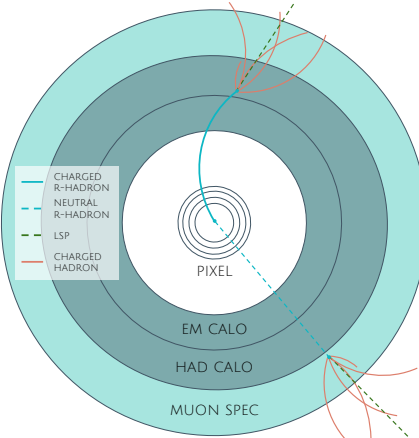


Figure 51: A schematic diagram of an R-Hadron event with a lifetime around 20 ns. The diagram includes one charged R-Hadron (solid blue), one neutral R-Hadron (dashed blue), LSPs (dashed green) and charged hadrons (solid orange). The pixel detector, calorimeters, and muon system are illustrated but not to scale.

1568 The longest lifetimes, the stable case, has all of the features of the 30-50 ns case  
 1569 but with the addition of muon tracks for any R-Hadrons that exit the calorimeter  
 1570 with a charge. That muon track can provide additional information from time-  
 1571 of-flight measurements to help identify LSPs. An example of the event topology  
 1572 for one charged and one neutral stable R-Hadron is shown in Figure 52. Some  
 1573 searches on ATLAS have included this information to improve the search reach  
 1574 for stable particles [60, 62].

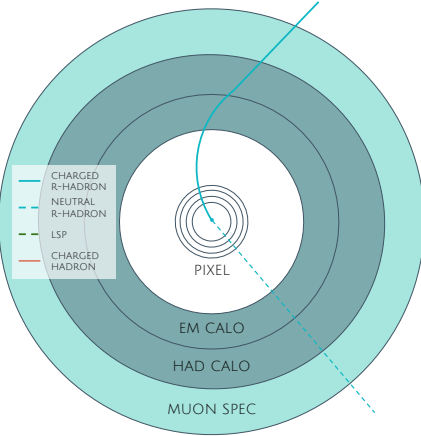


Figure 52: A schematic diagram of an R-Hadron event with a lifetime around 20 ns. The diagram includes one charged R-Hadron (solid blue) and one neutral R-Hadron (dashed blue). The pixel detector, calorimeters, and muon system are illustrated but not to scale.

## 1575 10.2 SIMULATION

1576 All of the event topologies discussed above are explored by simulations of R-  
 1577 Hadron events in the [ATLAS](#) detector. A large number of such samples are gen-  
 1578 erated to determine signal efficiencies, to measure expected yields, and to esti-  
 1579 mate uncertainties. The primary interaction, pair production of gluinos with  
 1580 masses between 400 and 3000 GeV, is simulated using [Pythia 6.4.27](#) [63]  
 1581 with the AUET2B [64] set of tuned parameters for the underlying event and  
 1582 the CTEQ6L1 [38] parton distribution function ([PDF](#)) set. The simulated inter-  
 1583 actions include a modeling of pileup by adding secondary, minimum bias in-  
 1584 teractions from both the same (in-time pileup) and nearby (out-of-time pileup)  
 1585 bunch crossings. This event generation is then augmented with a dedicated  
 1586 hadronization routine to hadronize the long-lived gluinos into final states with  
 1587 R-Hadrons [65], with the probability to form a gluon-gluino bound set at 10% [66].

1588 The cross sections used for these processes are calculated at next-to-leading  
 1589 order ([NLO](#)) in the strong coupling constant with a resummation of soft-gluon  
 1590 emmission at next-to-leading logarithmic ([NLL](#)) [67–71]. The nominal predic-  
 1591 tions and the uncertainties for each mass point are taken from an envelope of  
 1592 cross-section predictions using different [PDF](#) sets and factorization and renor-  
 1593 malization scales [72].

1594 The R-Hadrons then undergo a full detector simulation [], where the interac-  
 1595 tions of the R-Hadrons with the material of the detector are described by dedi-  
 1596 cated [Geant4](#) [8] routines. These routines model the interactions described in  
 1597 Section 10.1.1, including the ionizing interactions in the silicon modules of the  
 1598 inner detector and the R-Hadron-nucleon interactions in the calorimeters [73,  
 1599 74]. The specific routine chosen to describe the interactions of the R-Hadrons  
 1600 with nucleons, the “generic model”, uses a pragmatic approach where the scatter-  
 1601 ing cross section is taken to be a constant 12 mb per light quark. In this model

1602 the gluino itself does not interact at all except through its role as a reservoir of  
1603 kinetic energy.

1604 The lifetimes of these R-Hadrons are then simulated at several working points,  
1605  $\tau = 0.1, 1.0, 3.0, 10, 30, 50$  and detector stable, where the particle is required to  
1606 decay after propagating for a time compatible with its lifetime. Only one decay  
1607 mode is simulated for these samples,  $\tilde{g} \rightarrow q\bar{q}\tilde{\chi}_1^0$  with the neutralino mass set to  
1608 100 GeV, which is chosen because it has the highest sensitivity among all of the  
1609 modes studied in previous searches [61]. Heavier neutralinos have similar results  
1610 but generate less missing energy which reduces the efficiency of triggering.

1611 All of the simulated events are then reconstructed using the same software  
1612 used for collision data. The fully reconstructed events are then reweighted to  
1613 match the distribution of initial state radiation in an alternative sample of events,  
1614 generated with MG5\_aMC@NLO [75], which has a more accurate description of ra-  
1615 diate effects than Pythia6. This reweighting provides a more accurate descrip-  
1616 tion of the momentum of the gluino-gluino system and is important in modeling  
1617 the efficiency of triggering and offline event selection.



1618

1619 EVENT SELECTION

---

1620 The [LLPs](#) targeted by this search differ in their interactions with the detector from  
 1621 [SM](#) particles primarily because of their large mass. When produced at the ener-  
 1622 gies available at the [LHC](#), that large mass results in a low  $\beta$  (typically  $0.2 < \beta <$   
 1623 0.9). Such slow-moving particles heavily ionize in detector material. Each layer  
 1624 of the pixel detector provides a measurement of that ionization, through [ToT](#), as  
 1625 discussed in Section 6.3.1. The ionization in the pixel detector, quantified in  
 1626 terms of  $dE/dx$ , provides the major focus for this search technique, along with  
 1627 the momentum measured in the entire inner detector. It is effective both for its  
 1628 discriminating power and its use in reconstructing a particle's mass, and it can  
 1629 be used for a wide range of masses and lifetimes as discussed in Section 10.1.2.  
 1630 However  $dE/dx$  needs to be augmented with a few additional selection require-  
 1631 ments to provide a mechanism for triggering and to further reduce backgrounds.

1632 Ionization itself is not currently accessible for triggering, so this search in-  
 1633 stead relies on  $E_T^{\text{miss}}$  to trigger signal events. Although triggering on  $E_T^{\text{miss}}$  can  
 1634 be inefficient,  $E_T^{\text{miss}}$  is often large for many production mechanisms of [LLPs](#), as  
 1635 discussed in Section 10.1.

1636 The use of ionization to reject [SM](#) backgrounds relies on well-measured, high-  
 1637 momentum tracks, so some basic requirements on quality and kinematics are  
 1638 placed on the tracks considered in this search. These quality requirements have  
 1639 been significantly enhanced in Run 2 by a newly introduced tracking variable  
 1640 that is very effective in removing highly-ionizing backgrounds caused by over-  
 1641 lapping tracks. A few additional requirements are placed on the tracks consid-  
 1642 ered for [LLP](#) candidates that increase background rejection by targeting specific  
 1643 types of [SM](#) particles. These techniques provide a significant analysis improve-  
 1644 ment over previous iterations of ionization-based searches on ATLAS by provid-  
 1645 ing additional background rejection with minimal loss in signal efficiency.

1646 The ionization measurement with the Pixel detector can be calibrated to pro-  
 1647 vide an estimator of  $\beta\gamma$ . That estimate, together with the momentum measure-  
 1648 ment provided by tracking, can be used to reconstruct a mass for each track  
 1649 which traverses the pixel detector. That mass variable will be peaked at the [LLP](#)  
 1650 mass for any signal, and provides an additional tool to search for an excess. In  
 1651 addition to an explicit requirement on ionization, this search constructs a mass-  
 1652 window for each targeted signal mass in order to evaluate any excess of events  
 1653 and to set limits.

1654 The strategy discussed here is optimized for lifetimes of  $O(1) - O(10)$  ns.  
 1655 Pixel ionization is especially useful in this regime as particles only need to prop-  
 1656 agate through the first seven layers of the inner detector, about 37 cm from the  
 1657 beam axis. The search is still competitive with other searches for [LLPs](#) at longer  
 1658 lifetimes, because the primary discriminating variables are still applicable even  
 1659 for particles that do not decay within the detector [62]. Although the majority of

1660 the requirements will be the same for all lifetimes, two signal regions are defined  
 1661 to optimize separately for intermediate and long lifetime particles.

## 1662 11.1 TRIGGER

1663 Triggering remains a significant difficulty in defining an event selection with  
 1664 high signal efficiency in a search for LLPs. There are no triggers available in  
 1665 the current ATLAS system that can fire directly from a high momentum track  
 1666 with large ionization (Section 6.6). Although in some configurations a charged  
 1667 LLP can fire muon triggers, this requirement introduces significant model depen-  
 1668 dence on both the allowed lifetimes and the interactions in the calorimeter [55],  
 1669 as discussed in Section 10.1.1.

1670 For a search targeting particles which may decay prior to reaching the muon  
 1671 system, the most efficient available trigger is based on missing energy [55]. As  
 1672 discussed in Section 10.1, signal events can produce significant  $E_T^{\text{miss}}$  by a few  
 1673 mechanisms. At the trigger level however, the missing energy is only calculated  
 1674 using the calorimeters (Section 6.6) where the R-Hadrons deposit little energy.  
 1675 So, at short lifetimes,  $E_T^{\text{miss}}$  measured in the calorimeter is generated by an im-  
 1676 balance between the jets and undetected LSPs produced in R-Hadron decays. At  
 1677 longer lifetimes, without the decay products, missing energy is only produced in  
 1678 the calorimeters when the R-Hadrons recoil against an initial state radiation (ISR)  
 1679 jet.

1680 These features are highlighted in Figure 53, which shows the  $E_T^{\text{miss}}$  distribu-  
 1681 tions for simulated short lifetime (3 ns) and stable R-Hadron events. The figure  
 1682 includes both the offline  $E_T^{\text{miss}}$ , the missing energy calculated with all available  
 1683 information, and Calorimeter  $E_T^{\text{miss}}$ , the missing energy calculated using only  
 1684 information available at the calorimeter which approximates the missing energy  
 1685 available at the trigger. The short lifetime sample has significantly greater  $E_T^{\text{miss}}$   
 1686 and Calorimeter  $E_T^{\text{miss}}$  than the stable sample as expected. For the stable sam-  
 1687 ple, a small fraction of events with very large  $E_T^{\text{miss}}$  (about 5%) migrate into the  
 1688 bin with very small Calorimeter  $E_T^{\text{miss}}$  because the  $E_T^{\text{miss}}$  produced by a charged  
 1689 R-Hadron track opposite a neutral R-Hadron track does not contribute any miss-  
 1690 ing energy in the calorimeters.

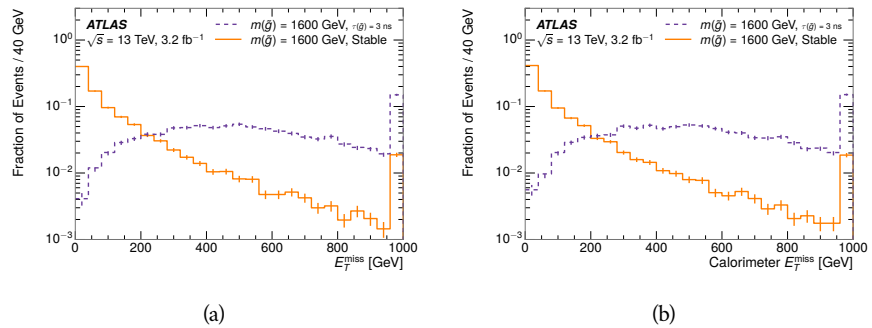


Figure 53: The distribution of (a)  $E_T^{\text{miss}}$  and (b) Calorimeter  $E_T^{\text{miss}}$  for simulated signal events before the trigger requirement.

1691 So, either case to some extent relies on kinematic degrees of freedom to pro-  
 1692 duce missing energy, as the pair-produced LLPs tend to balance each other in  
 1693 the transverse plain. That balance results in a relatively low efficiency for long-  
 1694 lifetime particles, roughly 40%, and efficiencies between 65% and 95% for shorter  
 1695 lifetimes depending on both the mass and the lifetime. For long lifetimes in par-  
 1696 ticular, the presence of ISR is important in providing an imbalance in the trans-  
 1697 verse plane, and is an important aspect of modeling the selection efficiency for  
 1698 R-Hadron events.

1699 The missing energy trigger with the lowest threshold available is chosen for  
 1700 this selection in order to maximize the trigger efficiency. During 2015 data col-  
 1701 lection this was the HLT\_xe70 trigger, which used a 50 GeV threshold on miss-  
 1702 ing energy at LVL1 and a 70 GeV threshold on missing energy at the HLT. These  
 1703 formation of the trigger decision for missing energy was discussed in more detail  
 1704 in Section 6.6.

## 1705 11.2 KINEMATICS AND ISOLATION

1706 After the trigger requirement, each event is required to have a primary vertex  
 1707 reconstructed from at least two well-measured tracks in the inner detector, each  
 1708 with  $p_T > 400$  MeV. If more than one such vertex exists, the primary vertex  
 1709 is taken to be the one with the largest summed track momentum for all tracks  
 1710 associated to that vertex. The offline reconstructed  $E_T^{\text{miss}}$  is required to be above  
 1711 130 GeV to additionally reject SM backgrounds. The transverse missing energy  
 1712 is calculated using fully reconstructed and calibrated offline objects, as described  
 1713 in Section 7.5. In particular the  $E_T^{\text{miss}}$  definition in this selection uses jets recon-  
 1714 structed with the anti- $k_t$  algorithm with radius  $R = 0.4$  from clusters of energy  
 1715 in the calorimeter (Section 7.2) and with  $p_T > 20$  GeV, as well as reconstructed  
 1716 muons, electrons, and tracks not identified as another object type.

1717 The  $E_T^{\text{miss}}$  distributions are shown for data and a few simulated signals in Fig-  
 1718 ure 54, after the trigger requirement. The cut placed at 130 GeV is 95% effi-  
 1719 cient for metastable and 90% efficient for stable particles, after the trigger re-  
 1720 quirement, because of the missing energy generating mechanisms discussed pre-  
 1721 viously. The distribution of data in this figure and subsequent figures in this sec-  
 1722 tion can be interpreted as the distribution of backgrounds, as any signal contam-  
 1723 ination would be negligible if present at these early stages of the selection (prior  
 1724 to the final requirement on ionization). The background falls rapidly with miss-  
 1725 ing energy, motivating the direct requirement on  $E_T^{\text{miss}}$  for the signal region. Al-  
 1726 though a tighter requirement than the specified value of 130 GeV would seem to  
 1727 increase the search potential from these early distributions, other requirements  
 1728 are more optimal when taken as a whole. The specific values for each require-  
 1729 ment in signal region were optimized considering the increase in discovery reach  
 1730 for tightening the requirement on each discriminating variable. **NOTE: If space**  
 1731 **and time permit, I will add a whole section about signal region optimiza-**  
 1732 **tion..**

1733 It is typically the practice for searches for new physics on ATLAS to place an  
 1734 offline requirement on the triggering variable that is sufficiently tight to guar-

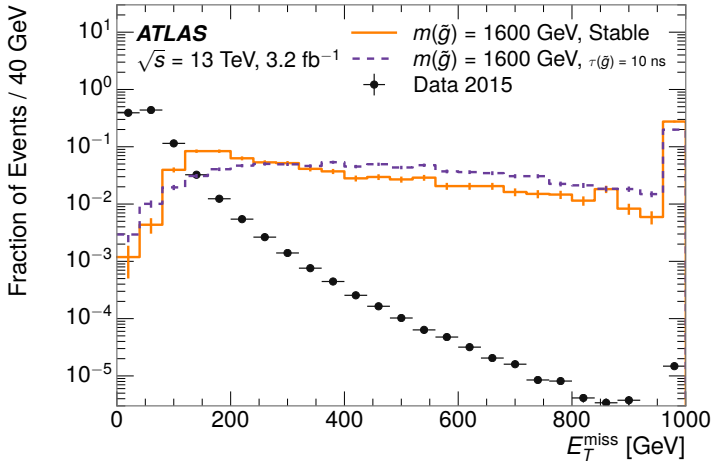


Figure 54: The distribution of  $E_T^{\text{miss}}$  for data and simulated signal events, after the trigger requirement.

1735 antee that the event would pass the trigger. Such a tight requirement makes the  
 1736 uncertainty on the trigger efficiency of the simulation negligible, as modeling the  
 1737 regime where the trigger is only partially efficient can be difficult. In this analy-  
 1738 sis, however, because of the atypical interactions of R-Hadrons with the tracker  
 1739 and the calorimeter, the offline requirement on  $E_T^{\text{miss}}$  is not sufficient to guar-  
 1740 antee a 100% trigger efficiency even at large values, as can be seen in Figure 55.  
 1741 This figure shows the efficiency for passing the HLT\_xe70 trigger as a function  
 1742 of the requirement on  $E_T^{\text{miss}}$ , which plateaus to roughly 85% even at large values.  
 1743 This plateau does not reach 100% because events which have large offline miss-  
 1744 ing energy from a neutral R-Hadron produced opposite of a charged R-Hadron  
 1745 can have low missing energy in the calorimeters. The Calorimeter  $E_T^{\text{miss}}$ , on the  
 1746 other hand, does not have this effect and reaches 100% efficiency at large values  
 1747 because it is the quantity that directly corresponds to the trigger threshold. In  
 1748 both cases the efficiency of triggering is greater for the short lifetime sample be-  
 1749 cause the late decays to hadrons and LSPs produce an imbalance in the calorime-  
 1750 ters even though they may not be reconstructed offline as tracks or jets. For this  
 1751 reason, the requirement on  $E_T^{\text{miss}}$  is determined by optimizing the background  
 1752 rejection even though it corresponds to a value of trigger efficiency significantly  
 1753 below 1.0.

1754 Potential signal events are then required to have at least one candidate LLP  
 1755 track. Although the LLPs are produced in pairs, many models do not consistently  
 1756 yield two charged particles. For example, in the R-Hadron model highlighted  
 1757 here, only 20% of events have two charged R-Hadrons while 47% of events have  
 1758 just one. A signal region requiring two charged candidates could be a powerful  
 1759 improvement in background rejection for a larger dataset, but it is not consid-  
 1760 ered in this version of the analysis as it was found to be unnecessary to reject the  
 1761 majority of backgrounds.

1762 For a track to be selected as a candidate, it must have  $p_T > 50 \text{ GeV}$  and pass  
 1763 basic quality requirements. The track must be associated to the primary vertex.

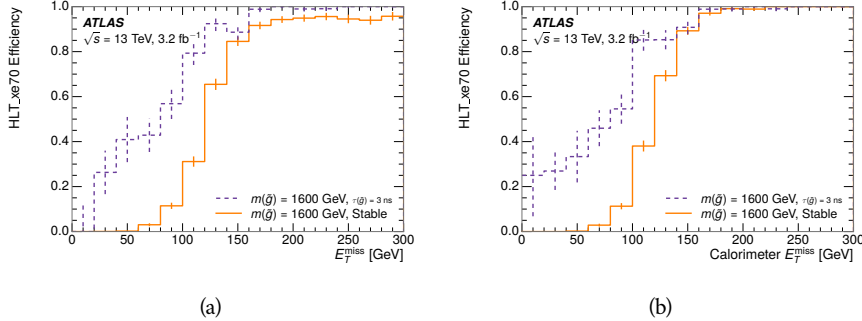


Figure 55: The trigger efficiency for the HLT\_xe70 trigger requirement as a function of (a)  $E_T^{\text{miss}}$  and (b) Calorimeter  $E_T^{\text{miss}}$  for simulated signal events.

1764 It must also have at least seven clusters in the silicon layers in the inner detector  
 1765 to ensure an accurate measurement of momentum. Those clusters must include  
 1766 one in the innermost layer if the extrapolated track is expected to pass through  
 1767 that layer. And to ensure a reliable measurement of ionization, the track is re-  
 1768 quired to have at least two clusters in the pixel detector that provide a measure-  
 1769 ment of  $dE/dx$ .

1770 At this point in the selection, there is a significant high-ionization background  
 1771 from multiple tracks that significantly overlap in the inner detector. Previous  
 1772 version of this analysis have rejected these overlaps by an explicit overlap rejec-  
 1773 tion between pairs of fully reconstructed tracks, typically by requiring no addi-  
 1774 tional tracks within a cone around the candidate. This technique, however, fails  
 1775 to remove the background from tracks that overlap so precisely that the tracks  
 1776 cannot be separately resolved, which can be produced in very collimated photon  
 1777 conversions or decays of pions.

1778 A new method, added in Run 2, identifies cluster shapes that are likely formed  
 1779 by multiple particles based on a neural network classification algorithm. The  
 1780 number of clusters that are classified this way in the pixel detector for a given  
 1781 track is called  $N_{\text{split}}$ . As the shape of clusters requires significantly less spatial  
 1782 separation to identify overlaps than it does to reconstruct two fully resolved  
 1783 tracks, this variable is more effective at rejecting backgrounds from overlaps.  
 1784 Figure 56 shows the dependence of ionization on  $N_{\text{split}}$ ; as  $N_{\text{split}}$  increases the  
 1785 most probable value of  $dE/dx$  grows significantly up to twice the expected value  
 1786 when  $N_{\text{split}} = 4$ .

1787 This requirement is very successful in reducing the long positive tail of the  
 1788  $dE/dx$  distributions, as can be seen in Figure 57. Comparing the distribution  
 1789 for “baseline tracks”, tracks with only the above requirements on clusters ap-  
 1790 plied and before the requirement on  $N_{\text{split}}$ , to the distribution with  $N_{\text{split}} = 0$ ,  
 1791 it is clear that the fraction of tracks with large  $dE/dx$  is reduced be several or-  
 1792 ders of magnitude. The tracks without split hits are very close to the  $dE/dx$   
 1793 distribution of identified muons, which are extremely well isolated on average.  
 1794 Figure 57 also includes the distribution of  $dE/dx$  in an example signal simula-  
 1795 tion to demonstrate how effective  $dE/dx$  is as a discriminating variable with this  
 1796 isolation applied. The background falls rapidly for  $dE/dx > 1.8 \text{ MeVg}^{-1}\text{cm}^2$

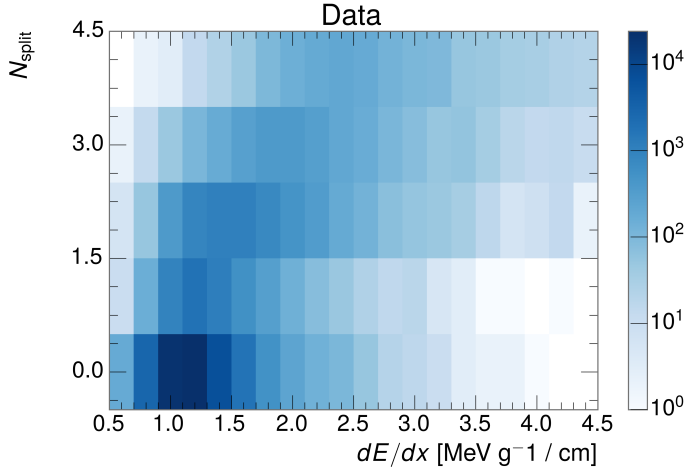


Figure 56: The dependence of  $dE/dx$  on  $N_{\text{split}}$  in data after basic track hit requirements have been applied.

1797 while the majority of the signal, approximately 90% depending on the mass, falls  
 1798 above that threshold. Over 90% of LLP tracks in simulated signal events pass the  
 1799  $N_{\text{split}}$ -based isolation requirement.

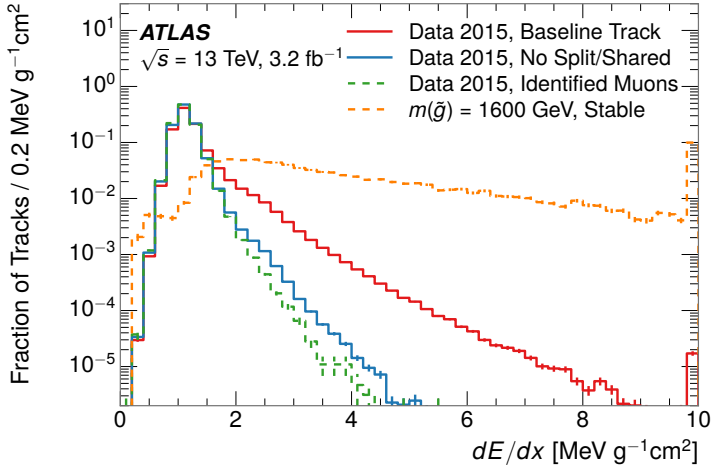


Figure 57: The distribution of  $dE/dx$  with various selections applied in data and simulated signal events.

1800 A few additional kinematic requirements are imposed to help reduce SM back-  
 1801 grounds. The momentum of the candidate track must be at least 150 GeV, and  
 1802 the uncertainty on that measurement must be less than 50%. The distribution of  
 1803 momentum is shown in Figure 58 for tracks in data and simulated signal events  
 1804 after the previously discussed requirements on clusters, transverse momentum,  
 1805 and isolation have been imposed. The signal particles are much harder on aver-

1806 age than their backgrounds because of the high energy interactions required to  
 1807 produce them. The transverse mass,  $M_T$ , defined as

$$M_T = \sqrt{2p_T E_T^{\text{miss}}(1 - \cos(\Delta\phi(E_T^{\text{miss}}, \text{track})))} \quad (6)$$

1808 estimates the mass of a decay of to a single charged particle and an undetected  
 1809 particle and is required to be greater than 130 GeV to reject contributions from  
 1810 the decay of W bosons. Figure 59 shows the distribution of  $M_T$  for data and  
 1811 simulated signal events. The signal is distributed over a wide range of  $M_T$ , with  
 1812 about 90% above the threshold value of 130 GeV. The data shows a dual-peaked  
 1813 structure, where the first peak comes from W boson decays and the second peak  
 1814 is a kinematic shaping from the requirements on  $E_T^{\text{miss}}$  and the track  $p_T$  in dijet  
 1815 events.

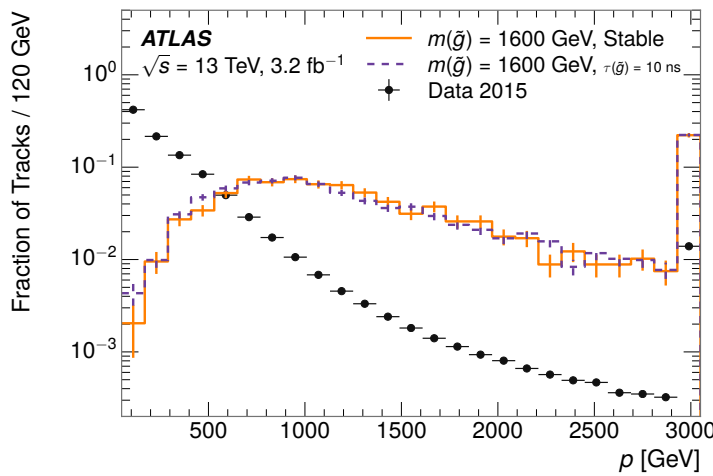


Figure 58: The distribution of track momentum for data and simulated signal events, after previous selection requirements have been applied.

### 1816 11.3 PARTICLE SPECIES REJECTION

1817 The amount of ionization deposited by particles with low mass and high mo-  
 1818 mentum has a large positive tail [7], so backgrounds can be formed by a wide  
 1819 variety of SM processes when various charged particles have a few randomly  
 1820 large deposits of energy in the pixel detector. Those backgrounds can be ad-  
 1821 ditionally reduced by targeting other interactions with the detector where they  
 1822 are expected to have different behavior than R-Hadrons. The interactions with  
 1823 the detector depend on the types of particles produced rather than the processes  
 1824 which produce them, so this search forms a series of rejections to remove back-  
 1825 grounds from individual particle species. These rejections focus on using addi-  
 1826 tional features of the event, other than the kinematics of the candidate track, as  
 1827 they can provide a powerful source of background rejection with very high sig-  
 1828 nal efficiency. However, the lifetime of an R-Hadron can significantly change its

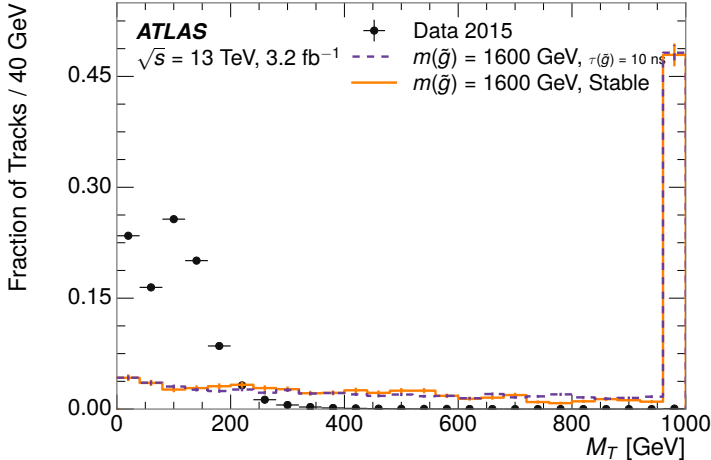


Figure 59: The distribution of  $M_T$  for data and simulated signal events, after previous selection requirements have been applied.

1829 detector characteristics, as discussed in Section 10.1.2. To accommodate these  
 1830 differences, the SM rejections defined in this section are split to form two signal  
 1831 regions, one for long-lifetimes particles, the stable region ( $50 \leq \tau[\text{ns}] < \infty \text{ ns}$ ),  
 1832 and one for intermediate lifetime particles, the metastable region ( $0.4 < \tau[\text{ns}] <$   
 1833 50).

1834 Jets can be very effectively rejected by considering the larger-scale isolation of  
 1835 the candidate track. In this case the isolation focuses on the production of nearby  
 1836 particles as a jet-veto, rather than the isolation from overlapping tracks based on  
 1837  $N_{\text{split}}$  that was used to reduce high-ionization backgrounds. As explained in Sec-  
 1838 tion 10.1, the fragmentation process which produces an R-Hadron is very hard  
 1839 and thus is not expected to produce additional particles with a summed momen-  
 1840 tum of more than 5 GeV. The jet-veto uses the summed momentum of tracks  
 1841 with a cone of  $\Delta R < 0.25$ , referred to as  $p_T^{\text{Cone}}$ , which is shown in Figure 60 for  
 1842 data and simulated signal events. In the data this value has a peak at zero from  
 1843 isolated tracks such as leptons, and a long tail from jets which contains as much  
 1844 as 80% of the background above 20 GeV at this stage of the selection. In signal  
 1845 events  $p_T^{\text{Cone}}$  is strongly peaked at zero and significantly less than 1% of signal  
 1846 events have  $p_T^{\text{Cone}}$  above 20 GeV. This makes a requirement of  $p_T^{\text{Cone}} < 20 \text{ GeV}$   
 1847 a very effective method to reject background without losing signal efficiency.  
 1848 For the stable signal region, this cut is further tightened to  $p_T^{\text{Cone}} < 5 \text{ GeV}$  as  
 1849 it is the most effective variable remaining to extend the search reach for long  
 1850 lifetimes.

1851 Even for fully isolated particles, there are additional methods to reject each  
 1852 type of particle using information in the muon system and calorimeters. Muons  
 1853 can be identified very reliably using the tracks in the muon system, as described  
 1854 in Section 7.4. For intermediate lifetimes the LLPs do not survive long enough  
 1855 to reach the muon system, and so muons are vetoed by rejecting tracks that as-  
 1856 sociate to a muon with medium muon identification requirements (Section 7.4).  
 1857 For longer lifetimes, this rejection is not applied because LLPs which reach the

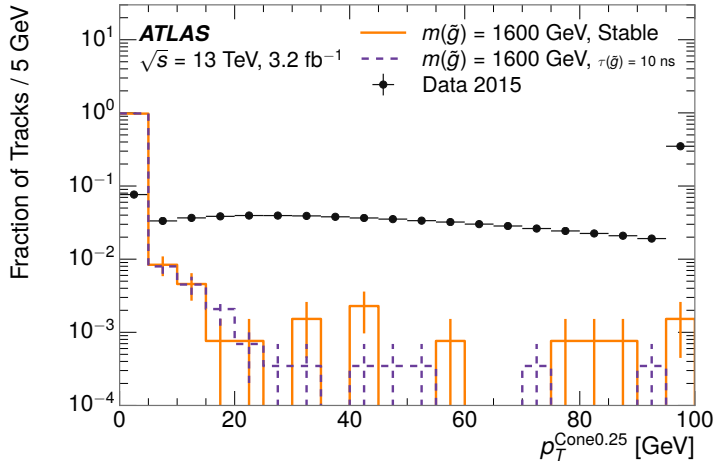


Figure 60: The distribution of summed tracked momentum within a cone of  $\Delta R < 0.25$  around the candidate track for data and simulated signal events, after previous selection requirements have been applied.

muon system can be identified as muons as often as 30% of the time in simulated samples.

Calorimeter-based particle rejection relies on the expected small deposits of energy from LLPs. When the lifetime is long enough to reach the calorimeter, a LLP deposits little of its energy as it traverses the material, as discussed in Section 10.1. Even when the particle does decay before the calorimeter, the majority of its energy is carried away by the LSP and not deposited in the calorimeter. In both cases the energy is expected to be distributed across the layers of the calorimeters and not peaked in just one layer. This can be quantified in terms of  $E/p$ , the ratio of calorimeter energy of a nearby jet to the track momentum, and  $f_{\text{EM}}$ , the fraction of energy in that jet within the electromagnetic calorimeter. When no jets fall within a cone of 0.05 of the particle,  $E/p$  and  $f_{\text{EM}}$  are both defined as zero.  $E/p$  is expected to be above 1.0 for typical SM particles because of calibration and the contributions from other nearby particles, as discussed in Chapter ???. At these momenta there is no significant zero fraction due to interactions with the detector or insufficient energy deposits (see Section 8.2.2).  $f_{\text{EM}}$  is peaked close to 1.0 for electrons, and distributed between 10% and 90% for hadrons.

These trends can be seen in the two dimensional distribution for signal in Figure 61 for stable and metastable (10 ns) events. The majority of R-Hadrons in both samples fall into the bin for  $E/p = 0$  and  $f_{\text{EM}} = 0$  because the majority of the time there is no associated jet. In the stable sample, when there often is an associated jet,  $E/p$  is typically still below 0.1, and the  $f_{\text{EM}}$  is predominantly under 0.8. In the metastable sample, on the other hand,  $E/p$  is larger but still typically below 0.1 because of actual jets produced during the decay. The  $f_{\text{EM}}$  is much lower on average in this case, below 0.1, because the 10 ns lifetime particles rarely decay before passing through the electromagnetic calorimeter. Figure 61 also includes simulated Z decays to electrons or tau leptons. From the decays

1886 to electrons it is clear that the majority of electrons have  $f_{\text{EM}}$  above 0.9. The  
 1887 tau decays include a variety of products. Muons can be seen in the bin where  
 1888  $E/p = 0$  and  $f_{\text{EM}} = 0$  because they do not have an associated jet. Electrons fall  
 1889 into the range where  $E/p > 1$  and  $f_{\text{EM}} > 0.9$ . Hadronic tau decays are the most  
 1890 common, and fall in the range of  $0.1 < f_{\text{EM}} < 0.9$  and  $E/p > 1.0$ .

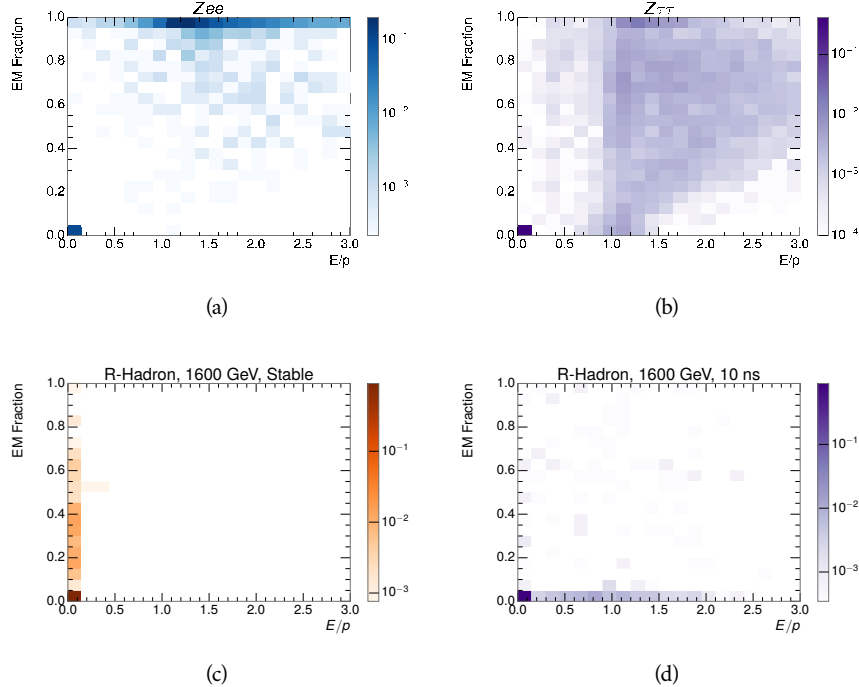


Figure 61: The normalized, two-dimensional distribution of  $E/p$  and  $f_{\text{EM}}$  for simulated  
 (a)  $Z \rightarrow ee$ , (b)  $Z \rightarrow \tau\tau$ , (c) 1200 GeV Stable R-Hadron events, and (d) 1200  
 GeV, 10 ns R-Hadron events.

1891 These differences motivate an electron rejection by requiring an  $f_{\text{EM}}$  below  
 1892 0.9. Similarly, isolated hadrons are rejected by requiring  $E/p < 1.0$ . These re-  
 1893 quirements combine to remove the majority of isolated electrons and hadrons  
 1894 but retain over 95% of the simulated signal across a range of masses and lifetimes.

## 1895 11.4 IONIZATION

1896 The final requirement on the candidate track is the primary discriminating vari-  
 1897 able, the ionization in the pixel detector. That ionization is measured in terms  
 1898 of  $dE/dx$ , which was shown for data and simulated signal events in Figure 57.  
 1899  $dE/dx$  is dramatically greater for the high mass signal particles than the back-  
 1900 grounds, which start to fall immediately after the minimally ionizing peak at 1.1  
 1901  $\text{MeV g}^{-1} \text{cm}^2$ . The  $dE/dx$  for candidate tracks must be greater than a pseudorapidity-  
 1902 dependent threshold, specifically  $1.80 - 0.11|\eta| + 0.17\eta^2 - 0.05\eta^3 \text{ MeV g}^{-1} \text{ cm}^{-2}$ ,  
 1903 in order to correct for an approximately 5% dependence of the MIP peak on  $\eta$ .  
 1904 The requirement was chosen as part of the signal region optimization, and man-

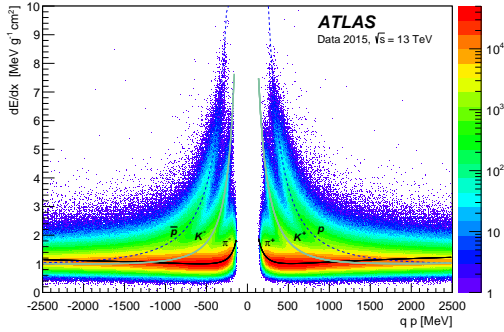


Figure 62: Two-dimensional distribution of  $dE/dx$  versus charge signed momentum ( $qp$ ) for minimum-bias tracks. The fitted distributions of the most probable values for pions, kaons and protons are superimposed.

ages to reduce the backgrounds by a factor of 100 while remaining 70-90% efficient for simulated signal events depending on the mass.

#### 11.4.1 MASS ESTIMATION

The mean value of ionization in silicon is governed by the Bethe equation and the most probable value follows a Landau-Vavilov distribution [7]. Those forms inspire a parametric description of  $dE/dx$  in terms of  $\beta\gamma$ ,

$$(dE/dx)_{MPV}(\beta\gamma) = \frac{p_1}{\beta^{p_3}} \ln(1 + [p_2 \beta\gamma]^{p_5}) - p_4 \quad (7)$$

which performs well in the range  $0.3 < \beta\gamma < 1.5$ . This range includes the expected range of  $\beta\gamma$  for the particles targeted for this search, with  $\beta\gamma \approx 2.0$  for lower mass particles ( $O(100 \text{ GeV})$ ) and up to  $\beta\gamma \approx 0.5$  for higher mass particles ( $O(1000 \text{ GeV})$ ). The parameters,  $p_i$ , are fit using a 2015 data sample of low-momentum pions, kaons, and protons as described in Ref. [76]. Figure 62 shows the two-dimensional distribution of  $dE/dx$  and momentum along with the above fitted values for  $(dE/dx)_{MPV}$ .

The above equation (7) is then numerically inverted to estimate  $\beta\gamma$  and the mass for each candidate track. In simulated signal events, the mean of this mass value reproduces the generated mass up to around 1800 GeV to within 3%, and a 3% shift is applied to correct for this difference. The mass distributions prior to this correction are shown for a few stable mass points in Figure 63. The large widths of these distributions come from the high variability in energy deposits in the pixel detector as well as the uncertainty on momentum measurements at high momentum, but the means converge to the expected values.

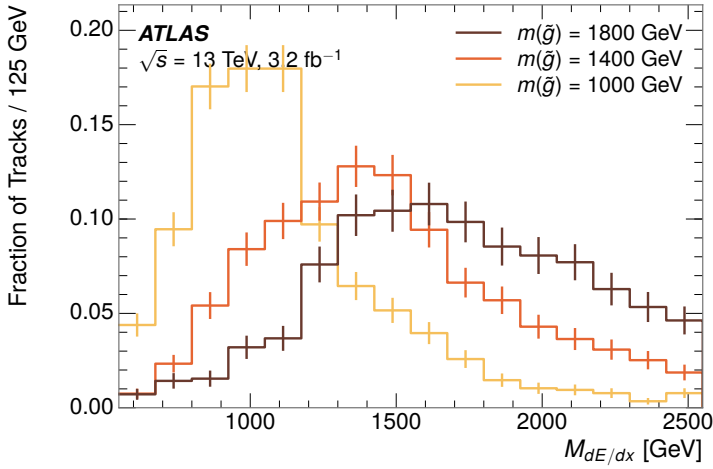


Figure 63: The distribution of mass estimated using  $dE/dx$  for simulated stable R-Hadrons with masses between 1000 and 1600 GeV.

This analysis evaluates expected yields and the resulting cross sectional limits using windows in this mass variable. The windows are formed by fitting mass distributions in simulated signal events like those in Figure 63 to Gaussian distributions and taking all events that fall within  $\pm 1.4\sigma$  of the mean. As can be seen in Figure 63, typical values for this width are  $\sigma \approx 300 - 500$  GeV depending on the generated mass.

## 11.5 EFFICIENCY

The numbers of events passing each requirement through ionization are shown in Table 4 for the full 2015 dataset and a simulated 1600 GeV, 10 ns lifetime R-Hadron sample. The table highlights the overall acceptance  $\times$  efficiency for signal events, which for this example is 19%. Between SM rejection and ionization, this signal region reduces the background of tracks which pass the kinematic requirements down by an additional factor of almost 2000.

There is a strong dependence of this efficiency on lifetime and mass, with efficiencies dropping to under 1% at low lifetimes. Figure 64 shows the dependence on both mass and lifetime for all signal samples considered in this search. The dependence on mass is relatively slight and comes predominantly from the increasing fraction of R-Hadrons which pass the ionization cut with increasing mass. The trigger and  $E_T^{\text{miss}}$  requirements are most efficient for particles that decay before reaching the calorimeters. However, the chance of a particle to be reconstructed as a high-quality track decreases significantly at low lifetimes as the particle does not propagate sufficiently through the inner detector. These effects lead to a maximum in the selection efficiency for lifetimes around 10-30 ns.

The inefficiency of this signal region at short lifetimes comes almost exclusively from an acceptance effect, in that the particles do not reach the necessary

Selection	Exp. Signal Events	Observed Events in $3.2 \text{ fb}^{-1}$
Generated	$26.0 \pm 0.3$	
$E_T^{\text{miss}}$ Trigger	$24.8 \pm 0.3$ (95%)	
$E_T^{\text{miss}} > 130 \text{ GeV}$	$23.9 \pm 0.3$ (92%)	
Track Quality and $p_T > 50$	$10.7 \pm 0.2$ (41%)	368324
Isolation Requirement	$9.0 \pm 0.2$ (35%)	108079
Track $p > 150 \text{ GeV}$	$6.6 \pm 0.2$ (25%)	47463
$M_T > 130 \text{ GeV}$	$5.8 \pm 0.2$ (22%)	18746
Electron and Hadron Veto	$5.5 \pm 0.2$ (21%)	3612
Muon Veto	$5.5 \pm 0.2$ (21%)	1668
Ionization Requirement	$5.0 \pm 0.1$ (19%)	11

Table 4: The expected number of events at each level of the selection for metastable  $1600 \text{ GeV}, 10 \text{ ns}$  R-Hadrons, along with the number of events observed in data, for  $3.2 \text{ fb}^{-1}$ . The simulated yields are shown with statistical uncertainties only. The total efficiency  $\times$  acceptance is also shown for the signal.

1952 layers of the SCT. This can be seen more clearly by defining a fiducial region  
 1953 which includes events with at least one R-Hadron that is produced with non-  
 1954 zero charge,  $p_T > 50 \text{ GeV}$ ,  $p > 150 \text{ GeV}$ ,  $|\eta| < 2.5$ , and a decay distance greater  
 1955 than 37 cm in the transverse plane. At short (1 ns) lifetimes, the acceptance into  
 1956 this region is as low as 4%. Once this acceptance is accounted for, the selection  
 1957 efficiency ranges from 25% at lifetimes of 1 ns up to 45% at lifetimes of 10 ns.

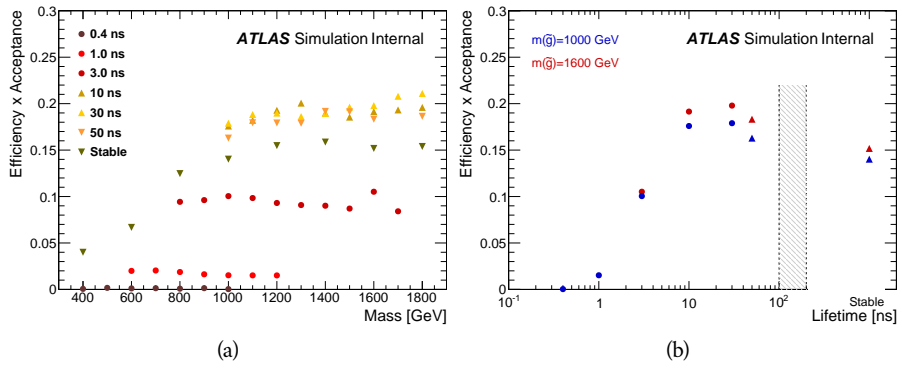


Figure 64: The acceptance  $\times$  efficiency as a function of R-Hadron (a) mass and (b) lifetime. (a) shows all of the combinations of mass and lifetime considered in this search, and (b) highlights the lifetime dependence for 1000 GeV and 1600 GeV R-Hadrons.

1958

1959 BACKGROUND ESTIMATION

---

1960 The event selection discussed in the previous section focuses on detector sig-  
 1961 natures, emphasizing a single high-momentum, highly-ionizing track. That track  
 1962 is then required to be in some way inconsistent with the expected properties  
 1963 of SM particles, with various requirements designed to reject jets, hadrons,  
 1964 electrons, and muons (Section 11.3). Therefore the background for this search comes  
 1965 entirely from reducible backgrounds that are outliers of various distributions in-  
 1966 cluding  $dE/dx$ ,  $f_{EM}$ , and  $p_T^{\text{Cone}}$ . The simulation can be tuned in various ways to  
 1967 do an excellent job of modeling the average properties of each particle type [77],  
 1968 but it is not necessarily expected to accurately reproduce outliers. For this rea-  
 1969 sons, the background estimation used for this search is estimated entirely using  
 1970 data.

## 1971 12.1 BACKGROUND SOURCES

1972 SM charged particles with lifetimes long enough to form tracks in the inner de-  
 1973 tector can be grouped into three major categories based on their detector inter-  
 1974 actions: hadrons, electrons, and muons. Every particle that enters into the back-  
 1975 ground for this search belongs to one of these types. Relatively pure samples of  
 1976 tracks from each of these types can be formed in data by inverting the various  
 1977 rejection techniques in Section 11.3. Specifically, muons are selected requiring  
 1978 medium muon identification, electrons requiring  $E/p > 1.0$  and  $f_{EM} > 0.95$ ,  
 1979 and hadrons requiring  $E/p > 1.0$  and  $f_{EM} < 0.95$ .

1980 Figure 65 shows the distributions of momentum and  $dE/dx$  for these cate-  
 1981 gories in data, after requiring the event level selection as well as the track re-  
 1982 quirements on  $p_T$ , hits, and  $N_{\text{split}}$ , as discussed in Section 11.2. Simulated signal  
 1983 events are included for reference. These distribution are only illustrative of the  
 1984 differences between types, as the rejection requirements could alter their shape.  
 1985 This is especially significant for momentum which enters directly into  $E/p$  and  
 1986 can indirectly affect muon identification. However the various types show clear  
 1987 differences in both distributions. The distributions of momentum are not nec-  
 1988 cessarily expected to match between the various types because the production  
 1989 mechanisms for each type result in different kinematic distributions.  $dE/dx$  is  
 1990 also different between types because of incomplete isolation; although the re-  
 1991 quirement on  $N_{\text{split}}$  helps to reduce the contribution of nearby particles it does  
 1992 not completely remove the effect of overlaps. Muons are better isolated because  
 1993 they do not have the additional particle from hadronization present for hadrons  
 1994 and they are significantly less likely do interact with the detector and produce  
 1995 secondary particles compared to hadrons and electrons. Thus muons have the  
 1996 smallest fraction of  $dE/dx$  above the threshold of  $1.8 \text{ MeVg}^{-1}\text{cm}^2$ ; hadrons and  
 1997 electrons have a larger fraction above this threshold.

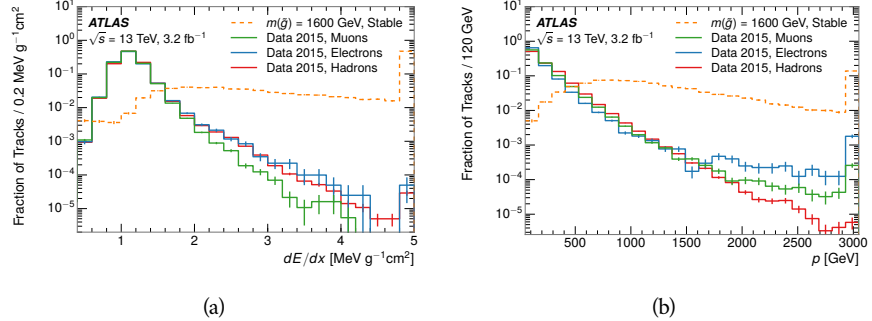


Figure 65: The distribution of (a)  $dE/dx$  and (b) momentum for tracks in data and simulated signal after requiring the event level selection and the track selection on  $p_T$ , hits, and  $N_{\text{split}}$ . Each sub-figure shows the normalized distributions for tracks classified as hadrons, electrons, and muons in data and R-Hadrons in the simulated signal.

1998 It is difficult to determine what fraction of each particle type enters into the final signal region.  
 1999 The background method will not have significant dependence  
 2000 on the relative contributions of each species, but it is useful to understand the  
 2001 differences between each when considering the various tests of the method.

## 2002 12.2 PREDICTION METHOD

2003 The data-driven background estimation relies on the independence between ion-  
 2004 ization and other kinematic variables in the event. For standard model particles  
 2005 with momenta above 50 GeV,  $dE/dx$  is not correlated with momentum; though  
 2006 there is a slight relativistic rise as momentum increases, the effect is small com-  
 2007 pared to the width of the distribution of ionization energy deposits.. So, the  
 2008 proposed method to estimate the mass distribution of the signal region is to use  
 2009 momentum from a track with low  $dE/dx$  (below the threshold value) and to com-  
 2010 bine it with a random  $dE/dx$  value from a  $dE/dx$  template. The resulting track is  
 2011 just as likely as the original, so a number of such random generations provide the  
 2012 expected distributions of momentum and ionization. These are then combined  
 2013 using the parametrization described in Section 11.4.1 to form a distribution of  
 2014 mass for the signal region.

2015 Algorithmically this method is implemented by forming two distinct Control  
 2016 Regions (**CR**s). The first **CR**, CR1, is formed by applying the entire event selec-  
 2017 tion from Chapter 11 up to the  $dE/dx$  and mass requirements. The  $dE/dx$  re-  
 2018 quirement is instead inverted for this region. Because of the independence of  
 2019  $dE/dx$ , the tracks in this control region have the same kinematic distribution  
 2020 as the tracks in the signal region, and are used to measure a two-dimensional  
 2021 template of  $p$  and  $\eta$ . The second **CR**, CR2, is formed from the event selection  
 2022 through the  $dE/dx$  requirement, but with an inverted  $E_T^{\text{miss}}$  requirement. The  
 2023 tracks in this control region are expected to have similar  $dE/dx$  distributions to  
 2024 the signal region before the ionization requirement, and so this region is used to  
 2025 measure a two-dimensional template of  $dE/dx$  and  $\eta$ .

2026     The contribution of any signal to the control regions is minimized by the in-  
 2027     verted selection requirements. Only less than 10% of simulated signal events  
 2028     have either  $dE/dx$  or  $E_T^{\text{miss}}$  below the threshold values in the original signal re-  
 2029     gion, while the backgrounds are significantly enhanced by inverting those re-  
 2030     quirements. The signal contamination is less than 1% in both control regions  
 2031     for all of the simulated masses and lifetimes considered in this analysis.

2032     With those measured templates, the shape of the mass estimation is generated  
 2033     by first selecting a random ( $p$ ,  $\eta$ ) combination from CR1. This momentum  
 2034     value is combined with a  $dE/dx$  value taken from the appropriate distribution  
 2035     of  $dE/dx$  for the selected  $\eta$  from CR2. The use of  $\eta$  in both random samplings  
 2036     controls for any correlation between  $p$ ,  $dE/dx$ , and  $\eta$ . Those values are then  
 2037     used to calculate a mass in the same way that is done for regular tracks in data,  
 2038     see Section 11.4.1. As this procedure includes all  $dE/dx$  values, the cut at 1.8  
 2039     MeVg $^{-1}$ cm $^2$  is then enforced to fully model the signal region. The generated  
 2040     mass distribution is then normalized by scaling the background estimate to the  
 2041     data in the region  $M < 160$  GeV, where signals of this type have already been  
 2042     excluded [61]. This normalization uses the distributions of mass generated with-  
 2043     out the ionization requirement.

2044     The statistical uncertainties on these background distributions are calculated  
 2045     by independently fluctuating each bin of the input templates according to their  
 2046     Poisson uncertainties. These fluctuations are repeated a large number of times,  
 2047     and the uncertainty on the resulting distribution is taken as the root mean square  
 2048     (RMS) deviation of the fluctuations from the average. As the procedure uses one  
 2049     million random combinations to generate the distributions, The statistical un-  
 2050     certainty from the actual random generations is negligible compared to the un-  
 2051     certainty from measuring the templates.

## 2052    12.3 VALIDATION

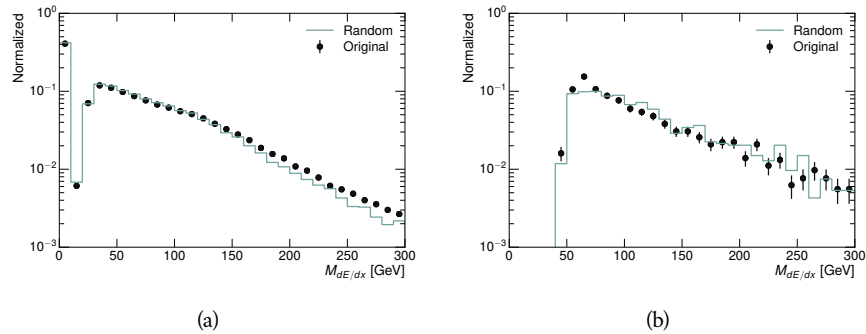
2053     The validity of the background estimation technique can be evaluated in both  
 2054     data and simulation. The underlying assumption that random combinations of  
 2055      $dE/dx$  and momentum can predict a mass distribution in an orthogonal region  
 2056     can be tested using simulated samples where concerns like multiple particle types  
 2057     can be controlled. Using the same technique in another set of signal-depleted  
 2058     regions in data then extends this confidence to the more complicated case where  
 2059     several particle species are inherently included.

### 2060    12.3.1 CLOSURE IN SIMULATION

2061     The first test of the procedure is done using a simulated sample of  $W \rightarrow \mu\nu$   
 2062     decays. These types of events provide the ingredients required to test the back-  
 2063     ground estimate,  $E_T^{\text{miss}}$  and isolated tracks, with high statistics. In this example  
 2064     there is no signal, so simulated events in the orthogonal CRs are used to estimate  
 2065     the shape of the mass distribution of the simulated events in the signal region. To  
 2066     reflect the different topology for W boson decays, the CRs use slightly modified  
 2067     definitions. In all CRs, the requirement of  $p > 150$  GeV and the SM rejection

2068 requirements are removed. Additionally, for the signal region the requirement  
 2069 on  $E_T^{\text{miss}}$  is relaxed to 30 GeV and the corresponding inverted requirement on  
 2070 CR2 is also set at 30 GeV.

2071 With these modified selections, the simulated and randomly generated distri-  
 2072 butions of  $M_{dE/dx}$  are shown in Figure 66. This figure includes the mass distri-  
 2073 butions before and after the requirement on  $dE/dx$ , which significantly shapes  
 2074 the distributions. In both cases the background estimation technique repro-  
 2075 duces the shape of  $M_{dE/dx}$  in the signal region. There is a small difference in the pos-  
 2076 itive tail of the mass distribution prior to the ionization cut, where the random  
 2077 events underestimate the fraction of tracks with mass above 150 GeV by about  
 2078 20%. After the ionization requirement, however, this discrepancy is not present  
 2079 and the two distributions agree to within statistical uncertainties.



2080 Figure 66: The distribution of  $M_{dE/dx}$  (a) before and (b) after the ionization requirement  
 2081 for tracks in simulated W boson decays and for the randomly generated back-  
 2082 ground estimate.

2083 This ability to reproduce the shape of the mass distribution in simulated events  
 2084 shows that the technique works as expected. No significant biases are acquired  
 2085 in using low  $dE/dx$  events to select kinematic templates or in using low  $E_T^{\text{miss}}$   
 2086 events to select ionization templates, as either would result in a mismodeling of  
 the shape of the mass distribution. The simulated events contain only one par-  
 ticle type, however, so this test only establishes that the technique works well  
 when the the CRs are populated by exactly the same species.

### 2087 12.3.2 VALIDATION REGION IN DATA

2088 The second test of the background estimate is performed using data in an or-  
 2089 thogonal validation region. The validation region, and the corresponding CRs,  
 2090 are formed using the same selection requirements as in the nominal method but  
 2091 with a modified requirement on momentum,  $50 < p[\text{GeV}] < 150$ . This allows  
 2092 the technique to be checked in a region with very similar properties but where  
 2093 the signal is depleted, as the majority of the signal has momentum above 150  
 2094 GeV while the backgrounds are enhanced below that threshold. Any biases on  
 2095 the particle composition of the CRs for the signal region will be reflected in the  
 2096 CRs used to estimate the mass distribution in the validation region.

2097     Figure 67 shows the measured and randomly generated mass distributions for  
 2098 data before and after the ionization requirement. The background estimate does  
 2099 an excellent job of modeling the actual background before the ionization require-  
 2100 ment, with good agreement to within the statistical uncertainties out to the limit  
 2101 of the mass distribution. There are very few events in the validation region after  
 2102 the ionization requirement, but the few observed events are consistent with the  
 2103 background prediction. The good agreement in this validation region provides  
 2104 a confirmation that the technique works even in the full-complexity case with  
 2105 multiple particle types entering the distributions. Any bias from changes in par-  
 2106 ticle composition between regions is small compared to statistical uncertainties.

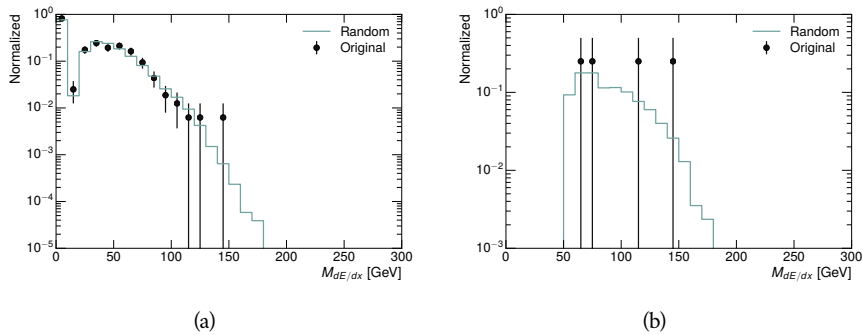


Figure 67: The distribution of  $M_{dE/dx}$  (a) before and (b) after the ionization require-  
 ment for tracks in the validation region and for the randomly generated back-  
 ground estimate.



2107

2108 SYSTEMATIC UNCERTAINTIES AND RESULTS

---

## 2109 13.1 SYSTEMATIC UNCERTAINTIES

2110 A number of systematic uncertainties affect the interpretation of the results of  
 2111 the search. These uncertainties can broken down into two major categories,  
 2112 those which affect the estimate of the background using data and those which  
 2113 affect the measurement of the signal yield estimated with simulated events. The  
 2114 total measured systematic uncertainties are 7% for the background estimation  
 2115 and approximately 32% for the signal yield depending on lifetime. These system-  
 2116atic uncertainties are expected to be small compared to the statistical fluctuations  
 2117 of the measured yields so that measured cross-sectional limits will be dominated  
 2118 by statistical uncertainties. The following sections describe each source of sys-  
 2119 tematic uncertainty for each of the two types.

## 2120 13.1.1 BACKGROUND ESTIMATE

2121 The systematic uncertainties on the background estimate come primarily from  
 2122 considering alternative methods for generating the background distributions.  
 2123 These uncertainties are small compared to the statistical uncertainties on the  
 2124 background estimate which come from the limited statistics in measuring the  
 2125 template distributions, as described in Section 12.2. They are summarized in  
 2126 Table 5.

Source of Uncertainty:	Value [%]
Analytic Description of $dE/dx$	4.0
Muon Fraction (Stable Region only)	3.0
IBL Ionization Correction	3.8
Normalization	3.0
Total (Metastable Region):	6.3
Total (Stable Region):	7.0

Table 5: A summary of the sources of systematic uncertainty for the data-driven back-  
 ground in the signal region. If the uncertainty depends on the mass, the maxi-  
 mum values are reported.

2127 13.1.1.1 ANALYTIC DESCRIPTION OF  $DE/DX$ 

2128 The background estimate uses a binned template distribution to estimate the  
 2129  $dE/dx$  of tracks in the signal region, as described in Section 12.2. It is also possi-

ble to fit that measured distribution to a functional form to help smooth the distribution in the tails of  $dE/dx$  where the template is driven by a small number of tracks. Both Landau convolved with a Gaussian and Crystal Ball functions are considered as the functional form and used to re-estimate the background distribution. The deviations compared to the nominal method are found to be 4%, and this is taken as a systematic uncertainty to cover the inability carefully predict the contribution from the long tail of  $dE/dx$  where there are few measurements available in data.

#### 2138 13.1.1.2 MUON FRACTION

2139 The stable region of the analysis explicitly includes tracks identified as muons,  
 2140 which have a known difference in their  $dE/dx$  distributions compared to non-  
 2141 muon tracks (Section 12.1). To account for a difference in muon fraction be-  
 2142 tween the background region and the signal region for this selection, the  $dE/dx$   
 2143 templates for muons and non-muons are measured separately and then the rel-  
 2144 ative fraction of each is varied in the random generation. The muon fraction  
 2145 is varied by its statistical uncertainty and the resulting difference of 3% in back-  
 2146 ground yield is taken as the systematic uncertainty.

#### 2147 13.1.1.3 IBL CORRECTIONS

2148 The Insertible B-Layer (IBL), described in Section 6.3.1, received a significant  
 2149 dose of radiation during the data collection in 2015. The irradiation can cause  
 2150 a drift in the frontend electronics and thus alter the  $dE/dx$  measurement which  
 2151 includes the ToT output by the IBL. These effects are corrected for in the nominal  
 2152 analysis by scaling the  $dE/dx$  measurements by a constant factor derived for  
 2153 each run to match the average  $dE/dx$  value to a reference run where the IBL  
 2154 was known to be stable to this effect. However, this corrective factor does not  
 2155 account for inter-run variations. To account for this potential drift of  $dE/dx$ ,  
 2156 the correction procedure is repeated by varying the corrections up and down by  
 2157 the maximal run-to-run variation from the full data-taking period, which results  
 2158 in an uncertainty of 3.8%.

#### 2159 13.1.1.4 NORMALIZATION

2160 As described in Section 12.2, the generated distribution of masses is normalized  
 2161 in a shoulder region ( $M < 160$  GeV) where signals have been excluded by pre-  
 2162 vious analyses. That normalization factor is varied by its statistical uncertainty  
 2163 and the resulting fluctuation in the mass distribution of 3% is taken as a system-  
 2164 atic uncertainty on the background estimate.

#### 2165 13.1.2 SIGNAL YIELD

2166 The systematic uncertainties on the signal yield can be divided into three cate-  
 2167 gories; those on the simulation process, those on the modeling of the detector  
 2168 efficiency or calibration, and those affecting the overall signal yield. They are  
 2169 summarized in Table 5. The largest uncertainty comes from the uncertainty on

2170 the production cross section for gluinos, which is the dominant systematic un-  
 2171 certainty in this analysis.

Source of Uncertainty	-[%]	+[%]
ISR Modeling (Metastable Region)	1.5	1.5
ISR Modeling (Stable Region)	14	14
Pile-up Reweighting	1.1	1.1
Trigger Efficiency Reweighting	0.9	0.9
$E_T^{\text{miss}}$ Scale	1.1	2.2
Ionization Parametrization	7.1	0
Momentum Parametrization	0.3	0.0
Electron Rejection	0.0	0.0
Hadron Rejection	0.0	0.0
$\mu$ Identification	4.3	4.3
Luminosity	5	5
Signal size uncertainty	28	28
Total (Metastable Region)	30	29
Total (Stable Region)	33	32

Table 6: A summary of the sources of systematic uncertainty for the simulated signal yield. The uncertainty depends on the mass and lifetime, and the maximum negative and positive values are reported in the table.

### 2172 13.1.2.1 ISR MODELING

2173 As discussed in Section 10.2, MadGraph is expected to reproduce the distribution  
 2174 of ISR in signal events more accurately than the nominal Pythia samples. The  
 2175 analysis reweights the distribution of ISR in the simulated signal events to match  
 2176 the distribution found in generated MadGraph samples. This has an effect on the  
 2177 selection efficiency in the signal samples, where ISR contributes to the generation  
 2178 of  $E_T^{\text{miss}}$ . To account for the potential inaccuracy on the simulation of ISR at high  
 2179 energies, half of the difference between the signal efficiency with the reweighted  
 2180 distribution and the original distribution is taken as a systematic uncertainty.

### 2181 13.1.2.2 PILEUP REWEIGHTING

2182 The simulated events were generated prior to data collection with an estimate of  
 2183 the average number of interactions per bunch crossing. This estimate does not  
 2184 match the value of pileup during actual data collection, but a large fraction of the  
 2185 simulated events would be discarded in order to match the distribution in data.  
 2186 Therefore the simulated signal events are not reweighted for pileup by default  
 2187 in the analysis. The effect of the pileup on signal efficiency is not expected to  
 2188 depend on the mass or lifetime of the generated signal events, which allows all

2189 of the generated signal events to be used together to assess the pileup dependence.  
 2190 To account for the potential effect of the difference in the number of interactions  
 2191 per bunch crossing between data and simulation, the difference in yield between  
 2192 the nominal signal events and the reweighted events averaged over all masses  
 2193 and lifetimes is taken as a systematic uncertainty on the yield for each mass and  
 2194 lifetime (1.1%).

### 2195 13.1.2.3 TRIGGER EFFICIENCY REWEIGHTING

2196 As described in Section 11.2, the selection for this analysis does not require a suf-  
 2197 ficiently large value of  $E_T^{\text{miss}}$  to be above the plateau of trigger efficiency. There-  
 2198 fore, some signal events which would otherwise pass the event selection can be  
 2199 excluded because of the trigger requirement. These effects can be difficult to es-  
 2200 timate in simulation, and thus are constrained by comparing data and simulated  
 2201 events in an alternative W boson region which uses decays to muons to find a rel-  
 2202 atively pure sample of events with missing energy. The trigger efficiency for data  
 2203 and simulated W events are shown in Figure 68. The comparison between data  
 2204 and MC in this region constrains the simulation of the trigger efficiency. The  
 2205 simulated signal events are reweighted by the ratio of data to simulation in the  
 2206 W boson decays, while the difference between the data and simulation in those  
 2207 decays is taken as a systematic uncertainty. This results in an uncertainty of only  
 2208 0.9% as the majority of events are well above the plateau and the disagreement  
 2209 between data and simulation is small even below that plateau.

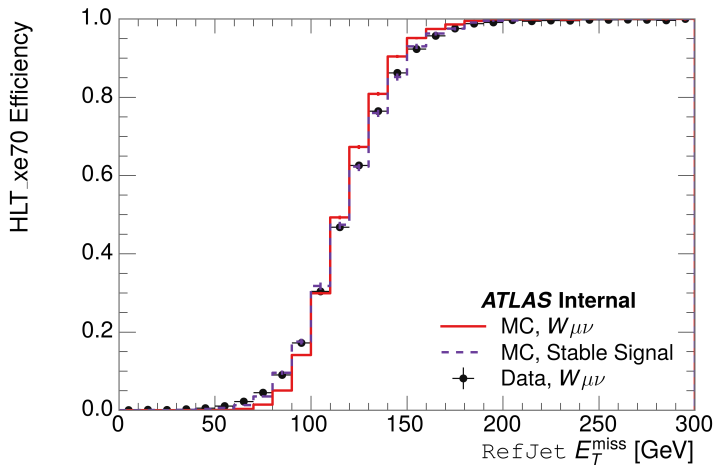


Figure 68: The trigger efficiency for the HLT\_xe70 trigger requirement as a function of Calorimeter  $E_T^{\text{miss}}$  for simulated data events with a W boson selection. Simulated signal events and simulated W boson events are also included.

### 2210 13.1.2.4 MISSING TRANSVERSE MOMENTUM SCALE

2211 The ATLAS Combined Performance (CP) group provides a default recommenda-  
 2212 tion for systematic variations of jets and missing energy (**note: I'm not quite**  
 2213 **sure what to cite for this - I don't see any papers from the jet/met group**

Systematic Variation	-[%]	+[%]
JET_GroupedNP_1	-0.7	1.3
JET_GroupedNP_2	-0.7	1.2
JET_GroupedNP_3	-0.5	1.3

Table 7: Example of the contributing systematic variations to the total systematic for the  $E_T^{\text{miss}}$  Scale, as measured in a 1200 GeV, Stable R-Hadron signal sample.

2214 **after this was implemented).** These variations enter into this analysis only in  
 2215 the requirement on  $E_T^{\text{miss}}$ . The effect of the measured scale of  $E_T^{\text{miss}}$  is evaluated  
 2216 by varying the  $E_T^{\text{miss}}$  scale according to the one sigma variations provided by all  
 2217 **CP** recommendations on objects affecting event kinematics in simulated signal  
 2218 events. Missing energy is reconstructed from fully reconstructed objects so any  
 2219 systematic uncertainties affecting jets, muons, electrons, or the  $E_T^{\text{miss}}$  soft terms  
 2220 are included. The only non-negligible contributions found using this method are  
 2221 itemized in Table 7 for an example signal sample (1200 GeV, Stable R-Hadron),  
 2222 where the systematic is measured as the relative difference in the final signal ef-  
 2223 ficiency after applying the associated variation through the CP tools. The only  
 2224 variations that are significant are the grouped jet systematic variations, which  
 2225 combine recommended jet systematic uncertainties into linearly independent  
 2226 variations.

2227 As the peak of the reconstructed  $E_T^{\text{miss}}$  distribution in the signal is significantly  
 2228 above the current threshold for events which pass the trigger requirement, the  
 2229 effect of scale variation is expected to be small, which is consistent with the mea-  
 2230 sured systematic of approximately 2%. Events which do not pass the trigger re-  
 2231 quirement usually fail because there are no ISR jets in the event to balance the  
 2232  $R$ -hadrons' transverse momentum, so the reconstructed  $E_T^{\text{miss}}$  is low and there-  
 2233 fore also expected to be not very sensitive to scale changes.

### 2234 13.1.2.5 MOMENTUM PARAMETRIZATION

2235 The uncertainty on the signal efficiency from track momentum is calculated us-  
 2236 ing the **CP** group recommendations for tracks. In particular, only one recom-  
 2237 mended systematic variation affects track momentum, the sagitta bias for  $q/P$ .  
 2238 This uncertainty is propagated to the final selection efficiency by varying the  
 2239 track momentum by the recommended one sigma variation, and the associated  
 2240 uncertainty is found to be negligible (0.3%).

### 2241 13.1.2.6 IONIZATION REQUIREMENT

2242 The  $dE/dx$  distributions in data and simulated events have different most prob-  
 2243 able values, which is due in part to radiation effects in the detector that are not  
 2244 fully accounted for in the simulation. The difference does not affect the mass  
 2245 measurement used in this analysis, as independent calibrations are done in sim-  
 2246 ulation and in data. However, it does affect the efficiency of the high  $dE/dx$   
 2247 selection requirement. To calculate the size of the effect on the signal efficiency,

the  $dE/dx$  distribution in signal simulation is scaled by a scale factor obtained from comparing the  $dE/dx$  distribution of inclusive tracks in data and in simulation. The difference in efficiency for this sample with a scaled  $dE/dx$  distribution, relative to the nominal case, is taken as a systematic uncertainty on signal efficiency. The uncertainty is as large as 7% for low masses and falls to a negligible effect for large masses.

#### 13.1.2.7 ELECTRON AND JET REJECTION

The systematic uncertainty on the electron rejection is measured by varying the EM fraction requirement significantly, from 0.95 to 0.9. This is found to have a less than 0.04% effect on signal acceptance, on average, and so is completely negligible. Similarly, the uncertainty on jet rejection is measured by tightening the  $E/p$  requirement from 0.5 to 0.4. This is found to have no effect on signal acceptance, so again the systematic is again negligible.

#### 13.1.2.8 MUON VETO

The metastable signal region requires that the candidate tracks are not identified as medium muons because the majority of R-Hadrons in the lifetime range included in that region do not reach the muon spectrometers before they decay. However, the exponential tail of the R-Hadron lifetime distribution results in some R-Hadrons traversing the muon spectrometer. These can still fail the muon medium identification because they can fail on the requirement on the number of precision hits required to pass the loose selection because they arrive late to the muon spectrometer. This can be seen in Figure 69, which shows the efficiency of the muon veto as a function of  $1/\beta$ , for two simulated stable R-Hadron samples.

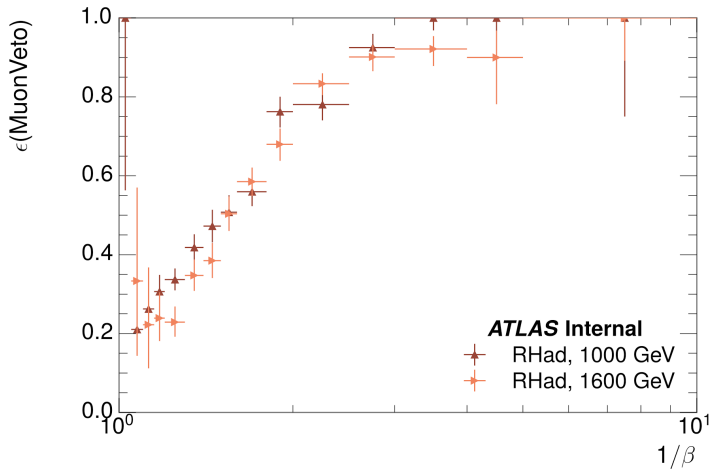


Figure 69: The efficiency of the muon veto for  $R$ -hadrons of two different masses, as a function of  $\frac{1}{\beta}$  for simulated R-Hadron tracks.

Thus, the efficiency of the muon veto depends on the timing resolution of the spectrometer, so an uncertainty is applied to the signal efficiency to cover dif-

ferences in timing resolution between data and simulation. First, a sample of  $Z \rightarrow \mu\mu$  events is selected in data in which one of the muons has a late arrival time measured in the Monitored Drift Tube ([MDT](#)). Then the reconstructed  $\beta$  distribution is compared to the distribution in simulated  $Z \rightarrow \mu\mu$  events; the difference between these two distributions reflects the difference in timing resolution between data and simulation. To emulate this difference in simulated signal events, the magnitude of the difference is used to scale and shift the true  $\beta$  distribution of R-Hadrons in simulation. Signal events are then reweighted based on this varied  $\beta$  distribution, and the difference in the efficiency of the muon veto selection is compared with the nominal and reweighted true  $\beta$  distributions. The difference in muon veto efficiency is taken as a systematic uncertainty of the muon veto.

The comparison of reconstructed  $\beta$  between data and simulation is performed separately in the barrel, transition, and endcap regions of the spectrometer, and the reweighting of the true  $\beta$  distribution in signal is done per region. The comparison of average reconstructed [MDT](#)  $\beta$  between data and simulation for the barrel region is shown in Figure 70 for  $Z \rightarrow \mu\mu$  events. As expected, The uncertainty is found to be negligible for  $R$ -hadrons with short lifetimes, and is only significant for lifetimes above 30 ns.

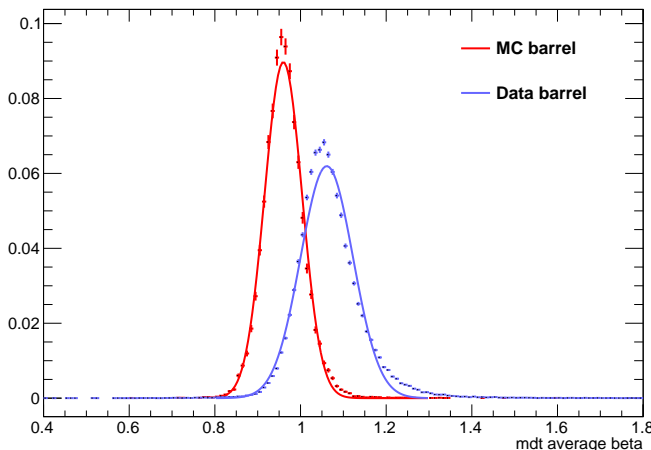


Figure 70: The average reconstructed MDT  $\beta$  distribution for  $Z \rightarrow \mu\mu$  events in which one of the muons is reconstructed as a slow muon, for both data and simulation. A gaussian fit is superimposed.

### 13.1.2.9 LUMINOSITY

The luminosity uncertainty is provided by a luminosity measurement on [ATLAS](#) and was measured to be 5% at the time of the publication of this analysis.

### 13.1.2.10 SIGNAL SIZE

As discussed in Section 10.2, the signal cross sections are calculated at [NLO](#) in the strong coupling constant with a resummation of soft-gluon emission at [NLL](#). The

Selection Region	Expected Background	Data
Stable	$17.2 \pm 2.6 \pm 1.2$	16
Metastable	$11.1 \pm 1.7 \pm 0.7$	11

Table 8: The estimated number of background events and the number of observed events in data for the specified selection regions prior to the requirement on mass. The background estimates show statistical and systematic uncertainties.

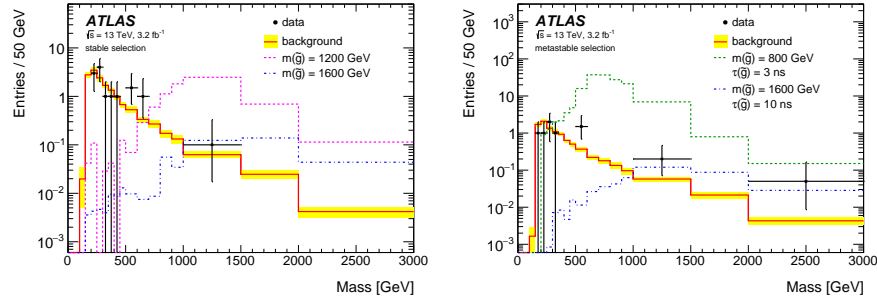


Figure 71: The observed mass distribution of events in data and the generated background distribution in (a) the stable and (b) the metastable signal region. A few example simulated signal distributions are superimposed.

uncertainties on those cross sections are between 14% to 28% for the R-Hadrons in the range of 400 to 1800 GeV [73, 74], where the uncertainty increases with the mass.

## 13.2 FINAL YIELDS

This full analysis was performed using the  $3.2 \text{ fb}^{-1}$  from the 2015 data-taking. Using the selections discussed in Chapter 11, sixteen events were observed in the stable signal region and eleven events were observed in the metastable signal region, prior to requirements on the candidate track mass. The background estimate discussed in Chapter 12 predicts  $17 \pm 2.6(\text{stat}) \pm 1.2(\text{syst})$  events for the stable region and  $11.1 \pm 1.7(\text{stat}) \pm 0.7(\text{syst})$  events for the metastable region. These counts are summarized in Table 8.

The mass estimated using  $dE/dx$  (Section 11.4.1) provides the final discriminating variable, where the signal would be expected as an excess in the falling exponential tail of the expected background. The observed distribution of masses is shown in Figure 71, along with the predicted distribution from the background estimate for each signal region. Both include a few example simulated signal distributions, which show the scale of an excess were the R-Hadron signals present. There is no statistically significant evidence of an excess in the data over the background estimation. From this distribution it is clearly possible to rule out signals with lower masses, around 1200 GeV, which have larger cross sections.

## 2319 13.3 CROSS SECTIONAL LIMITS

2320 Because there is no observed significant excess of events in the signal region,  
 2321 this analysis sets upper limits on the allowed cross section for R-Hadron produc-  
 2322 tion. These limits are set for each mass point by counting the observed events in  
 2323 data, along with the expected background and simulated signal events, in win-  
 2324 dows of mass. The mass windows are formed by fitting the distribution of signal  
 2325 events to a Gaussian distribution, and the window is then  $\pm 1.4\sigma$  around the cen-  
 2326 ter of that Gaussian. Two examples of the windows formed by this procedure  
 2327 are shown in Tables 9–10, for the stable and 10 ns working points. The corre-  
 2328 sponding counts of observed data, expected background, and simulated signal  
 2329 for those same working points are shown in Tables 11–12. Appendix B includes  
 2330 the mass windows and counts for all of the considered signal points.

$m(\tilde{g})$ [GeV]	Left Extremum [GeV]	Right Extremum [GeV]
1000	655	1349
1100	734	1455
1200	712	1631
1300	792	1737
1400	717	1926
1500	815	2117
1600	824	2122
1700	900	2274
1800	919	2344

Table 9: The left and right extremum of the mass window for each generated mass point with a 10 ns lifetime.

$m(\tilde{g})$ [GeV]	Left Extremum [GeV]	Right Extremum [GeV]
800	627	1053
1000	726	1277
1200	857	1584
1400	924	1937
1600	993	2308
1800	1004	2554

Table 10: The left and right extremum of the mass window used for each generated stable mass point.

2331 The 95% confidence level upper limits on the cross sections for a large grid of  
 2332 masses (between 800 and 1800 GeV) and lifetimes (between 0.4 and stable) are  
 2333 extracted from these counts with the  $CL_S$  method using the profile likelihood

$m(\tilde{g})$ [GeV]	Expected Signal	Expected Background	Observed Data
800	$462.83 \pm 14.86$	$1.764 \pm 0.080$	2.0
1000	$108.73 \pm 3.38$	$1.458 \pm 0.070$	1.0
1200	$31.74 \pm 0.95$	$1.137 \pm 0.060$	1.0
1400	$10.22 \pm 0.29$	$1.058 \pm 0.058$	1.0
1600	$3.07 \pm 0.09$	$0.947 \pm 0.054$	1.0
1800	$1.08 \pm 0.05$	$0.940 \pm 0.054$	1.0

Table 11: The expected number of signal events, the expected number of background events, and the observed number of events in data with their respective statistical errors within the respective mass window for each generated stable mass point

$m(\tilde{g})$ [GeV]	Expected Signal	Expected Background	Observed Data
1000	$144.48 \pm 5.14$	$1.499 \pm 0.069$	2.0
1100	$73.19 \pm 2.61$	$1.260 \pm 0.060$	2.0
1200	$41.54 \pm 1.41$	$1.456 \pm 0.067$	2.0
1300	$22.58 \pm 0.77$	$1.201 \pm 0.058$	2.0
1400	$12.70 \pm 0.42$	$1.558 \pm 0.071$	2.0
1500	$6.73 \pm 0.24$	$1.237 \pm 0.060$	2.0
1600	$3.90 \pm 0.13$	$1.201 \pm 0.058$	2.0
1700	$2.27 \pm 0.07$	$1.027 \pm 0.052$	2.0
1800	$1.34 \pm 0.04$	$1.019 \pm 0.052$	2.0

Table 12: The expected number of signal events, the expected number of background events, and the observed number of events in data with their respective statistical errors within the respective mass window for each generated mass point with a lifetime of 10 ns.

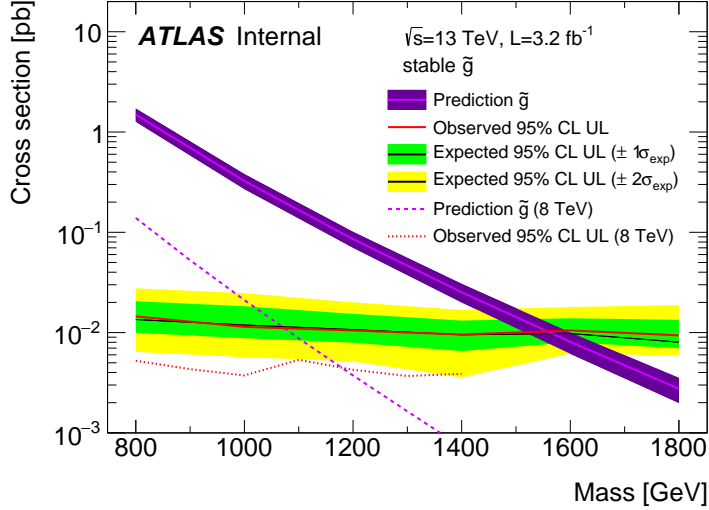


Figure 72: The observed and expected cross section limits as a function of mass for the stable simulated signal. The predicted cross section values for the corresponding signals are included.

ratio as a test statistic [78]. For this procedure, the systematic uncertainties estimated for the signal and background yields are treated as Gaussian-distributed nuisance parameters. The uncertainty on the normalization of the expected background distribution is included in the expected background events. At this point the expected cross section limit is calculated for both the metastable and stable signal region for each lifetime point, and the region with the best expected limit is selected for each lifetime. Using that procedure, the metastable region is used for lifetimes up to and including 30 ns, and the stable region for lifetimes above it.

The resulting cross-sectional upper limits are shown as a function of mass in Figure 72 and Figure 73 for each lifetime considered. The limits are interpolated linearly between each mass point, and the dependence of the limit on the mass is small as the efficiency is relatively constant for large R-Hadron masses. There is however a strong dependence on lifetime, as discussed in Section 11.5, where the probability to form a fully reconstructed track and the kinematic freedom to produce  $E_T^{\text{miss}}$  result in a local maximum in the limit at 10–30 ns. The figures also include the expected cross section for pair-produced gluino R-Hadrons for reference. For the 10 ns and stable cross section limits, both the observed limit and expected cross section for the Run 1, 8 TeV version of this analysis are included. There the cross sectional limits are lower because of the increased available luminosity, while the signal cross sections were also much lower because of the lower collision energy.

## 13.4 MASS LIMITS

The cross-sectional limits can then be used to derive a lower mass limit for gluino R-Hadrons by comparing them to the theoretically predicted production cross

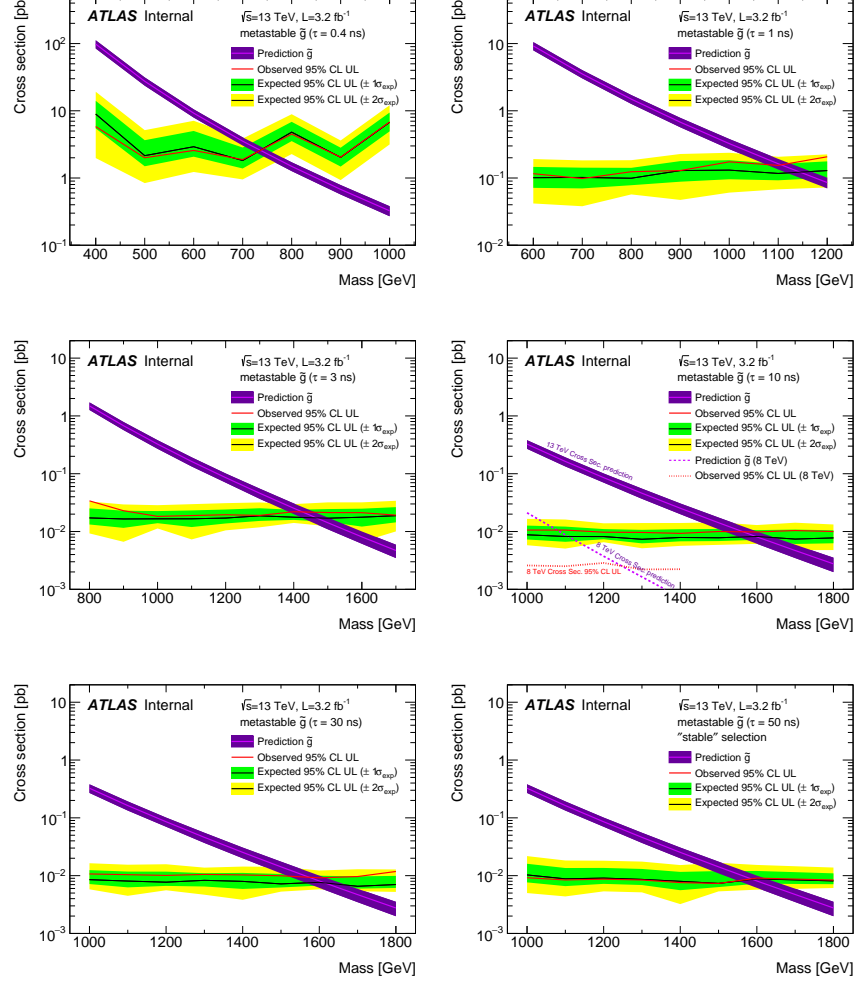


Figure 73: The observed and expected cross section limits as a function of mass for each generated lifetime. The predicted cross section values for the corresponding signals are included.

sections. These mass limits range from only 740 GeV at the lowest lifetimes considered, where the selection efficiency is very low, to up to 1580 GeV at 30 ns where the selection efficiency is maximized. The observed and expected mass limits for each lifetime point are detailed in Table 13, which also lists which selection region was used for each lifetime. These excluded range of masses as a function of lifetime is also shown in Figure 74. The Run 1 limits are included for comparison; the limits have increased by about 200 GeV on average. The search has also improved since the previous incarnation from Run 1 in optimizing the region between 30 GeV and detector-stable lifetimes by introducing the second signal region. The definition of the stable region prevents the significant drop in mass limit that occurred above 30 GeV in the Run 1 analysis.

Selection	$\tau$ [ns]	$M_{\text{obs}} > [\text{GeV}]$	$M_{\text{exp}} > [\text{GeV}]$
Metastable	0.4	740	730
"	1.0	1110	1150
"	3.0	1430	1470
"	10	1570	1600
"	30	1580	1620
Stable	50	1590	1590
"	stable	1570	1580

Table 13: The observed and expected 95% CL lower limit on mass for gluino R-Hadrons for each considered lifetime.

## 13.5 CONTEXT FOR LONG-LIVED SEARCHES

This search plays an important role in the current, combined [ATLAS](#) search for long lived particles. The mass limits provided by various [ATLAS](#) searches for long-lived gluino R-Hadrons can be seen in Figure 75. This search provides the most competitive limit for lifetimes between 3 ns up through very long lifetimes, where it is still competitive with dedicated searches for stable particles. The limits placed on gluino production are very similar to the limits on promptly decaying models.

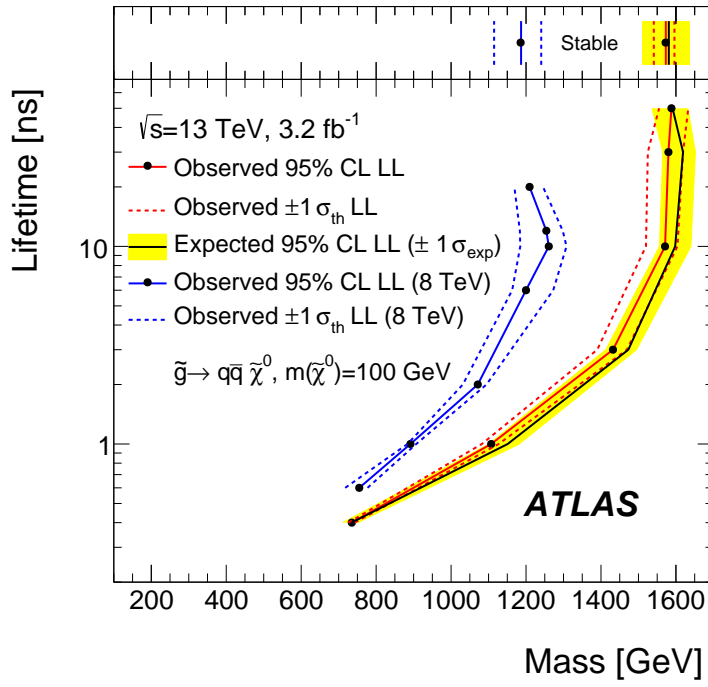


Figure 74: The excluded range of masses as a function of gluino lifetime. The expected lower limit (LL), with its experimental  $\pm 1\sigma$  band, is given with respect to the nominal theoretical cross-section. The observed 95% LL obtained at  $\sqrt{s} = 8 \text{ TeV}$  [61] is also shown for comparison.

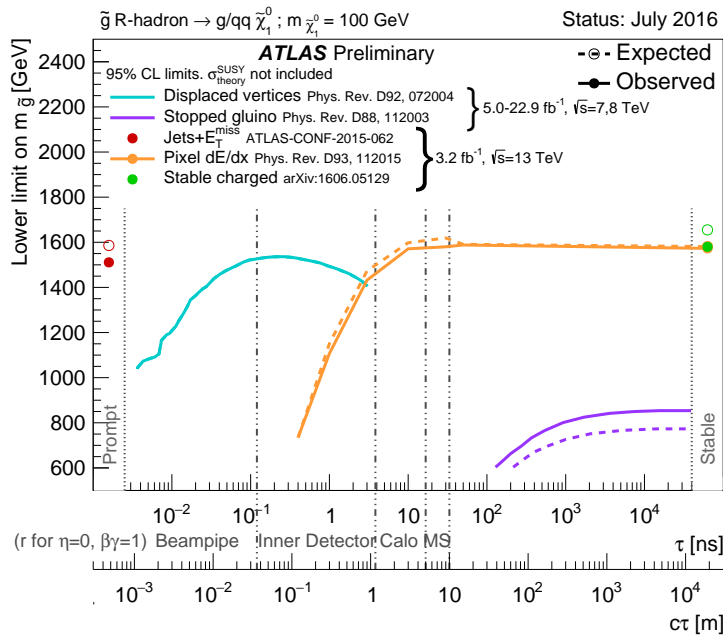


Figure 75: The constraints on the gluino mass as a function of lifetime for a split-supersymmetry model with the gluino R-Hadrons decaying into a gluon or light quarks and a neutralino with mass of 100 GeV. The solid lines indicate the observed limits, while the dashed lines indicate the expected limits. The area below the curves is excluded. The dots represent results for which the particle is assumed to be prompt or stable.



2378

## PART VI

2379

### CONCLUSIONS

2380

You can put some informational part preamble text here.



# 14

2381

## 2382 SUMMARY AND OUTLOOK

---

### 2383 14.1 SUMMARY

### 2384 14.2 OUTLOOK



2385

## PART VII

2386

## APPENDIX

2387



# A

2388

2389 INELASTIC CROSS SECTION

---



# B

2390

<sup>2391</sup> EXPANDED R-HADRON YIELDS AND LIMITS

---

$m(\tilde{g})$ [GeV]	Left Extremum [GeV]	Right Extremum [GeV]
1000	682	1387
1100	763	1478
1200	801	1606
1300	809	1841
1400	861	2011
1500	920	2032
1600	952	2173
1800	1017	2422

Table 14: The left and right extremum of the mass window for each generated mass point with a 50 ns lifetime.

$m(\tilde{g})$ [GeV]	Left Extremum [GeV]	Right Extremum [GeV]
1000	689	1321
1100	746	1513
1200	788	1670
1300	860	1734
1400	833	1925
1500	852	2048
1600	833	2283
1700	946	2379
1800	869	2505

Table 15: The left and right extremum of the mass window for each generated mass point with a 30 ns lifetime.

$m(\tilde{g})$ [GeV]	Left Extremum [GeV]	Right Extremum [GeV]
1000	655	1349
1100	734	1455
1200	712	1631
1300	792	1737
1400	717	1926
1500	815	2117
1600	824	2122
1700	900	2274
1800	919	2344

Table 16: The left and right extremum of the mass window for each generated mass point with a 10 ns lifetime.

$m(\tilde{g})$ [GeV]	Left Extremum [GeV]	Right Extremum [GeV]
800	531	1065
900	576	1165
1000	610	1345
1100	635	1432
1200	663	1563
1300	620	1667
1400	742	1727
1500	761	1937
1600	573	2000
1700	621	2182

Table 17: The left and right extremum of the mass window used for each generated mass point with a lifetime of 3 ns.

$m(\tilde{g})$ [GeV]	Left Extremum [GeV]	Right Extremum [GeV]
600	411	758
700	385	876
800	486	970
900	406	987
1000	408	1136
1100	555	1196
1200	516	1378

Table 18: The left and right extremum of the mass window used for each mass point with a lifetime of 1 ns.

$m(\tilde{g})$ [GeV]	Left Extremum [GeV]	Right Extremum [GeV]
400	204	510
500	295	639
600	288	702
700	323	701
800	190	771
900	277	677
1000	249	688

Table 19: The left and right extremum of the mass window for each generated mass point with a lifetime of 0.4 ns.

$m(\tilde{g})$ [GeV]	Left Extremum [GeV]	Right Extremum [GeV]
800	627	1053
1000	726	1277
1200	857	1584
1400	924	1937
1600	993	2308
1800	1004	2554

Table 20: The left and right extremum of the mass window used for each generated stable mass point.

$m(\tilde{g})$ [GeV]	Expected Signal	Expected Background	Observed Data
1000	$131.18 \pm 6.35$	$1.803 \pm 0.081$	$1.0 \pm 1.0$
1100	$71.11 \pm 3.35$	$1.409 \pm 0.069$	$1.0 \pm 1.0$
1200	$37.18 \pm 1.75$	$1.310 \pm 0.066$	$1.0 \pm 1.0$
1300	$20.76 \pm 0.95$	$1.431 \pm 0.069$	$1.0 \pm 1.0$
1400	$12.63 \pm 0.57$	$1.273 \pm 0.065$	$1.0 \pm 1.0$
1500	$6.57 \pm 0.29$	$1.115 \pm 0.059$	$1.0 \pm 1.0$
1600	$3.56 \pm 0.16$	$1.041 \pm 0.057$	$1.0 \pm 1.0$
1800	$1.27 \pm 0.05$	$0.918 \pm 0.053$	$1.0 \pm 1.0$

Table 21: The expected number of signal events, the expected number of background events, and the observed number of events in data with their respective statistical errors within the respective mass window for each generated mass point with a lifetime of 50 ns.

$m(\tilde{g})$ [GeV]	Expected Signal	Expected Background	Observed Data
1000	$144.65 \pm 6.34$	$1.328 \pm 0.063$	$2.0 \pm 1.4$
1100	$75.28 \pm 3.27$	$1.255 \pm 0.060$	$2.0 \pm 1.4$
1200	$40.51 \pm 1.75$	$1.193 \pm 0.058$	$2.0 \pm 1.4$
1300	$20.91 \pm 0.93$	$0.997 \pm 0.051$	$2.0 \pm 1.4$
1400	$11.97 \pm 0.51$	$1.131 \pm 0.056$	$2.0 \pm 1.4$
1500	$6.81 \pm 0.28$	$1.111 \pm 0.055$	$2.0 \pm 1.4$
1600	$4.19 \pm 0.16$	$1.193 \pm 0.058$	$2.0 \pm 1.4$
1700	$2.42 \pm 0.09$	$0.963 \pm 0.050$	$2.0 \pm 1.4$
1800	$1.46 \pm 0.05$	$1.138 \pm 0.056$	$3.0 \pm 1.7$

Table 22: The expected number of signal events, the expected number of background events, and the observed number of events in data with their respective statistical errors within the respective mass window for each generated mass point with a lifetime of 30 ns.

$m(\tilde{g})$ [GeV]	Expected Signal	Expected Background	Observed Data
1000	$144.48 \pm 5.14$	$1.499 \pm 0.069$	$2.0 \pm 1.4$
1100	$73.19 \pm 2.61$	$1.260 \pm 0.060$	$2.0 \pm 1.4$
1200	$41.54 \pm 1.41$	$1.456 \pm 0.067$	$2.0 \pm 1.4$
1300	$22.58 \pm 0.77$	$1.201 \pm 0.058$	$2.0 \pm 1.4$
1400	$12.70 \pm 0.42$	$1.558 \pm 0.071$	$2.0 \pm 1.4$
1500	$6.73 \pm 0.24$	$1.237 \pm 0.060$	$2.0 \pm 1.4$
1600	$3.90 \pm 0.13$	$1.201 \pm 0.058$	$2.0 \pm 1.4$
1700	$2.27 \pm 0.07$	$1.027 \pm 0.052$	$2.0 \pm 1.4$
1800	$1.34 \pm 0.04$	$1.019 \pm 0.052$	$2.0 \pm 1.4$

Table 23: The expected number of signal events, the expected number of background events, and the observed number of events in data with their respective statistical errors within the respective mass window for each generated mass point with a lifetime of 10 ns.

$m(\tilde{g})$ [GeV]	Expected Signal	Expected Background	Observed Data
800	$362.97 \pm 14.68$	$1.841 \pm 0.080$	$5.0 \pm 2.2$
900	$169.20 \pm 6.69$	$1.710 \pm 0.076$	$3.0 \pm 1.7$
1000	$84.78 \pm 3.23$	$1.727 \pm 0.076$	$2.0 \pm 1.4$
1100	$40.06 \pm 1.60$	$1.679 \pm 0.075$	$2.0 \pm 1.4$
1200	$20.06 \pm 0.81$	$1.598 \pm 0.072$	$2.0 \pm 1.4$
1300	$10.76 \pm 0.43$	$1.851 \pm 0.080$	$2.0 \pm 1.4$
1400	$5.52 \pm 0.22$	$1.374 \pm 0.064$	$2.0 \pm 1.4$
1500	$3.16 \pm 0.13$	$1.355 \pm 0.064$	$2.0 \pm 1.4$
1600	$2.13 \pm 0.11$	$2.235 \pm 0.093$	$3.0 \pm 1.7$
1700	$1.10 \pm 0.06$	$1.995 \pm 0.085$	$2.0 \pm 1.4$

Table 24: The expected number of signal events, the expected number of background events, and the observed number of events in data with their respective statistical errors within the respective mass window for each generated mass point with a lifetime of 3 ns.

$m(\tilde{g})$ [GeV]	Expected Signal	Expected Background	Observed Data
600	$431.80 \pm 36.60$	$2.418 \pm 0.099$	$3.0 \pm 1.7$
700	$192.77 \pm 15.28$	$3.267 \pm 0.126$	$3.0 \pm 1.7$
800	$69.63 \pm 5.90$	$2.125 \pm 0.089$	$3.0 \pm 1.7$
900	$28.91 \pm 2.59$	$3.114 \pm 0.121$	$3.0 \pm 1.7$
1000	$13.64 \pm 1.22$	$3.359 \pm 0.129$	$5.0 \pm 2.2$
1100	$6.13 \pm 0.57$	$1.879 \pm 0.081$	$3.0 \pm 1.7$
1200	$3.24 \pm 0.30$	$2.387 \pm 0.098$	$5.0 \pm 2.2$

Table 25: The expected number of signal events, the expected number of background events, and the observed number of events in data with their respective statistical errors within the respective mass window for each generated mass point with a lifetime of 1 ns.

$m(\tilde{g})$ [GeV]	Expected Signal	Expected Background	Observed Data
400	$181.71 \pm 75.59$	$6.780 \pm 0.238$	$4.0 \pm 2.0$
500	$103.88 \pm 30.05$	$4.310 \pm 0.160$	$4.0 \pm 2.0$
600	$28.34 \pm 9.34$	$4.868 \pm 0.177$	$4.0 \pm 2.0$
700	$13.62 \pm 4.00$	$3.908 \pm 0.147$	$4.0 \pm 2.0$
800	$2.75 \pm 1.15$	$9.001 \pm 0.308$	$8.0 \pm 2.8$
900	$2.25 \pm 0.71$	$5.045 \pm 0.183$	$5.0 \pm 2.2$
1000	$0.34 \pm 0.19$	$6.026 \pm 0.214$	$6.0 \pm 2.4$

Table 26: The expected number of signal events, the expected number of background events, and the observed number of events in data with their respective statistical errors within the respective mass window for each generated mass point with a lifetime of p4 ns.

$m(\tilde{g})$ [GeV]	Expected Signal	Expected Background	Observed Data
800	$462.83 \pm 14.86$	$1.764 \pm 0.080$	$2.0 \pm 1.4$
1000	$108.73 \pm 3.38$	$1.458 \pm 0.070$	$1.0 \pm 1.0$
1200	$31.74 \pm 0.95$	$1.137 \pm 0.060$	$1.0 \pm 1.0$
1400	$10.22 \pm 0.29$	$1.058 \pm 0.058$	$1.0 \pm 1.0$
1600	$3.07 \pm 0.09$	$0.947 \pm 0.054$	$1.0 \pm 1.0$
1800	$1.08 \pm 0.05$	$0.940 \pm 0.054$	$1.0 \pm 1.0$

Table 27: The expected number of signal events, the expected number of background events, and the observed number of events in data with their respective statistical errors within the respective mass window for each generated stable mass point

2392 BIBLIOGRAPHY

---

- 2393 [1] Lyndon Evans and Philip Bryant. "LHC Machine". In: *JINST* 3 (2008), S08001.  
2394 doi: [10.1088/1748-0221/3/08/S08001](https://doi.org/10.1088/1748-0221/3/08/S08001).
- 2395 [2] C Lefevre. "LHC: the guide (English version). Guide du LHC (version anglaise)".  
2396 2009. URL: <https://cds.cern.ch/record/1165534>.
- 2397 [3] ATLAS Collaboration. "The ATLAS Experiment at the CERN Large Hadron  
2398 Collider". In: *JINST* 3 (2008), S08003. doi: [10.1088/1748-0221/3/08/S08003](https://doi.org/10.1088/1748-0221/3/08/S08003).
- 2400 [4] S. Chatrchyan et al. "The CMS experiment at the CERN LHC". In: *JINST*  
2401 3 (2008), S08004. doi: [10.1088/1748-0221/3/08/S08004](https://doi.org/10.1088/1748-0221/3/08/S08004).
- 2402 [5] A. Augusto Alves Jr. et al. "The LHCb Detector at the LHC". In: *JINST* 3  
2403 (2008), S08005. doi: [10.1088/1748-0221/3/08/S08005](https://doi.org/10.1088/1748-0221/3/08/S08005).
- 2404 [6] K. Aamodt et al. "The ALICE experiment at the CERN LHC". In: *JINST* 3  
2405 (2008), S08002. doi: [10.1088/1748-0221/3/08/S08002](https://doi.org/10.1088/1748-0221/3/08/S08002).
- 2406 [7] K. A. Olive et al. "Review of Particle Physics". In: *Chin. Phys. C* 38 (2014),  
2407 p. 090001. doi: [10.1088/1674-1137/38/9/090001](https://doi.org/10.1088/1674-1137/38/9/090001).
- 2408 [8] S. Agostinelli et al. "GEANT4: A simulation toolkit". In: *Nucl. Instrum. Meth.*  
2409 A 506 (2003), pp. 250–303. doi: [10.1016/S0168-9002\(03\)01368-8](https://doi.org/10.1016/S0168-9002(03)01368-8).
- 2410 [9] ATLAS Collaboration. "A study of the material in the ATLAS inner de-  
2411 tector using secondary hadronic interactions". In: *JINST* 7 (2012), P01013.  
2412 doi: [10.1088/1748-0221/7/01/P01013](https://doi.org/10.1088/1748-0221/7/01/P01013). arXiv: [1110.6191 \[hep-ex\]](https://arxiv.org/abs/1110.6191).  
2413 PERF-2011-08.
- 2414 [10] ATLAS Collaboration. "Electron and photon energy calibration with the  
2415 ATLAS detector using LHC Run 1 data". In: *Eur. Phys. J. C* 74 (2014), p. 3071.  
2416 doi: [10.1140/epjc/s10052-014-3071-4](https://doi.org/10.1140/epjc/s10052-014-3071-4). arXiv: [1407.5063](https://arxiv.org/abs/1407.5063)  
2417 [hep-ex]. PERF-2013-05.
- 2418 [11] ATLAS Collaboration. "A measurement of the calorimeter response to sin-  
2419 ggle hadrons and determination of the jet energy scale uncertainty using  
2420 LHC Run-1  $pp$ -collision data with the ATLAS detector". In: (2016). arXiv:  
2421 [1607.08842 \[hep-ex\]](https://arxiv.org/abs/1607.08842). PERF-2015-05.
- 2422 [12] ATLAS Collaboration. "Single hadron response measurement and calorime-  
2423 ter jet energy scale uncertainty with the ATLAS detector at the LHC". In:  
2424 *Eur. Phys. J. C* 73 (2013), p. 2305. doi: [10.1140/epjc/s10052-013-2305-1](https://doi.org/10.1140/epjc/s10052-013-2305-1). arXiv: [1203.1302 \[hep-ex\]](https://arxiv.org/abs/1203.1302). PERF-2011-05.
- 2426 [13] ATLAS Collaboration. "The ATLAS Simulation Infrastructure". In: *Eur.*  
2427 *Phys. J. C* 70 (2010), p. 823. doi: [10.1140/epjc/s10052-010-1429-9](https://doi.org/10.1140/epjc/s10052-010-1429-9).  
2428 arXiv: [1005.4568 \[hep-ex\]](https://arxiv.org/abs/1005.4568). SOFT-2010-01.

- [14] T. Sjöstrand, S. Mrenna, and P. Skands. “A Brief Introduction to PYTHIA 8.1”. In: *Comput. Phys. Commun.* 178 (2008), pp. 852–867. doi: [10.1016/j.cpc.2008.01.036](https://doi.org/10.1016/j.cpc.2008.01.036). arXiv: [0710.3820](https://arxiv.org/abs/0710.3820).
- [15] ATLAS Collaboration. *Summary of ATLAS Pythia 8 tunes*. ATL-PHYS-PUB-2012-003. 2012. URL: <http://cds.cern.ch/record/1474107>.
- [16] A.D. Martin, W.J. Stirling, R.S. Thorne, and G. Watt. “Parton distributions for the LHC”. In: *Eur. Phys. J. C* 63 (2009). Figures from the MSTW Website, pp. 189–285. doi: [10.1140/epjc/s10052-009-1072-5](https://doi.org/10.1140/epjc/s10052-009-1072-5). arXiv: [0901.0002](https://arxiv.org/abs/0901.0002).
- [17] A. Sherstnev and R.S. Thorne. “Parton Distributions for LO Generators”. In: *Eur. Phys. J. C* 55 (2008), pp. 553–575. doi: [10.1140/epjc/s10052-008-0610-x](https://doi.org/10.1140/epjc/s10052-008-0610-x). arXiv: [0711.2473](https://arxiv.org/abs/0711.2473).
- [18] A. Ribon et al. *Status of Geant4 hadronic physics for the simulation of LHC experiments at the start of LHC physics program*. CERN-LCGAPP-2010-02. 2010. URL: <http://lcgapp.cern.ch/project/docs/noteStatusHadronic2010.pdf>.
- [19] M. P. Guthrie, R. G. Alsmiller, and H. W. Bertini. “Calculation of the capture of negative pions in light elements and comparison with experiments pertaining to cancer radiotherapy”. In: *Nucl. Instrum. Meth.* 66 (1968), pp. 29–36. doi: [10.1016/0029-554X\(68\)90054-2](https://doi.org/10.1016/0029-554X(68)90054-2).
- [20] H. W. Bertini and P. Guthrie. “News item results from medium-energy intranuclear-cascade calculation”. In: *Nucl. Instr. and Meth. A* 169 (1971), p. 670. doi: [10.1016/0375-9474\(71\)90710-X](https://doi.org/10.1016/0375-9474(71)90710-X).
- [21] V.A. Karmanov. “Light Front Wave Function of Relativistic Composite System in Explicitly Solvable Model”. In: *Nucl. Phys. B* 166 (1980), p. 378. doi: [10.1016/0550-3213\(80\)90204-7](https://doi.org/10.1016/0550-3213(80)90204-7).
- [22] H. S. Fesefeldt. *GHEISHA program*. Pitha-85-02, Aachen. 1985.
- [23] G. Folger and J.P. Wellisch. “String parton models in Geant4”. In: (2003). arXiv: [nucl-th/0306007](https://arxiv.org/abs/nucl-th/0306007).
- [24] N. S. Amelin et al. “Transverse flow and collectivity in ultrarelativistic heavy-ion collisions”. In: *Phys. Rev. Lett.* 67 (1991), p. 1523. doi: [10.1103/PhysRevLett.67.1523](https://doi.org/10.1103/PhysRevLett.67.1523).
- [25] N. S. Amelin et al. “Collectivity in ultrarelativistic heavy ion collisions”. In: *Nucl. Phys. A* 544 (1992), p. 463. doi: [10.1016/0375-9474\(92\)90598-E](https://doi.org/10.1016/0375-9474(92)90598-E).
- [26] L. V. Bravina et al. “Fluid dynamics and Quark Gluon string model - What we can expect for Au+Au collisions at 11.6 AGeV/c”. In: *Nucl. Phys. A* 566 (1994), p. 461. doi: [10.1016/0375-9474\(94\)90669-6](https://doi.org/10.1016/0375-9474(94)90669-6).
- [27] L. V. Bravin et al. “Scaling violation of transverse flow in heavy ion collisions at AGS energies”. In: *Phys. Lett. B* 344 (1995), p. 49. doi: [10.1016/0370-2693\(94\)01560-Y](https://doi.org/10.1016/0370-2693(94)01560-Y).

- [28] B. Andersson et al. “A model for low-pT hadronic reactions with generalizations to hadron-nucleus and nucleus-nucleus collisions”. In: *Nucl. Phys. B* 281 (1987), p. 289. doi: [10.1016/0550-3213\(87\)90257-4](https://doi.org/10.1016/0550-3213(87)90257-4).
- [29] B. Andersson, A. Tai, and B.-H. Sa. “Final state interactions in the (nuclear) FRITIOF string interaction scenario”. In: *Z. Phys. C* 70 (1996), pp. 499–506. doi: [10.1007/s002880050127](https://doi.org/10.1007/s002880050127).
- [30] B. Nilsson-Almqvist and E. Stenlund. “Interactions Between Hadrons and Nuclei: The Lund Monte Carlo, Fritiof Version 1.6”. In: *Comput. Phys. Commun.* 43 (1987), p. 387. doi: [10.1016/0010-4655\(87\)90056-7](https://doi.org/10.1016/0010-4655(87)90056-7).
- [31] B. Ganhuyag and V. Uzhinsky. “Modified FRITIOF code: Negative charged particle production in high energy nucleus nucleus interactions”. In: *Czech. J. Phys.* 47 (1997), pp. 913–918. doi: [10.1023/A:1021296114786](https://doi.org/10.1023/A:1021296114786).
- [32] ATLAS Collaboration. “Topological cell clustering in the ATLAS calorimeters and its performance in LHC Run 1”. In: (2016). arXiv: [1603.02934 \[hep-ex\]](https://arxiv.org/abs/1603.02934).
- [33] Peter Speckmayer. “Energy Measurement of Hadrons with the CERN ATLAS Calorimeter”. Presented on 18 Jun 2008. PhD thesis. Vienna: Vienna, Tech. U., 2008. url: <http://cds.cern.ch/record/1112036>.
- [34] CMS Collaboration. “The CMS barrel calorimeter response to particle beams from 2 to 350 GeV/c”. In: *Eur. Phys. J. C* 60.3 (2009). doi: [10.1140/epjc/s10052-009-0959-5](https://doi.org/10.1140/epjc/s10052-009-0959-5).
- [35] J. Beringer et al. (Particle Data Group). “Review of Particle Physics”. In: *Chin. Phys. C* 38 (2014), p. 090001. url: <http://pdg.lbl.gov>.
- [36] P. Adragna et al. “Measurement of Pion and Proton Response and Longitudinal Shower Profiles up to 20 Nuclear Interaction Lengths with the ATLAS Tile Calorimeter”. In: *Nucl. Instrum. Meth. A* 615 (2010), pp. 158–181. doi: [10.1016/j.nima.2010.01.037](https://doi.org/10.1016/j.nima.2010.01.037).
- [37] ATLAS Collaboration. “Jet energy measurement and its systematic uncertainty in proton–proton collisions at  $\sqrt{s} = 7$  TeV with the ATLAS detector”. In: *Eur. Phys. J. C* 75 (2015), p. 17. doi: [10.1140/epjc/s10052-014-3190-y](https://doi.org/10.1140/epjc/s10052-014-3190-y). arXiv: [1406.0076 \[hep-ex\]](https://arxiv.org/abs/1406.0076). PERF-2012-01.
- [38] Hung-Liang Lai, Marco Guzzi, Joey Huston, Zhao Li, Pavel M. Nadolsky, et al. “New parton distributions for collider physics”. In: *Phys. Rev. D* 82 (2010), p. 074024. doi: [10.1103/PhysRevD.82.074024](https://doi.org/10.1103/PhysRevD.82.074024). arXiv: [1007.2241 \[hep-ph\]](https://arxiv.org/abs/1007.2241).
- [39] E. Abat et al. “Study of energy response and resolution of the ATLAS barrel calorimeter to hadrons of energies from 20 to 350 GeV”. In: *Nucl. Instrum. Meth. A* 621.1-3 (2010), pp. 134 –150. doi: <http://dx.doi.org/10.1016/j.nima.2010.04.054>.
- [40] ATLAS Collaboration. “Jet energy measurement with the ATLAS detector in proton–proton collisions at  $\sqrt{s} = 7$  TeV”. In: *Eur. Phys. J. C* 73 (2013), p. 2304. doi: [10.1140/epjc/s10052-013-2304-2](https://doi.org/10.1140/epjc/s10052-013-2304-2). arXiv: [1112.6426 \[hep-ex\]](https://arxiv.org/abs/1112.6426). PERF-2011-03.

- 2513 [41] Nausheen R. Shah and Carlos E. M. Wagner. “Gravitons and dark matter in  
 2514 universal extra dimensions”. In: *Phys. Rev.* D74 (2006), p. 104008. doi: [10.1103/PhysRevD.74.104008](https://doi.org/10.1103/PhysRevD.74.104008). arXiv: [hep-ph/0608140](https://arxiv.org/abs/hep-ph/0608140) [hep-ph].
- 2515
- 2516 [42] Jonathan L. Feng, Arvind Rajaraman, and Fumihiro Takayama. “Graviton  
 2517 cosmology in universal extra dimensions”. In: *Phys. Rev.* D68 (2003), p. 085018.  
 2518 doi: [10.1103/PhysRevD.68.085018](https://doi.org/10.1103/PhysRevD.68.085018). arXiv: [hep-ph/0307375](https://arxiv.org/abs/hep-ph/0307375)  
 2519 [hep-ph].
- 2520 [43] Paul H. Frampton and Pham Quang Hung. “Long-lived quarks?” In: *Phys.*  
 2521 *Rev. D* 58 (5 1998), p. 057704. doi: [10.1103/PhysRevD.58.057704](https://doi.org/10.1103/PhysRevD.58.057704).  
 2522 URL: <http://link.aps.org/doi/10.1103/PhysRevD.58.057704>.
- 2523
- 2524 [44] C. Friberg, E. Norrbin, and T. Sjostrand. “QCD aspects of leptoquark pro-  
 2525 duction at HERA”. In: *Phys. Lett.* B403 (1997), pp. 329–334. doi: [10.1016/S0370-2693\(97\)00543-1](https://doi.org/10.1016/S0370-2693(97)00543-1). arXiv: [hep-ph/9704214](https://arxiv.org/abs/hep-ph/9704214) [hep-ph].
- 2526
- 2527 [45] Herbert K. Dreiner. “An introduction to explicit R-parity violation”. In:  
 2528 (1997). arXiv: [hep-ph/9707435](https://arxiv.org/abs/hep-ph/9707435).
- 2529 [46] Edmond L. Berger and Zack Sullivan. “Lower limits on R-parity-violating  
 2530 couplings in supersymmetry”. In: *Phys. Rev. Lett.* 92 (2004), p. 201801. doi:  
 2531 [10.1103/PhysRevLett.92.201801](https://doi.org/10.1103/PhysRevLett.92.201801). arXiv: [hep-ph/0310001](https://arxiv.org/abs/hep-ph/0310001).
- 2532 [47] R. Barbieri, C. Berat, M. Besancon, M. Chemtob, A. Deandrea, et al. “R-  
 2533 parity violating supersymmetry”. In: *Phys. Rept.* 420 (2005), p. 1. doi: [10.1016/j.physrep.2005.08.006](https://doi.org/10.1016/j.physrep.2005.08.006). arXiv: [hep-ph/0406039](https://arxiv.org/abs/hep-ph/0406039).
- 2534
- 2535 [48] M. Fairbairn et al. “Stable massive particles at colliders”. In: *Phys. Rept.* 438  
 2536 (2007), p. 1. doi: [10.1016/j.physrep.2006.10.002](https://doi.org/10.1016/j.physrep.2006.10.002). arXiv: [hep-ph/0611040](https://arxiv.org/abs/hep-ph/0611040).
- 2537
- 2538 [49] Christopher F. Kolda. “Gauge-mediated supersymmetry breaking: Intro-  
 2539 duction, review and update”. In: *Nucl. Phys. Proc. Suppl.* 62 (1998), p. 266.  
 2540 doi: [10.1016/S0920-5632\(97\)00667-1](https://doi.org/10.1016/S0920-5632(97)00667-1). arXiv: [hep-ph/9707450](https://arxiv.org/abs/hep-ph/9707450).
- 2541 [50] Howard Baer, Kingman Cheung, and John F. Gunion. “A Heavy gluino as  
 2542 the lightest supersymmetric particle”. In: *Phys. Rev. D* 59 (1999), p. 075002.  
 2543 doi: [10.1103/PhysRevD.59.075002](https://doi.org/10.1103/PhysRevD.59.075002). arXiv: [hep-ph/9806361](https://arxiv.org/abs/hep-ph/9806361).
- 2544 [51] S. James Gates Jr. and Oleg Lebedev. “Searching for supersymmetry in  
 2545 hadrons”. In: *Phys. Lett. B* 477 (2000), p. 216. doi: [10.1016/S0370-2693\(00\)00172-6](https://doi.org/10.1016/S0370-2693(00)00172-6). arXiv: [hep-ph/9912362](https://arxiv.org/abs/hep-ph/9912362).
- 2546
- 2547 [52] G. F. Giudice and A. Romanino. “Split supersymmetry”. In: *Nucl. Phys. B*  
 2548 699 (2004), p. 65. doi: [10.1016/j.nuclphysb.2004.11.048](https://doi.org/10.1016/j.nuclphysb.2004.11.048). arXiv:  
 2549 [hep-ph/0406088](https://arxiv.org/abs/hep-ph/0406088).
- 2550 [53] N. Arkani-Hamed, S. Dimopoulos, G. F. Giudice, and A. Romanino. “As-  
 2551 pects of split supersymmetry”. In: *Nucl. Phys. B* 709 (2005), p. 3. doi: [10.1016/j.nuclphysb.2004.12.026](https://doi.org/10.1016/j.nuclphysb.2004.12.026). arXiv: [hep-ph/0409232](https://arxiv.org/abs/hep-ph/0409232).
- 2552

- 2553 [54] Glennys R. Farrar and Pierre Fayet. "Phenomenology of the Production,  
 2554 Decay, and Detection of New Hadronic States Associated with Supersym-  
 2555 metry". In: *Phys. Lett.* B76 (1978), pp. 575–579. doi: [10.1016/0370-2693\(78\)90858-4](https://doi.org/10.1016/0370-2693(78)90858-4).
- 2557 [55] A. C. Kraan, J. B. Hansen, and P. Nevski. "Discovery potential of R-hadrons  
 2558 with the ATLAS detector". In: *Eur. Phys. J.* C49 (2007), pp. 623–640. doi:  
 2559 [10.1140/epjc/s10052-006-0162-x](https://doi.org/10.1140/epjc/s10052-006-0162-x). arXiv: [hep-ex/0511014](https://arxiv.org/abs/hep-ex/0511014)  
 2560 [[hep-ex](#)].
- 2561 [56] Rasmus Mckeprang and David Milstead. "An Updated Description of  
 2562 Heavy-Hadron Interactions in GEANT-4". In: *Eur. Phys. J.* C66 (2010), pp. 493–  
 2563 501. doi: [10.1140/epjc/s10052-010-1262-1](https://doi.org/10.1140/epjc/s10052-010-1262-1). arXiv: [0908.1868](https://arxiv.org/abs/0908.1868)  
 2564 [[hep-ph](#)].
- 2565 [57] ATLAS Collaboration. "Search for massive, long-lived particles using mul-  
 2566 titrack displaced vertices or displaced lepton pairs in  $pp$  collisions at  $\sqrt{s} =$   
 2567 8 TeV with the ATLAS detector". In: *Phys. Rev. D* 92 (2015), p. 072004.  
 2568 doi: [10.1103/PhysRevD.92.072004](https://doi.org/10.1103/PhysRevD.92.072004). arXiv: [1504.05162](https://arxiv.org/abs/1504.05162) [[hep-ex](#)].  
 2569 SUSY-2014-02.
- 2570 [58] ATLAS Collaboration. "Search for charginos nearly mass degenerate with  
 2571 the lightest neutralino based on a disappearing-track signature in  $pp$  col-  
 2572 lisions at  $\sqrt{s} = 8$  TeV with the ATLAS detector". In: *Phys. Rev. D* 88 (2013),  
 2573 p. 112006. doi: [10.1103/PhysRevD.88.112006](https://doi.org/10.1103/PhysRevD.88.112006). arXiv: [1310.3675](https://arxiv.org/abs/1310.3675)  
 2574 [[hep-ex](#)]. SUSY-2013-01.
- 2575 [59] ATLAS Collaboration. "Searches for heavy long-lived sleptons and R-Hadrons  
 2576 with the ATLAS detector in  $pp$  collisions at  $\sqrt{s} = 7$  TeV". In: *Phys. Lett. B*  
 2577 720 (2013), p. 277. doi: [10.1016/j.physletb.2013.02.015](https://doi.org/10.1016/j.physletb.2013.02.015). arXiv:  
 2578 [1211.1597](https://arxiv.org/abs/1211.1597) [[hep-ex](#)]. SUSY-2012-01.
- 2579 [60] ATLAS Collaboration. "Searches for heavy long-lived charged particles  
 2580 with the ATLAS detector in proton–proton collisions at  $\sqrt{s} = 8$  TeV".  
 2581 In: *JHEP* 01 (2015), p. 068. doi: [10.1007/JHEP01\(2015\)068](https://doi.org/10.1007/JHEP01(2015)068). arXiv:  
 2582 [1411.6795](https://arxiv.org/abs/1411.6795) [[hep-ex](#)]. SUSY-2013-22.
- 2583 [61] ATLAS Collaboration. "Search for metastable heavy charged particles with  
 2584 large ionisation energy loss in  $pp$  collisions at  $\sqrt{s} = 8$  TeV using the AT-  
 2585 LAS experiment". In: *Eur. Phys. J.* C 75 (2015), p. 407. doi: [10.1140/epjc/s10052-015-3609-0](https://doi.org/10.1140/epjc/s10052-015-3609-0). arXiv: [1506.05332](https://arxiv.org/abs/1506.05332) [[hep-ex](#)]. SUSY-  
 2586 2014-09.
- 2588 [62] ATLAS Collaboration. "Search for heavy long-lived charged  $R$ -hadrons  
 2589 with the ATLAS detector in  $3.2 \text{ fb}^{-1}$  of proton–proton collision data at  
 2590  $\sqrt{s} = 13$  TeV". In: *Phys. Lett.* B760 (2016), pp. 647–665. doi: [10.1016/j.physletb.2016.07.042](https://doi.org/10.1016/j.physletb.2016.07.042). arXiv: [1606.05129](https://arxiv.org/abs/1606.05129) [[hep-ex](#)].  
 2591
- 2592 [63] Torbjorn Sjöstrand, Stephen Mrenna, and Peter Skands. "PYTHIA 6.4 Physics  
 2593 and Manual". In: *JHEP* 0605 (2006), p. 026. doi: [10.1088/1126-6708/2006/05/026](https://doi.org/10.1088/1126-6708/2006/05/026). arXiv: [hep-ph/0603175](https://arxiv.org/abs/hep-ph/0603175).  
 2594

- 2595 [64] *Further ATLAS tunes of PYTHIA6 and Pythia 8*. Tech. rep. ATL-PHYS-PUB-  
 2596 2011-014. Geneva: CERN, 2011. url: <https://cds.cern.ch/record/1400677>.
- 2598 [65] Aafke Christine Kraan. “Interactions of heavy stable hadronizing parti-  
 2599 cles”. In: *Eur. Phys. J.* C37 (2004), pp. 91–104. doi: [10.1140/epjc/s2004-01946-6](https://doi.org/10.1140/epjc/s2004-01946-6). arXiv: [hep-ex/0404001](https://arxiv.org/abs/hep-ex/0404001) [hep-ex].
- 2601 [66] M. Fairbairn et al. “Stable massive particles at colliders”. In: *Phys. Rept.* 438  
 2602 (2007), p. 1. doi: [10.1016/j.physrep.2006.10.002](https://doi.org/10.1016/j.physrep.2006.10.002). arXiv: [hep-ph/0611040](https://arxiv.org/abs/hep-ph/0611040).
- 2604 [67] W. Beenakker, R. Hopker, M. Spira, and P. M. Zerwas. “Squark and gluino  
 2605 production at hadron colliders”. In: *Nucl. Phys. B* 492 (1997), p. 51. doi:  
 2606 [10.1016/S0550-3213\(97\)00084-9](https://doi.org/10.1016/S0550-3213(97)00084-9). arXiv: [hep-ph/9610490](https://arxiv.org/abs/hep-ph/9610490).
- 2607 [68] A. Kulesza and L. Motyka. “Threshold resummation for squark-antisquark  
 2608 and gluino-pair production at the LHC”. In: *Phys. Rev. Lett.* 102 (2009),  
 2609 p. 111802. doi: [10.1103/PhysRevLett.102.111802](https://doi.org/10.1103/PhysRevLett.102.111802). arXiv: [0807.2405](https://arxiv.org/abs/0807.2405) [hep-ph].
- 2611 [69] A. Kulesza and L. Motyka. “Soft gluon resummation for the production  
 2612 of gluino-gluino and squark-antisquark pairs at the LHC”. In: *Phys. Rev.*  
 2613 D 80 (2009), p. 095004. doi: [10.1103/PhysRevD.80.095004](https://doi.org/10.1103/PhysRevD.80.095004). arXiv:  
 2614 [0905.4749](https://arxiv.org/abs/0905.4749) [hep-ph].
- 2615 [70] Wim Beenakker, Silja Brensing, Michael Kramer, Anna Kulesza, Eric Lae-  
 2616 nen, et al. “Soft-gluon resummation for squark and gluino hadroproduc-  
 2617 tion”. In: *JHEP* 0912 (2009), p. 041. doi: [10.1088/1126-6708/2009/12/041](https://doi.org/10.1088/1126-6708/2009/12/041). arXiv: [0909.4418](https://arxiv.org/abs/0909.4418) [hep-ph].
- 2619 [71] W. Beenakker, S. Brensing, M.n Kramer, A. Kulesza, E. Laenen, et al. “Squark  
 2620 and Gluino Hadroproduction”. In: *Int. J. Mod. Phys. A* 26 (2011), p. 2637.  
 2621 doi: [10.1142/S0217751X11053560](https://doi.org/10.1142/S0217751X11053560). arXiv: [1105.1110](https://arxiv.org/abs/1105.1110) [hep-ph].
- 2622 [72] Michael Krämer et al. *Supersymmetry production cross sections in pp collisions*  
 2623 at  $\sqrt{s} = 7 \text{ TeV}$ . 2012. arXiv: [1206.2892](https://arxiv.org/abs/1206.2892) [hep-ph].
- 2624 [73] Rasmus Mackeprang and Andrea Rizzi. “Interactions of Coloured Heavy  
 2625 Stable Particles in Matter”. In: *Eur. Phys. J.* C50 (2007), pp. 353–362. doi:  
 2626 [10.1140/epjc/s10052-007-0252-4](https://doi.org/10.1140/epjc/s10052-007-0252-4). arXiv: [hep-ph/0612161](https://arxiv.org/abs/hep-ph/0612161)  
 2627 [hep-ph].
- 2628 [74] Rasmus Mackeprang and David Milstead. “An Updated Description of  
 2629 Heavy-Hadron Interactions in GEANT-4”. In: *Eur. Phys. J.* C66 (2010), pp. 493–  
 2630 501. doi: [10.1140/epjc/s10052-010-1262-1](https://doi.org/10.1140/epjc/s10052-010-1262-1). arXiv: [0908.1868](https://arxiv.org/abs/0908.1868)  
 2631 [hep-ph].
- 2632 [75] J. Alwall, R. Frederix, S. Frixione, V. Hirschi, F. Maltoni, O. Mattelaer, H. S.  
 2633 Shao, T. Stelzer, P. Torrielli, and M. Zaro. “The automated computation of  
 2634 tree-level and next-to-leading order differential cross sections, and their  
 2635 matching to parton shower simulations”. In: *JHEP* 07 (2014), p. 079. doi:  
 2636 [10.1007/JHEP07\(2014\)079](https://doi.org/10.1007/JHEP07(2014)079). arXiv: [1405.0301](https://arxiv.org/abs/1405.0301) [hep-ph].

- 2637 [76] “dE/dx measurement in the ATLAS Pixel Detector and its use for particle  
2638 identification”. In: (2011).
- 2639 [77] ATLAS Collaboration. “The ATLAS Simulation Infrastructure”. In: *Eur.*  
2640 *Phys. J.* C70 (2010), pp. 823–874. doi: [10.1140/epjc/s10052-010-1429-9](https://doi.org/10.1140/epjc/s10052-010-1429-9). arXiv: [1005.4568 \[physics.ins-det\]](https://arxiv.org/abs/1005.4568).
- 2642 [78] Alexander L. Read. “Presentation of search results: The CL(s) technique”.  
2643 In: *J. Phys.* G28 (2002). [,11(2002)], pp. 2693–2704. doi: [10.1088/0954-3899/28/10/313](https://doi.org/10.1088/0954-3899/28/10/313).
- 2644



2645 DECLARATION

---

2646 Put your declaration here.

2647 *Berkeley, CA, September 2016*

2648

---

Bradley Axen



2649

2650 COLOPHON

2651

Not sure that this is necessary.